Simulation Based Design and Performance Assessment of a Controlled Cascaded Pneumatic Wave Energy Converter

by

Eric Thacher
B. Sc., University of Manitoba, 2015

A Thesis Submitted in Partial Fulfillment
of the Requirements for the Degree of

MASTER OF APPLIED SCIENCE

in the Department of Mechanical Engineering

University of Victoria

Simulation Based Design and Performance Assessment of a Controlled Cascaded Pneumatic Wave Energy Converter

by

Eric Thacher
B. Sc., University of Manitoba, 2015

Supervisory Committee

Dr. Brad Buckham, Department of Mechanical Engineering
Supervisor

Dr. Henning Struchtrup, Department of Mechanical Engineering
Departmental Member

Dr. Curran Crawford, Department of Mechanical Engineering
Departmental Member

Abstract

Supervisory Committee

Dr. Bradley Buckham

Supervisor

Dr. Henning Struchtrup

Departmental Member

Dr. Curran Crawford

Departmental Member

The AOE Accumulated Ocean Energy Inc. (AOE) wave energy converter (WEC) is a cascaded pneumatic system, in which air is successively compressed through three point absorber devices on the way to shore; this air is then used to drive an electricity generator. To better quantify the performance of this device, this thesis presents a dynamically coupled model architecture of the AOE WEC, which was developed using the finite element solver ProteusDS and MATLAB/Simulink. This model is subsequently applied for the development and implementation of control in the AOE WEC. At each control stage, comprehensive power matrix data is generated to assess power production as a function of control complexity.

The nature of the AOE WEC presented a series of novel challenges, centered on the significant residency time of air within the power take-off (PTO). As a result, control implementation was broken into two stages: passive and active control. The first stage, passive control, was realized as an optimization of eight critical PTO parameters with the objective of maximizing exergy output. After only 15 generations, the genetic algorithm optimization led to an increase of 330.4% over an initial, informed estimate of the optimal design, such that the annually-averaged power output was 29.37 kW. However, a disparity in power production between low and moderate energy sea-states was identified, which informed the development of an active control strategy for the increase of power production in low energy sea-states. To this aim, a recirculation-based control strategy was developed, in which three accumulator tanks were used to selectively pressurize and de-pressurize the piston at opportune times, thereby increasing the continuity of air throughput. Under the influence of active control, sea-states with significant wave heights between 0.75 m – 1.75 m, which on average encompass 55.93% of the year at the Amphitrite Bank deployment location, saw a 16.3% increase in energy production.

Table of Contents

List of Tables

List of Figures

Nomenclature

A	Added mass coefficient.
A_{cyl}	Cross-sectional area of the piston.
$\mathrm{A_{orifice}}$	Cross-sectional area of the valve orifice.
A_{panel}	Area of a particular panel in the hydrodynamic mesh.
A_{∞}	Added mass coefficient at infinite frequency.
AOE	Accumulated Ocean Energy.
B	Added damping coefficient.
C_d	Drag coefficient.
C_P	Specific heat of air at constant pressure.
C_v	Specific heat of air at constant volume.
D_{cyl}	Diameter of the piston cylinder.
D_{float}	Diameter of the float of the Accumulated Ocean Energy converter.
D_1	Diameter of the first device in the Accumulated Ocean Energy converter.
D_2	Diameter of the second device in the Accumulated Ocean Energy converter.
D_3	Diameter of the third device in the Accumulated Ocean Energy converter.
${D_1}^*$	First device in the Accumulated Ocean Energy converter.
${D_2}^*$	Second device in the Accumulated Ocean Energy converter.
${D_3}^*$	Third device in the Accumulated Ocean Energy converter.
E_{final}	Total closed system exergy in the converter at the end of the simulation.
E_{flux}	Wave energy flux (wave power per incident metre).
$E_{initial}$	Total closed system exergy in the converter at the start of the simulation.
E_{total}	Total annual wave energy flux.
F	Force.
F_{drag}	Drag force induced from waves.
F_{exc}	Wave excitation force.
$F_{friction}$	Force of friction acting on the motion of the piston.
F_{hs}	Hydrostatic force.

F_{PTO}	Power take-off force.
$F_{moorings}$	Mooring force.
F_{rad}	Radiation force.
FK	Froude-Krylov force.
H_s	Significant wave height.
$\overline{H_s}$	Average significant wave height within a wave histogram grouping; used in the calculation of representative sea-states for the Amphitrite Bank location.
K	Wave number.
L	Length.
L_1	Length of the first device in the Accumulated Ocean Energy converter.
L_2	Length of the second device in the Accumulated Ocean Energy converter.
L_3	Length of the third device in the Accumulated Ocean Energy converter.
M	Number of sea-states per section of the wave histogram; used in the calculation of representative sea-states for the Amphitrite Bank location.
N	Number of hours of occurrence (on an annual basis) of a particular sea-state within the wave histogram.
N_{freq}	Number of wave frequencies included in wave spectrum when inputted to ProteusDS simulation.
N_{hours}	Number of hourly occurrences throughout the year; used in the calculation of the annual wave energy flux.
N_{Total}	Total number of hours throughout the year.
OR	Orifice Ratio, defined as the ratio of the valve diameter over the piston diameter.
P	Pressure.
$P_{Absorbed}$	Power absorbed by the converter over the course of the time step.
P_{amb}	Ambient pressure.
P_{th}	Motion threshold needed to identify peak has been exceeded.
$P_{Produced}$	Power produced by the converter over the course of the time step.
P_{RT}	Pressure of recirculation tank.
$\mathrm{P}_{\mathrm{upstream}}$	Pressure of the upstream volume; used to calculate flow limits through valve.

$P_{Produced}$	Power produced by the converter over the course of the time step.
PTO	Power take-off.
R_s	Individual gas constant of air.
R_1	Control signal used to define the flow direction in the lower piston chamber.
R_2	Control signal used to define the flow direction in the upper piston chamber.
RT	Recirculation tank.
S	Scattering force.
T	Temperature.
T_{amb}	Ambient air temperature.
T_{th}	Motion threshold needed to identify trough has been exceeded.
$\mathrm{T_{upstream}}$	Temperature of the upstream volume; used to calculate flow limits through a valve.
T_e	Wave energy period.
$\overline{T_e}$	Average wave energy period within a wave histogram grouping; used in the calculation of representative sea-states for the Amphitrite Bank location.
T_p	Wave peak period.
T_w	Ambient water temperature.
V	Volume.
WEC	Wave energy converter.
a	Surface area
$c_{end-stop}$	Damping coefficient used in the application of end-stop forces.
e	Flow exergy.
g	Acceleration due to gravity.
h_{amb}	Enthalpy of the ambient air; used in the calculation of the flow exergy.
h_{out}	Enthalpy of the outlet flow; used in the calculation of the flow exergy.
$k_{end-stop}$	Spring constant used in the application of end-stop forces.
k_{hs}	Hydrostatic stiffness.
k_r	Impulse response kernel function.
m	Mass.

m_{cyl}	Mass in the piston cylinder.
m_{∞}	Equivalent mass, due to the deflection of surrounding fluid as the body moves (added mass).
$\dot{\mathrm{m}}$	Mass flow through a valve.
$\dot{\mathrm{m}}_{\mathrm{control}}$	Flow rate limit through the valves, based on the application of an active control strategy.
$\dot{\mathrm{m}}_{\mathrm{max}}$	Flow rate limit through the valves, based on the state of air and dimension of the valve.
$\dot{\mathrm{m}}_{\mathrm{model}}$	Flow rate limit through the valves, based on an artificial model-based flow constraint that is used to ensure numerical stability.
$\vec{n}$	Normal vector
s_{amb}	Entropy of the ambient air; used in the calculation of the flow exergy.
s_{out}	Entropy of the outlet flow; used in the calculation of the flow exergy.
t	Current time step.
t_{total}	Total time period.
t^{*}	Current time, used in the calculation of the radiation force.
v	Velocity in an arbitrary direction.
z	Position in the vertical (heave) direction.
z_{limit}	Vertical limit on the motion of the float; used in the application of end-stop forces.
z_m	Minimum motion from last trough/peak needed in order for current motion to be identified as a peak/trough respectively.
z_{mean}	Mean water level of the Accumulated Ocean Energy converter.
z_{peak}	Vertical position of the latest peak in piston motion.
z_{trough}	Vertical position of the latest trough in piston motion.
$\dot{z}$	Velocity in the vertical (heave) direction.
$\dot{z}_{rel}$	Relative velocity in the vertical (heave) direction between the float and spar, which defines the velocity of the piston.
$\ddot{z}$	Acceleration in the vertical (heave) direction.

β	Pressure ratio across the valve, defined as the downstream pressure over the upstream pressure.
$\emptyset$	Wave phase, which is defined for each frequency in the wave spectrum when inputted to ProteusDS simulation.
$\Delta \mathrm{t}$	Simulation time step.
ΔU	Change in internal energy; used in the calculation of the absorbed energy.
γ	Ratio of specific heats of air.
η	Current height of the wave, used in the calculation of hydrostatic force.
θ	Wave direction, which is defined for each frequency in the wave spectrum when inputted to ProteusDS simulation.
ρ	Density.
τ	Time interval measured from the start of the simulation, which is used in the calculation of the radiation force.
ω	Wave frequency.
Subscripts	
cyl	Cylinder.
$cyl, ch.1$	Cylinder, chamber 1; this is the lower chamber of the cylinder.
$cyl, ch.2$	Cylinder, chamber 2; this is the upper chamber of the cylinder.
$end-stop$	Referring to the collision of the piston with the ends of the piston chamber. The high/low motion limit refer to the top and bottom of the cylinder chamber, respectively.
opt	Used in the calculation of model-based flow limits, to denote the optimal case in which the maximum flow rate between the upstream and downstream volume occurs.

Acknowledgments

I would like to sincerely thank everyone who helped guide me towards the completion of this thesis. In particular, a special thank you to Dr. Brad Buckham for his expert guidance, and kind and generous attitude in accommodating my schedule at every turn; Dr. Helen Bailey for ceaselessly and expertly answering my continuous stream of questions and Dr. Bryson Robertson for his valuable insight when needed most. In addition, this work would not have been possible without the support from my colleagues both in WCWI and IESVic as a whole.

On a personal note I would like to thank my sister and parents for their continual support, as well as my friends both in Victoria and back in Winnipeg for their understanding in tough times, and for celebrating with me in the best of times. You provide me with the motivation to continue pursuing research.

This work was funded by the Natural Sciences and Engineering Research Council of Canada and AOE Accumulated Ocean Energy Inc., and was completed in collaboration with Ocean Networks Canada. Special thanks goes to those at AOE Accumulated Ocean Energy Inc. for their partnership in this work.

Dedication

For my parents; without their support this would not have been possible.

Chapter 1. Introduction

Global energy demands are increasing year over year, and coupled with increasingly restrictive international emissions policies, there is a growing mandate for the use of renewable energy sources to meet demand. While current commercial renewable energy activities are focused on wind and solar resources, the dual impact of increased energy demand and lower emissions allowances has generated interest in largely underdeveloped renewable sources such as wave energy. Baseline estimates of the global wave resource suggest that the annual wave power incident on ocean-facing coastlines is 2.11 TW [1]. Furthermore, the resource has several advantageous characteristics when compared to solar and wind energy, such as a higher power density, greater predictability, as well as a strong temporal [2] and spatial correlation between the resource and demand (37% of the world’s population lives within 90 km of the coast) [3]. Consequently, this resource represents a valuable option in the global renewable energy portfolio. However, the large-scale deployment of wave energy devices is hampered by the high costs of physical testing, which has led to a lack of long-term test deployments and uncertainty in wave energy converter (WEC) power production estimates. Performance uncertainty has further reduced the likelihood of securing the significant level of funding needed to advance the wave industry, particularly when considering the existence of more mature renewable technologies. As a result, research at the present must focus on strengthening our understanding of present day device performance, while also the means to improve the viability, efficiency, and affordability of the power from wave energy devices [3] [4].

A cost effective method of meeting these requirements is a significant challenge, but valuable insight may be gathered through the development of high fidelity numerical models. In particular, detailed wave resource data at device deployment locations, coupled with high fidelity models of the device, can underpin a process for generating realistic estimates of the power that would be transmitted to the grid [3] [5] [6]. These models are also critical for the development of holistic and accurate WEC control strategies, as iterative tuning of control parameters requires reproducibility in environmental conditions. The implementation of optimal WEC control is crucial for maximizing WEC power production while meeting strict grid integration requirements [7]. In an effort to address these next steps in the development of the wave energy industry, the current work will describe the development of a numerical simulation tool for a novel point absorber WEC and subsequent application of the simulator to the development of a power-maximizing control strategy. In doing so, detailed power production estimates are provided as a function of incremental increases in the complexity of the control strategy.

1.1 Background

The wave energy field has not yet converged to a single device, and as such is marked by a huge variety of WECs with fundamentally different operating principles. To date, there has been more than 100 prototypes of WEC devices [4], of which a variety of reviews exist on both the available technologies, operating principles, and status [3] [8] [9] [10]. Lopez et al [3] provide a listing of 157 WEC devices, which for brevity are not listed here. Instead, a device classification is presented, based on the nature of wave power capture.

Table 1.1: Classification of wave energy devices by the nature of wave power capture.

Classification (incl. examples)	**Definition**	**Motion**
Attenuators (Pelamis, Biopower)	Aligned parallel to the direction of wave propagation.	
Terminators (AWS, OREC)	Aligned perpendicular to the direction of wave propagation.	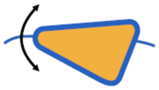
Overtopping Devices (Wave Dragon, Limpet, Manchester Bobber, OceanLinx, ORECON, SEEWEC)	Not aligned with wave direction. Top of breaking wave is absorbed.	
Point Absorbers (OPT, WaveBob, AOE)	Not aligned with wave direction. Omni-directional wave absorption.	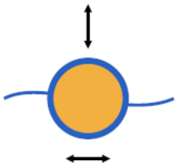

Point absorber converters are defined as having a small horizontal dimension when compared to the incident wave-length [11]; this is in contrast to attenuator and terminator devices, which are of a comparable dimension to the wave-length in the direction of the waves, or direction perpendicular to the waves, respectively. Overtopping devices are further differentiated based on the nature of wave energy absorption, for which power is captured as the wave breaks over the device. In addition to the marked differences between these devices, it is clear how each of these categories have the capability of producing a diverse subset of WEC designs; in particular, the location of the device (offshore, near-shore, or offshore) as well as the working principle of the power take-off. In combination, one can see how a vast variety of WEC prototypes are developed, each of which provide potential research directions for the wave industry. However, this variety of WEC prototypes presents a challenge to the sector to the whole, as a limited pool of resources is diluted across divergent efforts. In particular, many of the challenges impeding WEC commercialization, such as the management of WEC power quality and control, operation and maintenance challenges, or even array design and deployment considerations [12] are all specific to a given device. Consequently, the commercialization of any single WEC device requires a substantial level of focused research and capital investment in order to overcome design challenges. Many of these challenges are significant and expensive to test and overcome; as a result, only 5% of WECs have reached technology readiness level five (full/large scale (100 kW) grid connected prototype) [3].

In light of these challenges, the development of device-specific models becomes critical. High fidelity numerical models present a cost effective method of assessing operation, control, and deployment challenges. However, it is not sufficient to use a generalized model for the design of highly nonlinear systems such as holistic control strategies. Instead, focus must be placed on developing design-specific models, particularly for devices with unconventional operating principles. The present study will focus on a novel WEC developed by the Victoria based company AOE Accumulated Ocean Energy Inc. This WEC falls within the well-studied floating point-absorber class of devices, operating in the near-shore environment, but presents a series of unique additional challenges that underscore the need for developing a unique numerical model.

1.2 Accumulated Ocean Energy Converter

The function of the AOE WEC is to produce highly compressed air, which can then drive a variety of on-shore processes such as reverse osmosis desalination or electricity generation. However, the production of compressed air using a variable renewable resource such as ocean waves presents a significant design challenge; namely, ensuring that air is consistently produced at a sufficient pressure to drive the relevant on-shore processes. To tackle this challenge, AOE developed a cascaded network of point-absorber devices, which are pictured in Fig. 1.1. The first device in the cascade draws fresh air from the atmosphere, compresses the air using a piston contained within the spar of the device, and then passes this pressurized air to the next device. After initial compression of atmospheric air, subsequent devices in the chain compress the output from upstream devices. Consequently, after several compression cycles from latter devices in the chain, the air reaches sufficient pressure to drive the on-shore equipment. For the current study, the air is assumed to drive an on-shore electricity generator. In addition, a cascade of three devices is considered, however, it is possible for more devices to be added if higher pressure air is required for a particular on-shore process.

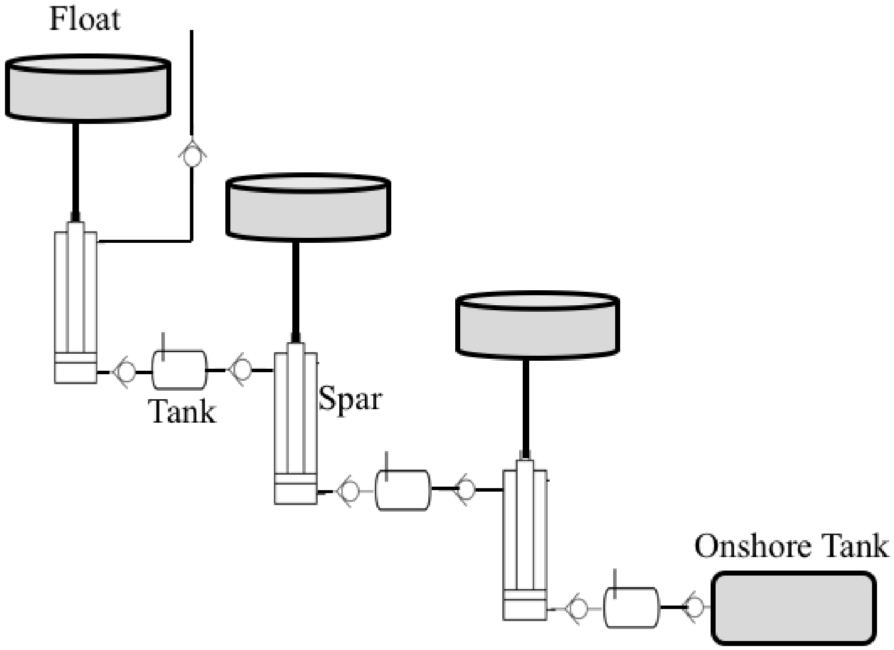

Figure 1.1: Schematic of the cascaded 3-device configuration of the AOE WEC.

Since the motion (and subsequent piston compression/expansion cycles) of different devices may not align, the devices are separated by accumulator tanks. These tanks temporarily store air, prior to it being passed to the next device. Air flows between devices when the pressure in the air storage tank exceeds that of the cylinder in the subsequent device. Once the air in the final tank reaches a desired crack pressure, air is released from the tank and flows to shore for the production of electricity. In order to prevent backflow, unidirectional flow valves separate each component of the system.

For each device, the piston compression is driven by the relative motion between the spar of the device, which is moored to the sea-floor, and the wave-following float. The primary components of each device are shown in Fig. 1.2. As an indication of the device scale, primary dimensions are summarized in Table 1.2.

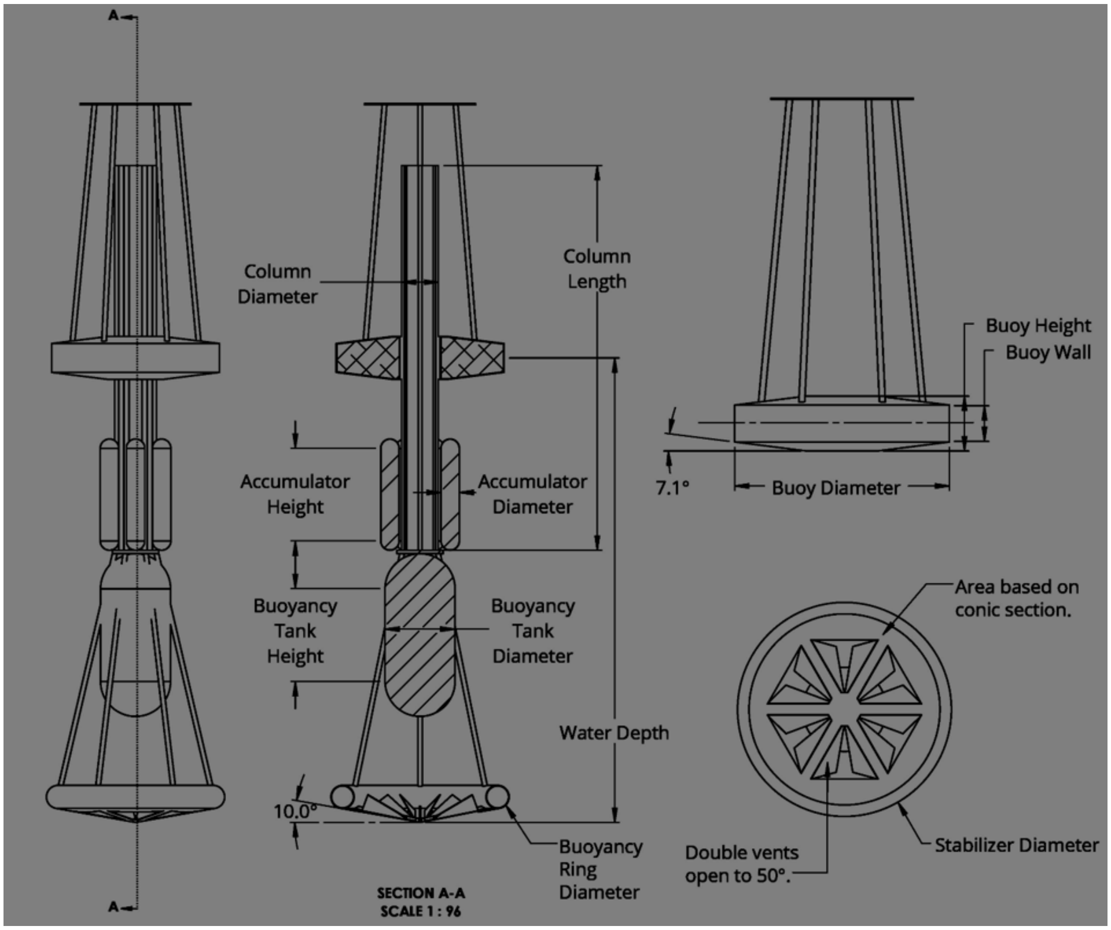

Figure 1.2: Components of the AOE WEC.

Table 1.2: Primary dimensions of the AOE WEC.

Dimension	Value	Dimension	Value
Column Diameter	2.74 m	**Column Length**	8.43 m
Accumulator Height	1.63 m	**Accumulator Diameter**	0.91 m
Buoyancy Tank Height	5.08 m	**Buoyancy Tank Diameter**	3.81 m
Buoyancy Ring Diameter	1.52 m	**Water Depth**	18.69 m
Buoy Diameter	10.97 m	**Buoy Height**	2.79 m
Buoy Wall	1.85 m	**Stabilizer Diameter**	10.97 m
Float Mass	33384 kg	**Air Tank Mass**	314 kg
Buoyancy Tank Mass	93508 kg	**Stabilizer Assembly Mass**	74162 kg
Column Assembly Mass	15918 kg		

Each device contains the following components:

1. Float - highly buoyant and follows the wave profile. In doing so, it moves relative to the spar and compresses the interior piston cylinder.
2. Spar – separates the mass and buoyant centres of the device in order to provide a passive buoyant righting moment; the spar also contains the piston cylinder.
3. Accumulator Tanks (x6) – placed radially around the spar in order to provide a mechanism for temporary air storage.
4. Buoyancy tank – encircles the spar and ensures neutral buoyancy of the device. The buoyancy tank is a primary determinant of the centre of buoyancy, which is necessary to produce a passive righting moment.
5. Heave plate – connected to the bottom of the spar. The heave plate damps vertical motion, through an increase in the added mass of the WEC.
6. Mooring lines (x3) – prevent wave drift and ensure the spar remains largely stationary.

The relative motion between the float and spar is the driver of the power take-off system, through the creation of piston compression. To aid in the understanding of the nature and timing of piston compression, a cross section of the piston during two key stages in the compression cycle is provided in Fig. 1.3.

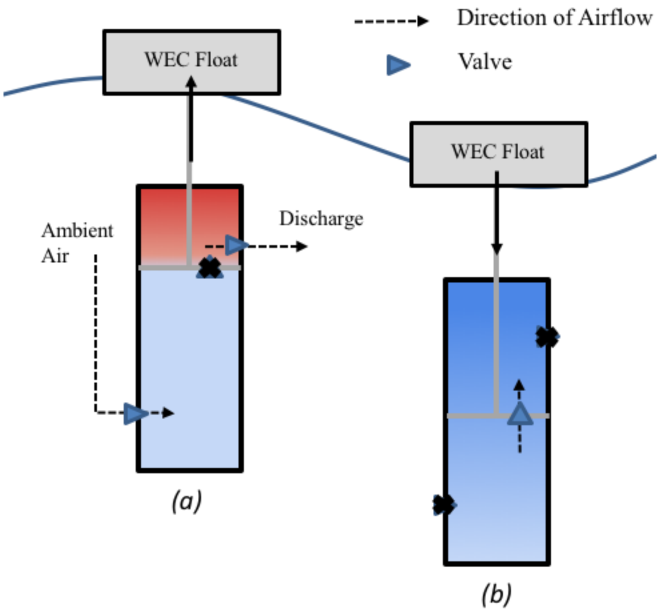

Figure 1.3: Piston dynamics during: (a) wave crest, (b) wave trough.

The piston contains two-chambers, which are alternately compressed during wave motion. The flow of air between these chambers, as well as the intake and exit of air, is governed by a series of unidirectional flow valves. As the wave crests (and the float rises, producing a piston upstroke), the intake valve is opened and air is drawn into the bottom chamber. This air is drawn from the atmosphere (in the case of the first device) or the tank of an upstream device. Simultaneously, the top chamber is compressed and when it reaches a sufficient pressure, the exit valve is opened and air flows into one of the accumulator tanks placed radially around the spar of the device. This is the power production phase of motion. Conversely, when the wave crest passes and the float begins to drop (producing a piston downstroke), the intake and exit valve shut and the top chamber of the piston is prepped for the subsequent compression cycle. In particular, the bottom chamber compresses, and when the pressure exceeds that of the top chamber, the intermediate flow valve opens and air passes to the top chamber. This valve is shut once the trough of the wave is reached, after which the cycle repeats.

In addition to the above wave-induced variations in the piston operation, the flow of air from the piston is determined as the function of a number of additional parameters. In particular, the quantity and state of air throughout the cascade is highly dependent on the geometry of the piston and downstream components. Furthermore, airflow from the piston is highly dependent on the timing of valve events, as well as the pressure of the particular accumulator tank to which flow is directed (each of the six tanks may contain a different pressure). In combination, it is clear to see that the WEC performance is highly dependent on both passive (geometry) factors as well as dynamic changes in the available controllable geometries (valves and accumulator tanks). Consequently, the nature of the AOE WEC necessitates the implementation of a holistic PTO force control strategy, which addresses both passive and active operational factors in order to maximize the production of power output. With this understanding of the operation and design of the AOE WEC, as well as the need for control implementation, it is possible to discuss the objectives of this thesis.

1.3 Objectives

The AOE device provides novel challenges, and to see these challenges overcome within a timeline that enables industry development, a significant body of focused research is required. The technical objectives of the present work are to:

1. Develop a high fidelity wave-to-wire model of the AOE Accumulated Ocean Energy wave energy converter. The model framework will resolve the device hydrodynamics, power take-off, and on-shore generator system.
2. Utilize the model to develop and implement holistic, layered, PTO force control for the AOE WEC.
    a. The first tier of control will focus on passive control, which will provide a baseline level of performance for the device.
    b. The second tier will introduce active control, which provides the opportunity to further increase the power output or target additional objectives as necessary.
3. Quantify the performance of the WEC with active control, as well as the absence of control in a particular device deployment location. This will provide accurate performance data for the AOE WEC, while simultaneously providing a detailed analysis on the performance benefits achieved with incremental increases in control complexity.

This hierarchy of objectives outlines a cost effective means to test and optimize the WEC in a variety of sea-states. Not only does this inform WEC prototype design for ocean or tank-based testing, this enables the calculation of realistic power production estimates; as previously mentioned, these estimates are critical for the capture of investment funding. Furthermore, the application of this model for control implementation provides a methodology by which alternative control objectives may be targeted, without incurring risks associated with sea-based testing.

1.4 Contributions

Despite the focus of the technical objectives on the AOE WEC, that is not to say that the benefits of this thesis are limited to a particular converter. In contrast, there are several key contributions that will make inroads in largely unexplored areas of wave energy research. The contributions of this thesis are summarized as follows:

1. Extension of a dynamically coupled WEC modelling approach to a complex cascaded design. Required model fidelity is assessed by virtue of determining the sensitivity of the WEC performance to particular design parameters.

2. The development and application of a design optimization methodology for the implementation of passive WEC control.
3. Development and implementation of realistic active control objectives for a fully resolved power take-off system, including a brief cost-benefit analysis.
4. Comprehensive performance benchmarks are provided for a novel WEC.

The over-arching contribution of this thesis is in developing a methodology for WEC modelling and control implementation, which is then implemented for a complex WEC geometry. This methodology will inform the WEC industry on cost-effective methods to generate performance estimates in a variety of sea-states. In addition, through the application of layered control and evaluation of subsequent performance gains, this thesis will outline a methodology on how both passive and active control can be implemented in other WEC configurations.

1.5 Thesis Outline

The remainder of the thesis is laid out as follows. Pertinent literature review is included at the beginning of Ch. 2, 3, and 5.

Chapter 2 lays out the dynamically coupled modelling framework for the AOE WEC, including a detailed description of both the hydrodynamic and power take-off models. The modelling of the on-shore generator system is also addressed.

Chapter 3 details the methodology for implementing passive control in the AOE WEC.

Chapter 4 provides a detailed assessment of device performance under the influence of passive control. A power matrix for AOE WEC under the influence of the passive control is also presented.

Chapter 5 details the implementation of active control, again followed by an assessment of device performance. The incremental gains in performance subject to increased complexity of the chosen controller is discussed.

Chapter 6 summarizes the key conclusions of the thesis, as well as provides recommendations for future work.

Chapter 2. Modelling Framework

In this chapter, a high fidelity numerical model of the AOE Accumulated Ocean Energy multi-body WEC is developed with the capability of resolving the hydrodynamic and power take-off forcing acting on the WEC bodies in real time. The dynamically coupled approach resolves the performance impact of slight changes in the WEC geometry on a second-by-second basis; these impacts can then be mapped across a variety of sea-states to determine performance metrics on annual timescales. Furthermore, the model can illustrate the impact of active control implementation, by resolving the dynamic impact of undertaking a control action. The development of the model is motivated by insufficiencies in existing wave energy modelling techniques, for which a review is provided at the start of the chapter. The modelling framework is then described in general terms, after which a detailed discussion is provided on the two primary sections: the hydrodynamics and power take-off. Lastly, relevant parameters for the on-shore generation system are discussed.

2.1 Modelling Techniques for Wave Energy Converters

High fidelity models of wave energy technologies have been gaining traction in recent literature, as the coupled impact of increased research interest and ever-increasing computational speeds has improved the accuracy and range of applicability of modelling techniques. Numerical simulation techniques in particular provide a significant opportunity, as models can now be executed at speeds that allow iterative design development. These techniques have progressed significantly from initial wave energy mathematical modelling, which drew from the study of ship dynamics that took place prior to the mid-1970s [8]. Ship sea-keeping has continued to provide a parallel basis for hydrodynamic modelling development [13], but the wave energy industry has since provided strong modelling literature in its own right. Techniques have been developed that are tailored to a wide range of WEC geometries and objectives, for which a review of the available literature is provided. First, a general overview of WEC modelling techniques is presented, with a focus on techniques that are applicable to capturing wave-body interactions of point absorber converters. This is followed by a review of WEC systems modelling approaches, including the comparison of techniques on both the device (hydrodynamics, power take-off) and holistic (wave-to-wire) level. WEC systems approaches are defined as those that include additional components beyond the WEC itself, such as the device moorings, power take-off, or downstream mechanisms in the power conversion chain.

2.1.1 Hydrodynamic Modelling of Point-Absorber WECs

Due to numerous trade-offs between computational time and fidelity, no single model can perform equally well in all scenarios. Instead, models have been developed for particular applications, spanning the spectrum of study from macro-scale wave climate studies, using techniques such as spectral and Boussinesq models [14], to the study of high fidelity wave-body interactions. An extensive review of the modelling techniques for WECs, including limitations, is provided by Day et al [15], as well as Folley [16]. Given that the dominant physical phenomena change from one WEC to another [16], it is critical to consider the device in question when selecting a modelling approach. In particular, it is necessary to consider only relevant nonlinear effects, in order to improve accuracy without needlessly increasing computational cost [17]. For point absorber converters, the primary methods seen in wave energy literature are analytical methods, boundary element methods (BEM), and computational fluid dynamics (CFD) [4].

Analytical methods depend on a series of linear equations, which arise from linear wave theory. When using analytical methods, only a monochromatic wave input is considered, after which individual frequency constituents are superimposed. The basics of linear wave theory, and resulting analytical modelling methods, is provided by Folley [16], for which implementation in literature is extensive. Due to the linear system of equations, analytical methods provide a computationally efficient calculation method, but inherent assumptions limit the range of applicability of modelling results. In particular, analytical methods must be limited to waves with relatively smaller amplitude, negligible interaction between radiated and incoming waves, and solely linear viscous effects [4] [16]. While empirical approximations such as Morrison's equation provide a method of incorporating viscous effects, the accuracy of this approximation is to a much lesser degree than other methods [18].

BEM is an advanced potential flow method that is applicable to more complex geometries and wave conditions; a description of the theory is provided by Lee and Newman [19]. BEM requires the discretization of the WEC surface into a series of panels, after which Green's theorem is applied in order to obtain the potential flow field. With the flow field known, the pressure, forces, and moments acting on the body surface are determined. Numerous hydrodynamic software packages make use of BEM, including WAMIT, NEMOH, and AQUAPLUS in the frequency domain, and ACHIL3D in the time domain [17]. In the frequency domain the results are calculated using a linear superposition of individual components, while in the time domain higher order schemes are used to better calculate the interactions between waves and floating bodies [4]. To further improve accuracy, numerous nonlinear extensions of the BEM method exist, for which several methods are provided by Retes et al [17]. However, despite the capture of certain nonlinear wave-body interaction effects, such as instantaneous changes in wetted surface, a major drawback with potential flow codes are that inviscid irrotational flow is assumed. While a more comprehensive listing of limitations from inviscid flow assumptions are presented by Bretl [18], some key restrictions are that BEM is not applicable to complex flow around moving structures [14], and breaking wave dynamics cannot be captured [4] [14].

Consequently, for the highest level of accuracy and broadest range of applicability, Li and Yu [4] recommend using computational fluid dynamics (CFD). CFD provides a fully viscous solution, and allows for the capture of effects such as boundary layer separation, turbulence, wave breaking, multi-phase flow, or overtopping that cannot be predicted with potential flow models [4] [14]. A variety of CFD methods exist [17] [18], including Direct Numerical Simulation (DNS), Smoothed Particle Hydrodynamics (SPH), Large-Eddy Simulation (LES), and Reynolds-Averaged Navier Stokes (RANS); each of these methods vary in terms of accuracy and computational expense. CFD models that have been tailored to the prediction of wave-structure interactions have also been developed, and include models such as SWENSE and IH2VOF [17]. However, the level of accuracy provided by CFD comes at the expense of significantly higher computational times [4] [17] [14]. Li and Yu [4] provided sample simulation times for a point absorber WEC, and found that a BEM simulation with 30 wave frequencies, conducted with a single 3.33 GHz Intel i5 processor, was completed in 2804s. Conversely, a NSEM CFD simulation with a single wave frequency, conducted on 64 cores (with each node consisting of a dual-socket/quad core 2.93 GHz Intel Nehalem processor), took 12 hours to complete.

2.1.2 WEC System Modelling

In light of the prohibitive computational requirements associated with CFD, Many WEC systems solvers (solvers that incorporate additional components beyond the components of the WEC itself), use BEM or analytical methods to resolve pertinent nonlinear hydrodynamic effects. Due to the use of a variety of these solvers in literature, studies have assessed and compared the performance of specific modelling codes [20] [21]. Combourieu et al [20] provide a code-to-code comparison of mid fidelity modelling codes. The four codes compared in the analysis are InWave, WaveDyn, ProteusDS, and Wec-Sim v1.0, for which the characteristics of each of the codes are summarized by Combourieu et al [20]. Following the completion of multiple tests, it was found that there was good agreement among all four codes, but no recommendations were made for a particular code. Conversely, Garcia-Ross et al [21] looked to provide code recommendations by hosting a blind simulation competition. The objective of each participant was to simulate the motion of a submerged horizontal cylinder without complete knowledge of the wave motion. Six different approaches were assessed, with recommendations being based on the root-mean-square (RMS) error of the predicted surge and heave motions. The lowest error was achieved by the frequency domain BEM code FAST, with hydrodynamic coefficients from WAMIT, followed by the time domain finite element solver ProteusDS, with hydrodynamic coefficients from ShipMo3D. Detailed descriptions of these models are provided in Lawson et al [22] and Roy et al [23], respectively. Despite the determination of a ranking, Garcia-Ross et al [21] qualified the ordered results by stating that four of the six codes provided strong comparisons to the experimental data, and the remaining two codes had high RMS errors that were tied to external factors. Consequently, the overall level of agreement between the numerical simulations and experimental data is very good.

A large body of research is also dedicated to the study and development of different techniques when handling complete wave-to-wire dynamics [24] [25] [7]. Sandvik [24] details the wave-to-wire development and subsequent control implementation for the Bolt2 converter; a linear hydrodynamic model is used in the work, which superimposes results from particular wave frequencies. Nielson et al [25] provide a review of wave-to-wire model requirements, including some of the tools available. Penalba et al [7] provide a review of wave-to-wire models of wave energy converters in the context of control development, in which the required components of a complete wave-to-wire model for control design and implementation are presented. Ten models from the available literature are assessed in comparison to these requirements, and it is concluded that no model has yet been developed with sufficient fidelity to develop a holistic, wave-to-wire, control strategy [7]. Despite these limitations, two papers [6] [26] are discussed that incorporate both nonlinear hydrodynamics and downstream elements of the power conversion chain. These models present a potential methodology that may be extended to the current work. Forehand et al [26] compute the hydrodynamic forcing using a state space representation of Cummin’s equation with the addition of nonlinear hydrostatic forces, which account for the instantaneous wetted surface. Hydrodynamic coefficients are determined using WAMIT. This nonlinear hydrodynamic model is implemented in the time domain in MATLAB/Simulink, at which point it is coupled to models of the hydraulic PTO system and generator. Bailey et al [6] developed a dynamically coupled wave-to-wire modelling approach by which the hydrodynamic and mooring forcing is calculated using finite element solver ProteusDS, using hydrodynamic parameters inputted from either WAMIT or ShipMo3D, while the PTO and generator model implemented in Simulink. The Simulink and ProteusDS components of the model pass information in real-time in order to more accurately simulate the

WEC power conversion chain. The application of this methodology to an oscillating water column (OWC) WEC is provided by Bailey et al [27].

2.2 Model of the AOE Converter

As demonstrated by the array of available hydrodynamic modelling techniques, there is no universal solution for capturing all relevant phenomena that drive device motion, and execute calculations fast enough to facilitate reasonable computation times. In addition, the AOE converter presents a variety of unique challenges in the modelling process; namely, the significant residency time of air within the system. Consequently, the modelling framework must provide the capability of resolving the state of air within the power take-off for the duration of the simulation. Furthermore, the model must provide a venue for incorporating control. To this aim, the approach provided by Bailey et al [6] [27] provides an acceptable compromise between accuracy and computational efficiency. Furthermore, the applicability of this approach to modelling a detailed pneumatic system has already been demonstrated [27]. Consequently, this model architecture was applied to the current work.

The developed model architecture dynamically couples the calculation of the external forcing (hydrodynamics, mooring loads) with a separate simulation of the internal dynamics (power take-off) to improve computational speed. The external forcing is resolved in finite element solver ProteusDS, while the internal PTO dynamics are determined in MATLAB/Simulink. The separation of the internal and external dynamics allows for the calculations to be conducted at two different rates, which are adjusted to correspond to the nature of dynamic responses in each model. To ensure computational stability, the external dynamics are resolved at a variable time step with a minimum rate of 500 Hz, while the internal dynamics are resolved at 500 Hz. At each 2 ms interval, information is passed between the two models. In addition to the above modelling rates, the sea-state is updated at a rate of 10 Hz; this is based on the relatively slow nature of environmental changes. The passing of information between the two models in the current work, including key outputs, is described in Fig. 2.1.

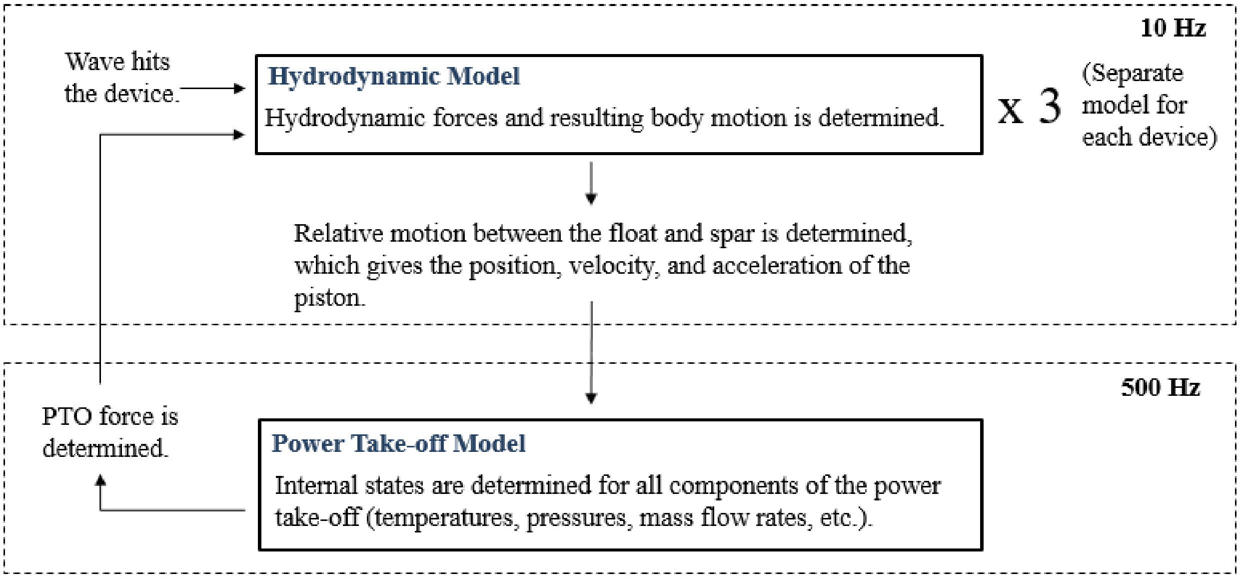

Figure 2.1: Passing of state information during a single time step of the coupled model architecture.

At each time step of the ProteusDS simulation, the hydrodynamic and mooring forces are resolved using the current wave condition; this allows the motion of the body to be determined. The relative motion between the float and spar is subsequently determined, and passed to the power take-off model as the magnitude and velocity of piston compression; the piston compression is unique to each device within the WEC. The PTO model then uses the current state of the system, coupled with the piston compression, to determine the state of air within both chambers of the piston cylinder. The resulting flow through downstream components is subsequently propagated throughout the model to determine the complete state of air within the system. Lastly, the magnitude of the PTO force (a function of the state of air within each cylinder) is determined separately for each device, and passed back to the hydrodynamic model. To better illustrate the particular variables that are passed between the two components of the simulation, the variables used to define the state of the system at each time step are given in Fig. 2.2. For simplicity, valve dynamics and corresponding state variables are not included. Instead, the primary state variables defining the internal components of both models are given, as well as the variables that are passed between models. These include the variables passed between ProteusDS and Simulink, as well as the variables that define the user-inputted wave spectrum, which is sampled by ProteusDS to produce the current wave condition.

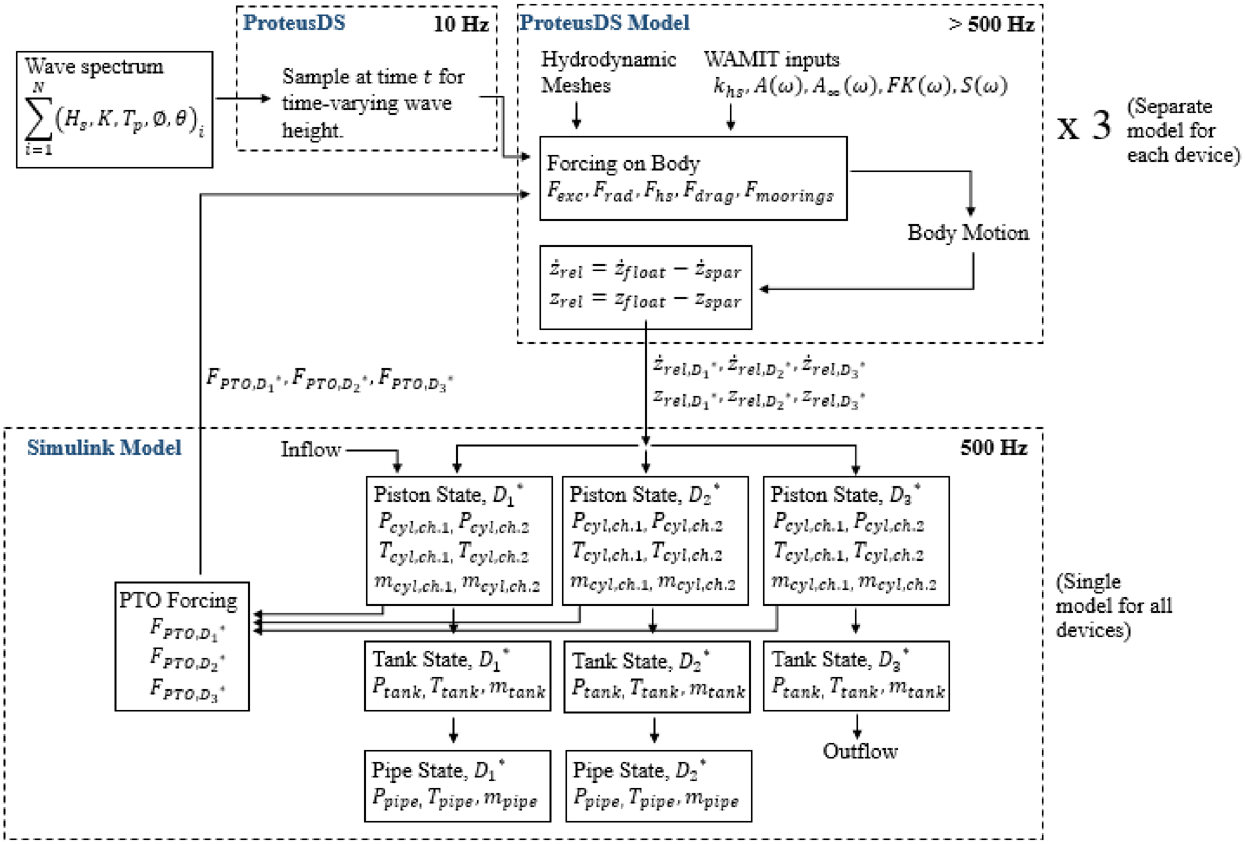

Figure 2.2: Key variables used to define the complete state of the system within the coupled model architecture.

The determination of each of the state variables included in Fig. 2.2 is described in subsequent sections. For now, it is sufficient to state that the selected approach resolves real-time variation in the sea surface elevation, WEC hull motions, and compressed air state; all required to quantify the on-shore production of electricity. The combined model, incorporating aspects from three distinct software packages, is used to produce a six degree of freedom simulation of the AOE WEC in any user-defined sea state. The accuracy of the selected methodology is ensured through the use of the experimentally validated dynamic software ProteusDS [21]. Furthermore, thermodynamic relationships are taken from literature in order to ensure accuracy. Since the compression processes are simulated at 500 Hz, simple fundamental equations are sufficient to describe state changes. In order to illustrate the calculation procedure of both models in detail, the hydrodynamic and power take-off models are described in the following sections.

2.3 Hydrodynamic Model

The hydrodynamic and mooring loads are computed using the software package ProteusDS. ProteusDS is an experimentally verified finite element, non-linear, time domain solver that is used for the dynamic analysis of WEC and wave-body interactions. In addition, it has been shown to have strong performance when compared to other mid fidelity hydrodynamic codes [21]. ProteusDS has the optional capability of importing hydrodynamic coefficients, for the current work these coefficients were imported from the frequency domain BEM solver WAMIT v7; this follows the approach developed by Bailey et al [27].

2.3.1 Calculation of Hydrodynamic Coefficients

WAMIT v7 is a frequency domain BEM solver, for which the fundamental theory is provided in the user manual [28]. The solver is based on a potential flow model, which requires the discretization of the components into a panelized mesh. For each panel, potential flow theory is applied to resolve a velocity potential; this velocity potential is then used to resolve the pressures, forces, and moments acting on each panel. To improve computational time, instead of meshing each component individually the AOE device was grouped into two bodies: the float and spar/stabilizer assembly. Furthermore, the maximum physical panel size in the final mesh set to 1 m; this was the same panel size chosen by Bailey et al [27], and was selected as a compromise between accuracy and computational speed. The hydrodynamic mesh of both bodies is shown in Fig. 2.3. Since WAMIT computes hydrodynamic forcing with a constant mean water level, only components below the mean water level are included in the mesh. The mean water level on the WEC is indicated on a subset of the original drawing, shown in Fig. 2.3b.

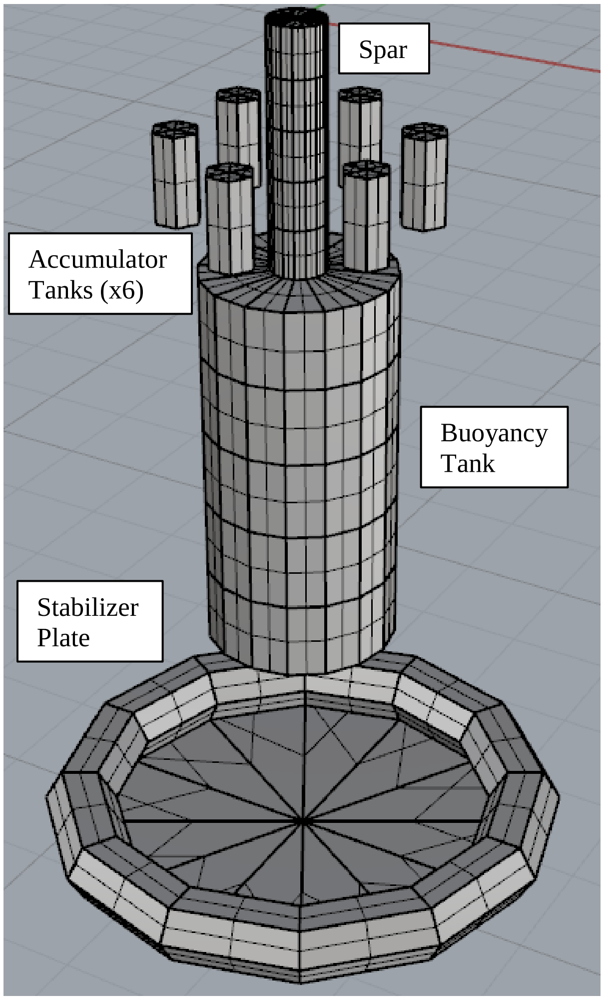

(a)

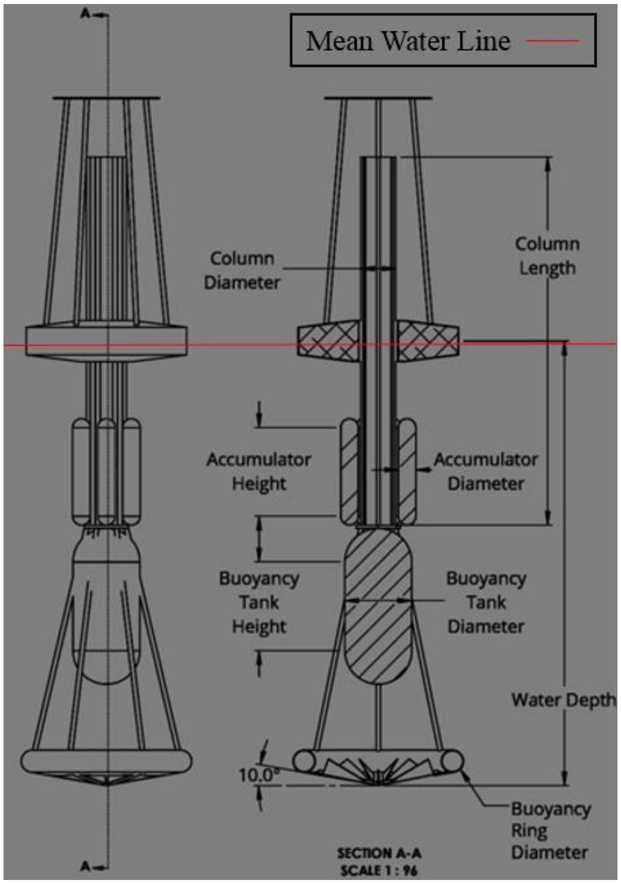

(b)

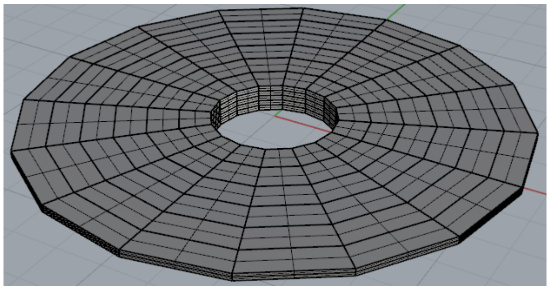

(c) Perspective view.

(c) Side view.

Figure 2.3: WAMIT panel mesh for the (a) spar/stabilizer assembly and (c) float. Original engineering drawing is shown in (b), with the mean water level indicated.

To improve the numerical stability of the assembly mesh, all components of the body are assumed to be solid. Consequently, components that are hollow (such as the spar), are reduced in diameter in order to ensure the mass of the component aligns with the design specification. As a result, bodies such as the storage tanks or buoyancy tank are no longer directly attached to other components of the converter. Instead, they are kinematically constrained in the positions that they would be on the actual system. Errors in the location and size of the buoyancy and accumulator tanks are assumed to be small, however, as the relative hydrodynamic contributions of these components are small when compared to bluff bodies such as the stabilizer plate and float.

Using these panelized surfaces, the following hydrodynamic coefficients were calculated: hydrostatic stiffness, added mass at infinite frequency, as well as the frequency dependent added mass, added damping, Froude-Krylov, and diffraction forces. To illustrate the dynamic responses of both bodies, selected parameters are included in Fig. 2.4 and 2.5. The frequency-dependent added mass and damping for both the float and spar/stabilizer assembly are shown in Fig. 2.4.

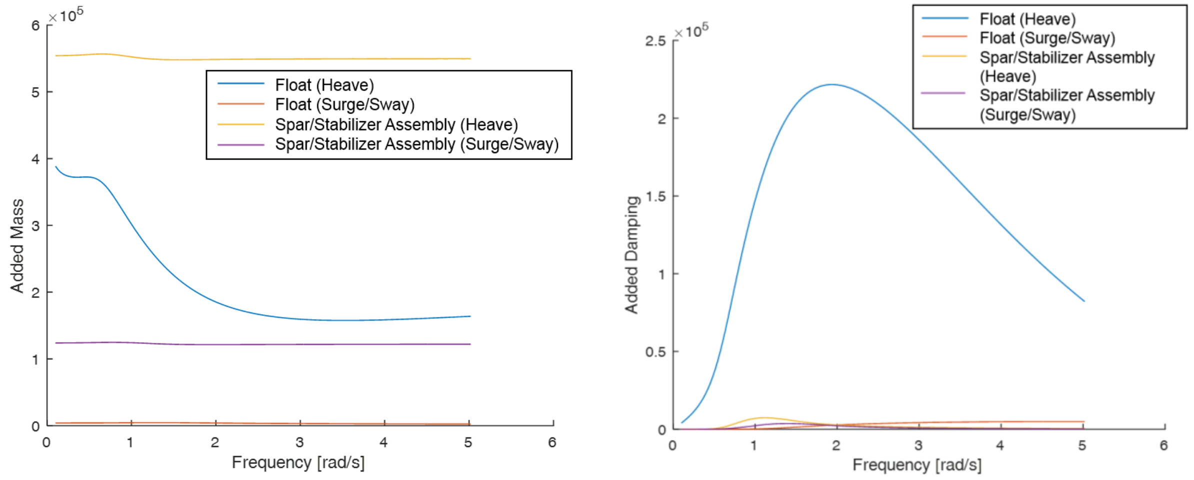

(a) (b)

Figure 2.4: Frequency dependent (a) added mass and (b) added damping for the float and spar/stabilizer assembly.

The added mass and added damping values were curtailed at frequencies above 5 rad/s. Due to the symmetry of the AOE design, the hydrodynamic coefficients for surge and sway are virtually identical. The frequency-dependent Froude-Krylov and scattering for both the float and spar/stabilizer assembly are shown in Fig. 2.5.

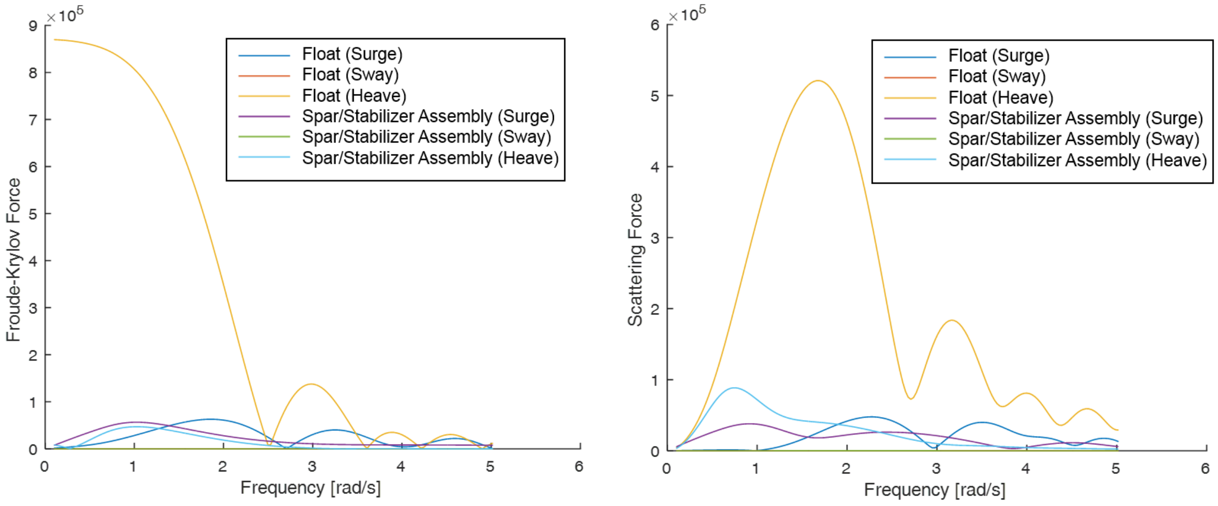

(a) (b)

Figure 2.5: Frequency dependent (a) Froude-Krylov and (b) Scattering force for the float and spar/stabilizer assembly.

While both Fig. 2.4 and 2.5 only show quantities in surge, sway, and heave, it is important to note that all quantities are calculated in all six degrees of freedom. Therefore, using these sets of coefficients, it is possible to determine the hydrodynamic forcing in six DOF in ProteusDS; the methodology for doing so is described in the following section.

2.3.2 Time Domain ProteusDS Simulation

ProteusDS requires the discretization of the components into a panelized mesh. The float and spar/stabilizer assembly were meshed separately, for which the hydrodynamic meshes used in ProteusDS are given in Fig. 2.6. While the same mesh was used for all three devices, the simulation of each device was run in a separate instance of ProteusDS to improve computational time. ProteusDS calculates the fluid kinematics using Airy wave equations, which are derived from potential theory. As a result, wake dynamics between the three devices are not considered. However, the devices are assumed to be placed 70 m apart, such that wake dynamics are not expected to have a significant impact on the power capture of the devices.

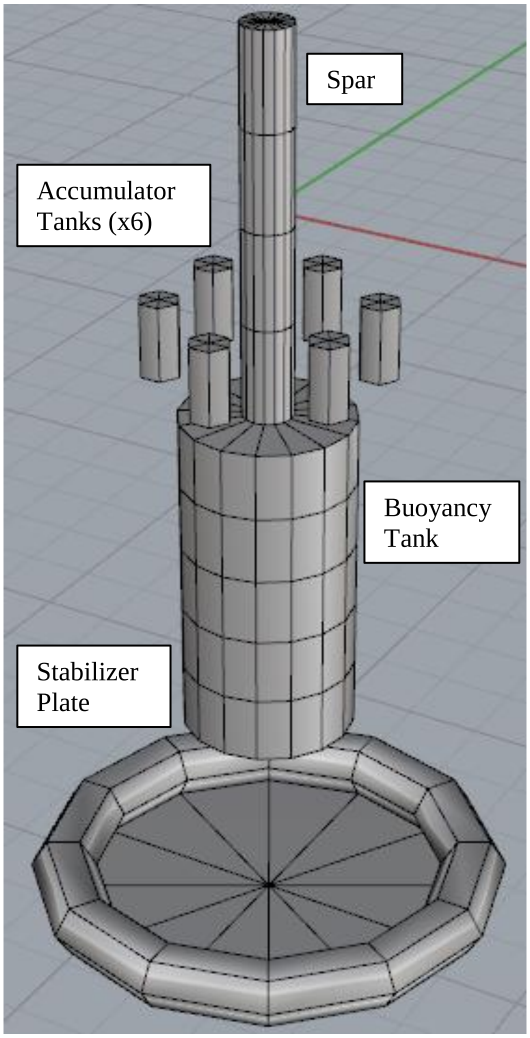

(a)

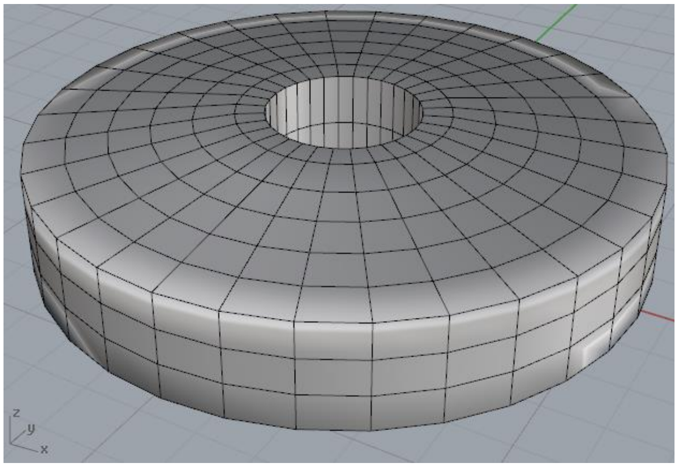

(b) Perspective view.

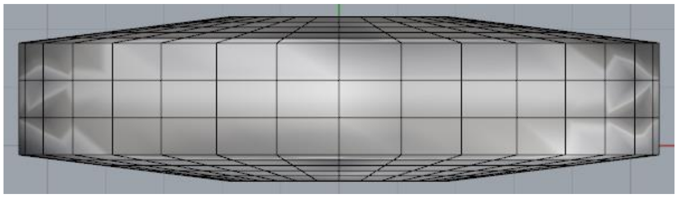

(b) Side view.

Figure 2.6: ProteusDS panel mesh for the (a) spar/stabilizer assembly and (b) float.

For the spar/stabilizer assembly, the accumulator tanks (as with WAMIT) are kinematically constrained in the positions that they would be on the actual system. However, while the component groupings are the same as those in WAMIT, these meshes differ slightly. In particular, ProteusDS requires the entire body to be included, not just the subsurface components. Furthermore, the ProteusDS mesh uses a coarser grid in order to improve computational speed within the time domain ProteusDS simulation.

Within a particular instance of the time domain simulator, ProteusDS independently solves the force balance equation given in Eq. 2.1 for both bodies at each time step, subject to the kinematic constraint of the float encircling the spar. This constraint is applied using the articulated body algorithm, for which the application of this numerical method to submerged systems is studied by Soylu [29].

$$F_{exc} + F_{rad} + F_{hydrostatic} + F_{drag} + F_{moorings} + F_{PTO} = (m + m_{\infty})\ddot{z} \tag{2.1}$$

For brevity, the equation is only given in the z-direction (heave) for a single device; however, it is solved in all six degrees of freedom, as well as for all three devices. With this in mind, the calculation procedure for each term is detailed; this procedure differs for both bodies as it factors in the nature of the expected dynamic response in order to further improve computation time.

The first term in the force balance is the excitation force, which is calculated as the sum of the diffraction (scattering) and Froude-Krylov forces. The Froude-Krylov force is calculated using the undisturbed wave field, as the integral of the dynamic pressure on each of the submerged body panels shown in Fig. 2.6. In the linearized WAMIT calculation, the mean water level is held constant, such that the Froude-Krylov force is proportional to the frequency-dependent instantaneous free surface elevation, using the coefficients given in Fig. 2.5. This can then be converted to the time domain with a linear superposition of the frequency components within the wave spectrum. For the spar, this is a sufficient level of accuracy, as the waterplane area on the spar/stabilizer assembly remains approximately constant. However, for the float the submerged water level is changing constantly; consequently, a linear calculation of the Froude-Krylov force is inacceptable. As a result, the Froude-Krylov force acting on the float is calculated using the instantaneous body position in ProteusDS; the dynamic pressure is subsequently integrated over the current set of wetted body panels.

Conversely, the diffraction is calculated for both bodies using WAMIT. Due to the relatively small size of the AOE converter relative to the wavelength, the contribution of diffraction to the total hydrodynamic force is small, so a frequency domain calculation of the diffraction force provides sufficient accuracy. To compute the diffraction force, the velocity potential is determined at each panel under the assumption that the wave field is undisturbed. The presence of the body is then accounted for through a secondary calculation of a new velocity potential that would prevent flow from occurring in the wall-normal direction (this secondary potential enforces the impermeable condition at the body wall). This diffraction potential is then summed over the entire set of panels, to produce a frequency-dependent diffraction force. The diffraction force is then computed in the time domain using the linear superposition of the diffraction force for all frequency components in the wave spectrum.

For the calculation of the radiation force in both bodies, frequency dependent added damping coefficients are inputted from WAMIT. From these coefficients, ProteusDS computes a kernel (impulse response) function, which demonstrates the decaying time domain response of each body to a unit impulse; the kernel function is calculated using Eq. 2.2 [30].

$$k_r(t) = \frac{2}{\pi}\int_0^\infty Bcos(\omega t)d\omega \tag{2.2}$$

Where the kernel function and frequency dependent damping coefficients are six-by-six matrices, which represent the impulse response in all six degrees of freedom from motion in an arbitrary direction. Using this impulse response function, the radiation force is then calculated in the time domain from the convolution integral of the kernel function and the body velocity; this is given in Eq. 2.3 for motion in the z-direction (heave) [30].

$$F_{rad}(t^*) = \int_0^{t^*} \dot{z}(\tau)k_r(t-\tau)d\tau \tag{2.3}$$

The convolution integral represents the time domain history as a series of impulses, each of which carry forward a time domain response that is dictated by the kernel function. As a result, the convolution integral incorporates the memory effects of previous body motion.

The hydrostatic (buoyancy) force is calculated using WAMIT in the case of the spar, and ProteusDS in the case of the float. In the linearized calculation, a hydrostatic stiffness (k_{hs}) is calculated in WAMIT, using a surface integral of the static pressure over the mean wetted body surface. The hydrostatic force can then be computed in the time domain using the difference in the current wave height and the mean water level, as given by Eq. 2.4 (for the z-direction).

$$F_{hs}(t) = k_{hs}(\eta(t) - z_{mean}) \tag{2.4}$$

This is sufficiently accurate for the spar, since the waterplane area is relatively constant. However, as with the Froude-Krylov force, this is not an acceptable approximation for the float. Consequently, the buoyancy calculation for the float is determined as the integral of the static pressure over the instantaneous wetted surface of the body, resolved in the time domain in ProteusDS.

Due to the highly nonlinear nature of viscous drag, F_{drag} is computed nonlinearly using ProteusDS for both the float and spar/stabilizer assembly. The drag force is computed for each panel, then is summed over the entire body using the instantaneous wetted surface. In computing the drag force, the drag coefficient, C_d, is specified as 1 for motion in each of the surge, sway, and heave directions. The drag force on a particular panel is given in Eq. 2.5 [31].

$$F_{drag} = \frac{1}{2}\rho C_d A_{panel} \cdot \vec{n} v^2 \tag{2.5}$$

Where $A_{panel} \cdot \vec{n}$ is the frontal projected area of the panel in the relative direction of fluid flow. In addition to being calculated on each panel, drag is also computed as a function of the relative motion between the float and spar, but this is computed as a portion of the PTO force. The PTO force is determined using a separate PTO model, described in Section 2.4, which is then passed to the float as the F_{PTO} forcing signal.

Due to the highly nonlinear nature of mooring forces, they are resolved in the time domain in ProteusDS. The AOE device uses three moorings, connected radially around the device. The mooring is connected to the sea-floor, which is assumed to be 50 m below the surface, at a 35 m horizontal distance from the centre of the body. The lines, beginning at the body, are composed of a 2 m spring (to prevent shock loading), 33.25 m of polymer, and 20 m of chain, for a total length of 55.25 m. A spherical external mass, with a 1.4 m diameter and 10060 kg mass, is also connected 35.25 m along the line, to create a catenary line structure. The properties of the mooring lines are summarized in Table 2.1.

Table 2.1: Properties of mooring lines.

Component	**Length [m]**	**Diameter [m]**	**Density [kg/m^3]**	**Axial Rigidity [N]**
Spring	2	0.01	1000	See Fig. 2.7
Polymer	33.25	0.05	720	5.2×10^7
Chain	20	0.0457	7700	6.56×10^8

For the spring component of the mooring, the axial rigidity is defined as a sixth order polynomial, in terms of the engineering strain. The tension in the spring as a function of engineering strain is given in Fig. 2.7.

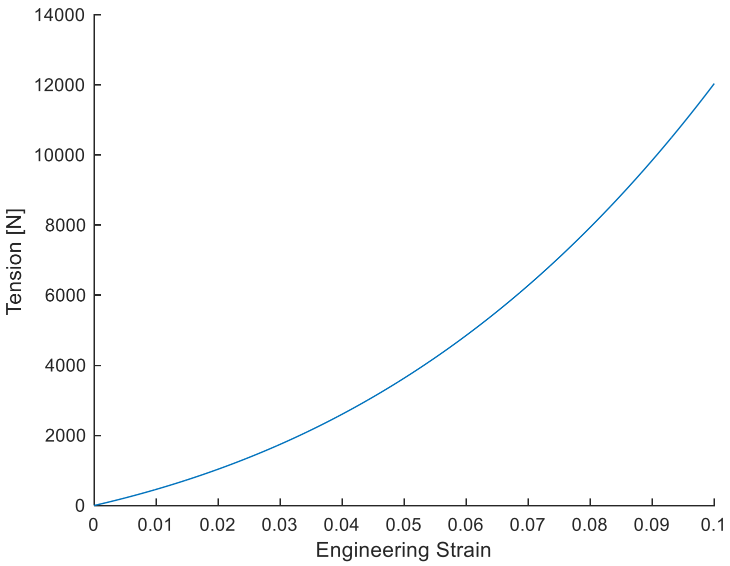

Figure 2.7: Tension as a function of engineering strain for spring component of mooring line.

A rendering of the mooring lines is given in Fig. 2.8.

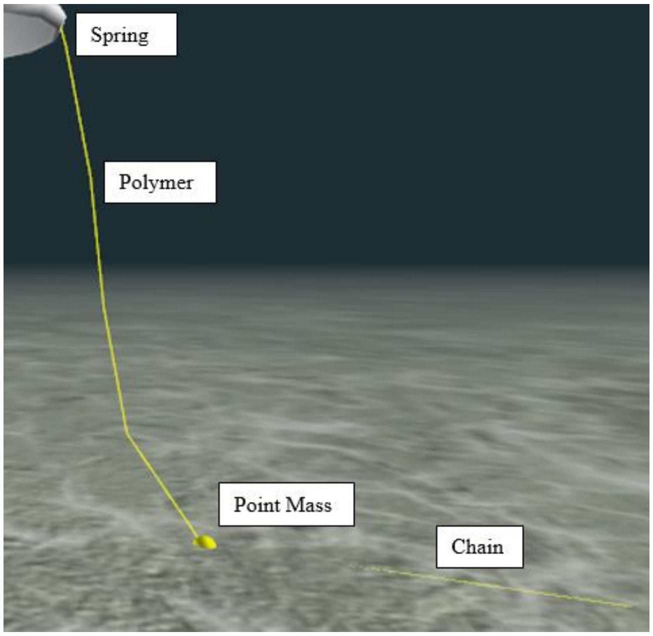

Figure 2.8: Rendering of mooring lines in ProteusDS.

A rendering of the complete WEC, including the float, spar/stabilizer assembly, and moorings is given in Fig. 2.9.

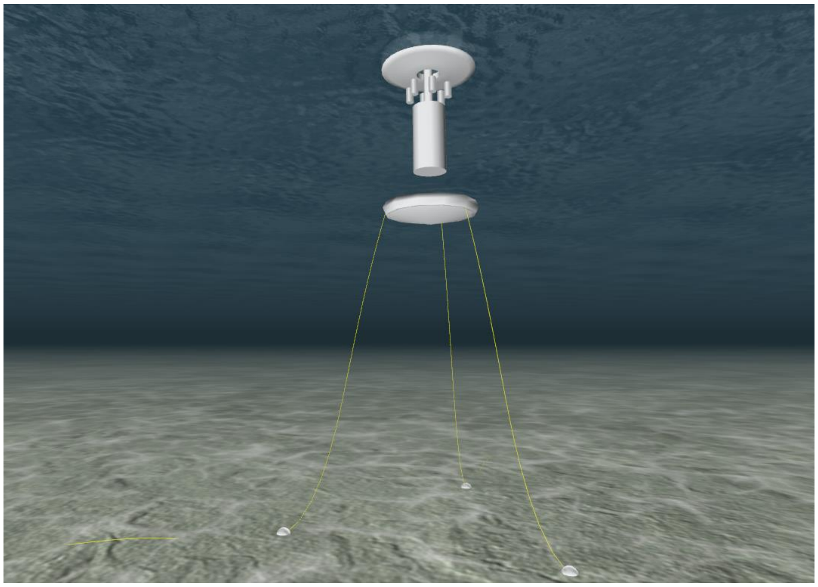

Figure 2.9: Rendering of complete WEC, including mooring lines, in ProteusDS.

The mooring forces are calculated using a finite-element method based on cubic-spline element geometry. The cable model employs a lumped mass approximation and calculates the hydrodynamic drag, added mass terms, weight, and seabed friction forces at the node points; this calculation procedure is given by Buckham [32]. The cable state is evolved with the WEC position and orientation, and cable element tensions are resolved using the node positions.

Once the forcing acting on both bodies is determined for a given time step, the wave data is subsequently updated. The wave data for each simulation is inputted directly as a series of individual wave frequencies, each with a particular wave height, period, phase, and heading. These individual frequencies are selected so that when aggregated together in a Pierson-Moskowitz (PM) spectrum, a desired significant wave height, energy period, and wave heading are produced; the PM spectrum is used, as it is representative of the spectral shape seen in actual sea-states off the BC coast [33]. The wave spectrum is then converted to the time domain by sampling the linear superposition of all frequency components at time 't'. For the simulations used in this thesis, a minimum of 140 wave frequencies were included in each wave spectrum, to ensure that a fully irregular, non-repeating sea-state is produced.

2.4 Power Take-Off Model

Due to the significant residency time of air within the power take-off, it is necessary to resolve the state of the air within the power take-off at each time step. However, it is not sufficient to merely resolve the state on the same time scale as the wave dynamics. In particular, while air passes between devices on the time scale of several wave periods, rapid transients due to valve opening/closing necessitate a smaller temporal resolution. Consequently, the PTO model must be able to handle a variety of time scales. Furthermore, the model must also provide a framework into which control can be introduced, which may introduce additional short time scale dynamics into the system. Consequently, the model of the power take-off was developed in MATLAB/Simulink. The PTO model is used to determine the complete internal state of the system, by resolving the dynamics of all piston cylinder chambers, tanks, pipes, and valves from the point at which air is drawn into the system to the point at which it is sent to shore. In contrast to the hydrodynamic (external dynamics) model, the internal dynamics of all three devices are resolved within the same simulation. Since air is readily passed between devices, the motion and resulting airflow of a particular device can have a significant impact on the dynamics of subsequent devices. To aid in understanding of how state information is passed between PTO components, the model structure of the first device are shown in Fig. 2.10.

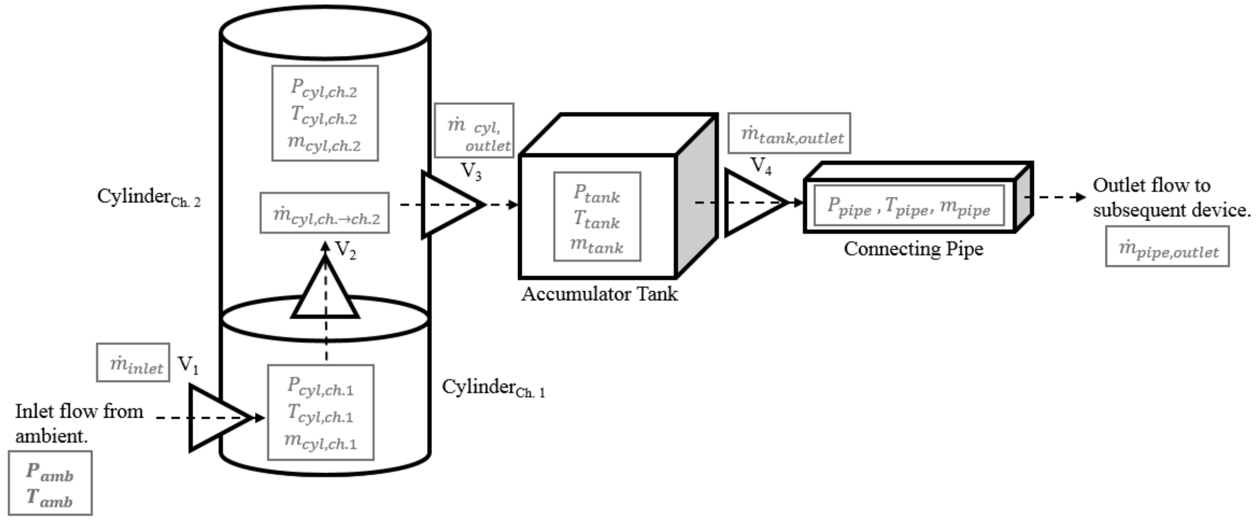

Figure 2.10: Representative illustration of PTO components, including key outputs of each component.

Each device is defined using pressure, temperature, and the mass of air within the component. The model contains the following components:

1. Cylinder, which is divided into two chambers that are separated by a unidirectional valve.
2. Accumulator tank(s), which store air prior to it being passed onto the next device. While the AOE device is designed to have six tanks, these tanks can be included separately or grouped together into a single block as necessary.
3. Valves (x4), which are unidirectional and prevent backflow. The valves are placed between each of the components, including at the entry and exit of each device configuration.
4. Connecting pipe, which passes air to the next device in the cascade. It is only included in devices 1 and 2.

There are several over-arching assumptions that govern the development of the thermodynamic equations in all of these components. The state of air is only resolved inside components that have a significant internal volume, and since there is no intermediate volume considered within the valves, no intermediate state is determined within the valve component. Instead, air is dumped instantaneously from the upstream to the downstream volume. In terms of the volumes themselves, it is assumed that ideal gas law applies, such that air has a constant ratio of specific heat and specific volume, such that $\gamma = \frac{c_P}{c_V} = 1.4$. In addition, it is assumed that the air within each component is at a single temperature and pressure (no gradients). This assumption is valid for relatively slow dynamic processes, and greatly expedites the computation of the air-flow dynamics within the PTO. Furthermore, this simplifies the calculation of heat transfer losses from each of the components, which is calculated using a constant heat transfer coefficient for the piston chambers, tank, and pipe. Lastly, it is assumed that all ambient air and water conditions are constant. Critical fluid properties, as well as the heat transfer coefficients of the PTO components, are given in Table 2.2. Dimensions of these components are not yet given, as they are defined in Chapter 3.

Table 2.2: Values for critical parameters used in model.

Variable	**Value**	**Variable**	**Value**	**Variable**	**Value**
$\boldsymbol{C_P}$	1005 J/kgK	$\boldsymbol{P_{atm}}$	101.3 kPa	$\boldsymbol{T_{atm}}$	293 K
$\boldsymbol{h_{cyl}}$, $\boldsymbol{h_{tank}}$, $\boldsymbol{h_{pipe}}$	0.2 W/mK	$\boldsymbol{R_s}$	288 J/kgK	$\boldsymbol{T_w}$	280 K
$\boldsymbol{\gamma}$	1.4				

The properties of air correspond approximately to those at the ambient air temperature, for which values are widely reported at 300 K [34]. These values are representative of dry air, which was a simplifying assumption used to establish a base case for measuring system performance. Furthermore, the chosen heat transfer coefficient is acknowledged to be a substantial simplification of heat loss from a piston cylinder; however, since the piston compression is driven by relatively slow wave motion, the temperature gradients within the piston cylinder are assumed to be small. In future work it may be possible to resolve the temperature gradients, inevitably leading to a substantial loss in computational speed, but for which both the inner and outer wall temperature can be accurately determined. When considering the tank and pipe, the heat coefficient is believed to be a conservative estimate, particularly when considering that in addition to thermal resistance from the device walls and insulation, heat transfer to the ocean surface is dominated by free convection. However, since wall thicknesses are not known, a more accurate estimate could not be obtained.

Under the influence of these assumptions, it is possible to determine the PTO reaction force, which affects the motion of the float governed by Eq. 2.1. Incorporating additional friction effects, the total PTO reaction force is given by Eq. 2.6.

$$F_{PTO} = F_{piston} + F_{end-stop} + F_{friction} \tag{2.6}$$

This force is passed to the ProteusDS model at the same rate as the hydrodynamic calculations: 500 Hz. The force applied from the pressure differential across the piston is described in conjunction with the cylinder model in the following section. The end-stop forces are applied using mass-spring damper equations, to prevent numerical instabilities arising from the effect of highly nonlinear collision dynamics. Collisions create rapid transients as a result of extreme forces; these forces have the potential to generate oscillations in the piston motion if applied instantaneously. Instead, the end-stop forces are applied progressively using a mass-spring damper if the float moves within 5% of the end of the piston cylinder, as given by:

$$F_{end-stop,low} = k_{end-stop}\left(z_{limit} - z_{float}\right) - c_{end-stop}\dot{z}_{float} \tag{2.7}$$

$$F_{end-stop,high} = -k_{end-stop}\left(z_{float} - \left(L_{cyl} - z_{limit}\right)\right) - c_{end-stop}\dot{z}_{float} \tag{2.8}$$

Where $k_{end-stop} = 5 \text{ x } 10^6$ and $c_{end-stop} = 5 \text{ x } 10^7$. Coulomb friction is also applied to the motion of the piston, and is given by:

$$F_{friction} = \text{minimum}\begin{cases} -k_{friction}\dot{z} \\ -400D_{cyl} \end{cases} \tag{2.9}$$

Where $k_{friction} = 10^5$. The magnitude of coulomb friction is typically several orders of magnitude smaller than the force applied by the pressure difference across the piston face. To determine F_{piston}, the pressure within the cylinder is resolved using a full dynamic model of the components of the PTO.

2.4.1 Cylinder

The airflow within the cylinder as a function of the wave height is given in Fig. 1.3. Resolving the airflow through the cylinder is necessary for calculating the PTO force as well as the pressure of compressed air produced by the WEC (and eventual useful power output). To calculate the pressure within the cylinder, it is necessary to determine the mass flow rate, temperature, and pressure of air flowing into and out of both chambers at each time step. Using this state information, the pressure of both chambers can be determined independently by integrating the following differential equations which are based on ideal gas law [35]. Eq. 2.10a is used for the lower piston chamber (chamber 1), while Eq. 2.10b governs the upper piston chamber (chamber 2).

$$\frac{dP_{cyl,ch.1}}{dt} = \frac{1}{V_{cyl,ch.1}}\Big[\gamma P_{cyl,ch.1}\, A_{cyl}\dot{z} - (\gamma - 1)h_{cyl}a_{cyl,ch.1}\left(T_{cyl,ch.1} - T_w\right) + \gamma R_s T_{amb}\dot{m}_{inlet} - \gamma R_s T_{cyl,ch.1}\dot{m}_{cyl,ch.1\rightarrow ch.2}\Big] \tag{2.10a}$$

$$\frac{dP_{cyl,ch.2}}{dt} = \frac{1}{V_{cyl,ch.2}}\Big[-\gamma P_{cyl,ch.2}\, A_{cyl}\dot{z} - (\gamma - 1)h_{cyl}a_{cyl,ch.2}\big(T_{cyl,ch.2} - T_w\big) + \gamma R_s T_{cyl,ch.1}\dot{m}_{cyl,ch.1\rightarrow ch.2} - \gamma R_s T_{cyl,ch.2}\dot{m}_{cyl,outlet}\Big] \tag{2.10b}$$

The mass flow rate in/out of the cylinder chambers is defined by the cylinder valve dynamics, which are described in Section 2.4.4. The time rate of change in pressure is also affected by heat loss from the piston cylinder, which is governed by one-dimensional heat conduction with a constant heat transfer coefficient, h_{cyl}; the value of this coefficient is given in Table 2.2, along with other fluid properties. Lastly, the pressure gradient computed in Eq. 2.10 is scaled by the volume of the piston chamber. The volumes of the two piston chambers, as a function of the current piston position, are given by Eq. 2.11a and Eq. 2.11b, respectively.

$$V_{cyl,ch.1} = A_{cyl}(-z + L_{cyl}) \tag{2.11a}$$

$$V_{cyl,ch.2} = A_{cyl}\big(z + L_{cyl}\big) \tag{2.11b}$$

The mass of air in the two cylinder chambers is given as the integral of Eq. 2.12a and Eq. 2.12b, respectively.

$$\frac{dm_{cyl,ch.1}}{dt} = \dot{m}_{inlet} - \dot{m}_{cyl,ch.1\rightarrow ch.2} \tag{2.12a}$$

$$\frac{dm_{cyl,ch.2}}{dt} = \dot{m}_{cyl,ch.1\rightarrow ch.2} - \dot{m}_{cyl,outlet} \tag{2.12b}$$

With the pressure, mass, and volume determined, the updated temperature of both chambers can then be determined using ideal gas law, as given by 2.13a and 2.13b for the lower and upper piston chamber, respectively:

$$T_{cyl,ch.1} = \frac{P_{cyl,ch.1}V_{cyl,ch.1}}{m_{cyl,ch.1}R_s} \tag{2.13a}$$

$$T_{cyl,ch.2} = \frac{P_{cyl,ch.2}V_{cyl,ch.2}}{m_{cyl,ch.2}R_s} \tag{2.13b}$$

Furthermore, the contribution of this pressure differential to the PTO force can be calculated.

$$F_{piston} = (P_{cyl,ch.2} - P_{cyl,ch.1})\, A_{cyl} \tag{2.14}$$

With the state of air within the cylinder determined, it is now possible to resolve the continued flow of air through the system. In particular, air is passed to the air storage tanks if the pressure in the second (upper) piston chamber exceeds the subsequent air storage tank, such that $P_{cyl,ch.2} > P_{tank}$. In this case, the valve is opened and mass is allowed to flow instantaneously into the subsequent tank.

2.4.2 Air Storage Tanks

Once air passes through the cylinder, it is stored in one of six accumulator tanks. Separate pressures can be maintained in each tank if necessary, or the tanks can be grouped together to produce a single volume. Grouping the tanks into a single volume is the default configuration in the absence of active control. However, in the case of active control implementation, there is an option to dump air instantaneously from the upper piston chamber to any of the tanks (provided a favourable pressure differential exists). Furthermore, air can be selectively drawn from a single tank to the single downstream pipe, provided the tank pressure exceeds that of the pipe. The role of variable pressure tanks in the active control strategy is described in further detail in Section 4.4.

The pressure is calculated as the integral of Eq. 2.15; this is valid for both the grouped volume and individual accumulator tanks provided the volume is adjusted accordingly.

$$\begin{aligned}\frac{dP_{tank}}{dt} = \frac{1}{V_{tank}}\Big[&-(\gamma - 1)h_{tank}a_{tank}(T_{tank} - T_w) + \gamma R_s T_{cyl,ch.2}\dot{m}_{cyl,outlet} \\ &- \gamma R_s T_{tank}\dot{m}_{tank,outlet}\Big]\end{aligned} \tag{2.15}$$

The three terms are dependent on mass flow into/out of the tank, as well as heat loss through the tank wall. The heat transfer through the tank wall is steady state conduction, with a constant heat transfer coefficient given in Table 2.2. It is assumed that conduction through the tank wall is the dominant thermal resistance. Once the pressure is calculated, the mass of the tank is determined by integrating Eq. 2.16.

$$\frac{dm_{tank}}{dt} = \dot{m}_{cyl,outlet} - \dot{m}_{tank,outlet} \tag{2.16}$$

Using the tank mass and pressure, the tank temperature is determined using ideal gas law, as given in Eq. 2.17.

$$T_{tank} = \frac{P_{tank}V_{tank}}{m_{tank}R_s} \tag{2.17}$$

Air is stored in this combined volume until the tank pressure exceeds that of the subsequent connecting pipe to the next device in the WEC, such that $\mathrm{P_{tank}} > \mathrm{P_{pipe}}$. In the case of the third device, no pipe exists, so air is held within the tank until the crack pressure of the cascade is exceeded.

2.4.3 Connecting Pipes

Once air passes through the accumulator tank(s), it is temporarily stored in a connecting pipe, prior to being passed onto the next device. The power take-off model includes the connecting pipes between the first and second, as well as the second and third devices. The function of the pipe model is to capture temperature losses due to the large surface area that is exposed to ambient ocean conditions. Head losses due to the velocity of the air are considered negligible due to the density of the pressurized air, relatively large pipe diameter, and relatively small pipe length. Furthermore, as a result of the small pipe length, the velocity and pressure gradients within the pipe are also assumed to be negligible.

As a result of these simplifications, it is not necessary to resolve the velocity within the pipe; this allows each pipe to be treated as a fixed volume tank, which is at a single temperature and pressure. The diameter of the pipe is assumed to be the same as the inlet valve orifice, which varies with each device. Conversely, the pipe length is fixed at 70 m; this is the spacing between devices. The pipe pressure is given by integrating Eq. 2.18.

$$\frac{dP_{pipe}}{dt} = \frac{1}{V_{pipe}}\left[-(\gamma - 1)h_{pipe}a_{pipe}\left(T_{pipe} - T_w\right) + \gamma R_s T_{tank}\dot{m}_{tank,outlet} - \gamma R_s T_{pipe}\dot{m}_{pipe,outlet}\right] \tag{2.18}$$

The heat loss through the pipe wall is treated the same as for the tank, since the velocity within the pipe is not resolved. The mass of air within the pipe is given by integrating Eq. 2.19.

$$\frac{dm_{pipe}}{dt} = \dot{m}_{tank,outlet} - \dot{m}_{pipe,outlet} \tag{2.19}$$

The temperature can then be given by ideal gas law, as illustrated in Eq. 2.20.

$$T_{pipe} = \frac{P_{pipe}V_{pipe}}{R_s} \tag{2.20}$$

The flow in/out of the pipes is governed by a pair of unidirectional valves, for which the set of governing equations are given in the subsequent section.

2.4.4 Valves

The components of the WEC PTO are separated by a series of valves, which are used to ensure unidirectional flow through the system. The location of the valves within a single device are indicated in Fig. 2.10. The valves do not introduce a pressure loss, as this would require resolving the pressure gradient within each PTO component in order to determine flow velocity; instead, flow is allowed to occur whenever a favourable pressure gradient exists, subject to a series of flow limits. The first, $\dot{\mathrm{m}}_{\mathrm{max}}$, depends on the area available for airflow as well as state of the air. The second, $\dot{\mathrm{m}}_{\mathrm{control}}$, is based on the implementation of an active control strategy, while the last limit, $\dot{\mathrm{m}}_{\mathrm{model}}$, is an artificial model-based flow constraint used to ensure numerical stability. When considering each of these flow limits, the actual flow rate is given by Eq. 2.21.

$$\dot{\mathrm{m}} = \mathrm{minimum}\begin{cases}\dot{\mathrm{m}}_{\mathrm{max}}\\ \dot{\mathrm{m}}_{\mathrm{control}}\\ \dot{\mathrm{m}}_{\mathrm{model}}\end{cases} \tag{2.21}$$

The maximum mass flow rate through the valve, calculated as a function of the state of the air and orifice area, is given by Eq. 2.22 [36].

$$\dot{m}_{max} = \begin{cases} \frac{A_{orifice}P_{upstream}2\gamma}{(\gamma - 1)R_s T_{upstream}}(\beta^{\frac{2}{\gamma}} - \beta^{\frac{\gamma+1}{\gamma}})^{0.5}, \beta > 0.5283 \\ \frac{0.0404A_{orifice}P_{upstream}}{T_{upstream}^{0.5}}, \beta \leq 0.5283 \end{cases} \tag{2.22}$$

Where β is the pressure ratio across the valve, $\frac{P_{downstream}}{P_{upstream}}$, which defines the nature of the flow as subsonic and sonic respectively. Instead of providing a separate equation for each valve in the model, the mass flow rate is defined as a function of the upstream/downstream air states. In the case of flow from the upper piston chamber to the tank, the upstream volume is the cylinder chamber, while the downstream volume is the tank, such that $\beta = \frac{P_{tank}}{P_{cyl,ch.2}}$.

The control-defined flow limit is dependent on the particular control strategy being applied. For the present study, there are two primary regimes of valve control: passive and active control. In the passive control regime, the control flow limit is not applied. However, in the active control regime, the control strategy introduces additional flow limitations, which are presented in Section 5.4.2. These flow limitations include the time dependence of valve opening, which is not considered in the passive system in order to provide an optimal base case.

The last flow limit is $\dot{m}_{model}$, which is applied to ensure numerical stability in the simulation. The need for an artificial model-based flow limit arises from the assumption that all tanks and pipes are at a single temperature and pressure. In the absence of internal pressure gradients, it is possible for the pressure gradient across a valve to reverse instantaneously. This is in contrast to real pressure vessels, for which the existence of gradients ensures the pressure downstream of a valve does not instantly build when mass is received through a valve. Since the flow through the simulated valves is unidirectional, the reversal of the pressure gradient prevents flow from occurring, which creates high frequency pulses of the flow through the simulated valve.

These fluctuations arise if the valves exhaust a significant percentage of the upstream volume in a given time step. The increase in downstream pressure, coupled with a drop in the upstream pressure, will reverse the pressure gradient across the valve in the subsequent time step.

However, as air continues to flow into the upstream volume, the upstream pressure will increase until the process repeats. For high flow rates simultaneously occurring into and out of a single volume, the return to a favourable pressure gradient may only take 1-2 time steps, which produces a series of oscillations in the flow rate on the magnitude of 2-3 time steps, or 0.004 – 0.006s.

It is clear to see that these oscillations are non-physical. However, allowing significant pressure build-up across the valve in order to prevent these numerical oscillations is also unacceptable, as this will lead to erroneous WEC performance losses. In an effort to prevent the formation of numerical instabilities, while simultaneously preventing the formation of pressure build-up across the valve, the model-based flow limit was applied. The application of $\dot{\mathrm{m}}_{\mathrm{model}}$ requires determining the mass flow rate that would create equal pressure across the valve, $\dot{\mathrm{m}}_{\mathrm{opt}}$. This optimal mass flow rate can be determined using a valve-dependent set of ideal gas law based equations, which are listed in Appendix A. However, a sample equation for the optimal mass flow rate is given in Eq. 2.24. This formula is for flow between the cylinder and air storage tank.

$$\begin{aligned}\mathrm{P}_{\mathrm{opt,cyl\,outlet}} = \left(\frac{\Delta\mathrm{t}}{\mathrm{V}_{\mathrm{tank}} + \mathrm{V}_{\mathrm{cyl,ch.2}}}\right)\Bigg[&\frac{\mathrm{P}_{\mathrm{tank}}\mathrm{V}_{\mathrm{tank}}}{\Delta\mathrm{t}} - \gamma\mathrm{P}_{\mathrm{cyl,ch.2}}\dot{\mathrm{z}}\mathrm{A}_{\mathrm{cyl}} \\ &- (\gamma-1)\mathrm{h}_{\mathrm{cyl}}\mathrm{a}_{\mathrm{cyl,ch.2}}\left(\mathrm{T}_{\mathrm{cyl,ch.2}} - \mathrm{T}_{\mathrm{W}}\right) - (\gamma-1)\mathrm{h}_{\mathrm{tank}}\mathrm{a}_{\mathrm{tank}}(\mathrm{T}_{\mathrm{tank}} - \mathrm{T}_{\mathrm{W}})\Bigg]\end{aligned} \tag{2.23}$$

$$\begin{aligned}\dot{\mathrm{m}}_{\mathrm{opt,cyl\ outlet}} = \left(\frac{1}{\mathrm{R}_{\mathrm{s}}\mathrm{T}_{\mathrm{cyl,ch.2}}\gamma}\right)\Bigg[&-\frac{\left(\mathrm{P}_{\mathrm{opt,cyl\,outlet}} - \mathrm{P}_{\mathrm{cyl,ch.2}}\right)\mathrm{V}_{\mathrm{cyl,ch.2}}}{\Delta\mathrm{t}} - \gamma\mathrm{P}_{\mathrm{cyl,ch.2}}\dot{\mathrm{z}}\mathrm{A}_{\mathrm{cyl}} \\ &- (\gamma-1)\mathrm{h}_{\mathrm{cyl}}\mathrm{a}_{\mathrm{cyl,ch.2}}\left(\mathrm{T}_{\mathrm{cyl,ch.2}} - \mathrm{T}_{\mathrm{W}}\right)\Bigg]\end{aligned} \tag{2.24}$$

The optimal pressure is determined first (Eq. 2.23), which is the pressure that the cylinder and tank will both equal in the subsequent time step, provided that the highest allowable (optimal) mass flow occurs. This pressure is then used to determine the optimal mass flow rate. To ensure numerical stability, the model-based flow limit is then selected as 99% of the optimal mass flow rate through the valve; this was to ensure the flow rate was as close to optimal as possible while ensuring numerical stability. Therefore, the model-based flow limit at each time step is given by:

$$\dot{m}_{\mathrm{model}} = 0.99\dot{m}_{\mathrm{opt}} \tag{2.25}$$

The PTO model structure is designed to resolve the complete state of air at each time step of the simulation. As described in the valve and tank dynamics, the model includes the necessary features to implement a control strategy that improves the performance of the AOE device. When coupled with the ProteusDS model, the model provides a holistic representation of the AOE WEC.

2.5 On-Shore Generator System

Incorporating knowledge of the on-shore generation system allows for the development of holistic control strategies that don't inherently reduce generator performance as the result of introducing sub-optimal upstream control laws. Therefore, while the modelling of the on-shore generation system is not within the scope of the current work, it is important to consider limitations on the state of the air that is passed to shore; of particular interest are bounds on the pressure, temperature, and quantity of mass-flow from the WEC. To identify these limits, a potential on-shore generation system was identified. This was followed by a brief overview of the primary limitations on the on-shore equipment, in order to inform potential bounds on the operation of the control strategy.

2.5.1 On-shore Generation Architecture

The conversion of compressed air to electricity is well-developed, and there are several commercial technologies for this process. Of greater concern is the significant challenge of incorporating the intermittent wave energy resource to the grid [12], in a manner that facilitates the use of compressed air. To this aim, compressed air energy storage (CAES) systems provide a method for matching intermittent renewable energy sources with variable demand, in a manner that provides high reliability, economic feasibility, and low environmental impact [37]. In addition to the two commercial plants that have been developed to date (in 1978 and 1991), novel methods have been proposed for introducing CAES systems in new applications, such as for the buffering the intermittency of renewable technologies, even on small generation scales [38]. As a result, CAES technology was targeted as a generic model architecture for the AOE on-shore electricity conversion system.

The conventional CAES concept uses low-cost electricity from the grid at off-peak times to produce compressed air; this air is then stored either in underground caverns or above-ground vessels. Using the stored compressed air in conjunction with a standard air turbine, power can be produced as needed in order to match electricity demand. Several variations on this conventional diabetic concept exist, including adiabatic or isothermal CAES systems, as well as tri-generation micro-CAES configurations [37] [38]. A review of the state of the CAES technology is provided by Rogers et al [38]. The CAES architecture used in the AOE system will differ from standard CAES systems, which use grid power to produce the compressed air, while the AOE WEC will provide compressed air directly. Furthermore, several options exist for AOE in terms of the way this compressed air is used, which are not yet resolved: either air may be passed directly through a turbine for zero-emission electricity generation, or it may be pre-heated using either fossil fuel combustion or excess grid power in order to increase efficiency. However, despite these variations on the conventional concept it is clear that these developments in CAES technology are applicable to the AOE WEC, as they provide novel methods to improve the efficiency of extracting power from compressed air. Furthermore, the storage innovations made with the CAES technology are critical for the buffering the intermittent supply of electricity that is inherent to the wave energy resource.

2.5.2 Design Constraints on CAES systems

To gain an understanding of the critical parameters included in the CAES generation architecture, a CAES model is provided by Struchtrup [39]. Even this basic structure contains a number of parameters that significantly affect performance, such as efficiencies/dimensions of the turbine, regenerator, and combustion chamber, as well as the volume and thermal resistance of the storage tank. However, not all of these parameters directly limit the nature of airflow to shore. Since a wide range of storage opportunities are available [38], storage induced restrictions on the quantity of airflow to shore are not considered. Furthermore, since the particular CAES architecture is not resolved, and the regenerator and combustion chamber are not mandatory inclusions in the CAES system, limitations on the nature of airflow induced from these components are not considered. However, it is important to still consider limitations from the air turbine itself, as the efficiency of this component is a primary determinant of the power that is extracted from the compressed air. If the application of the control strategy shifts the performance of the turbine into an undesirable operating range, then any performance gains achieved with the control strategy may not result in increases in electricity production. This consideration prompted a review of the air motor/turbine industry, in order to identify ranges of feed-in temperatures, pressures, and mass-flow rates.

The review is structured in two sections, as devices can be largely grouped into two categories: air turbines and air motors. Air turbines are designed specifically for the production of electricity, and are typically designed for large-scale operation. Conversely, air motors are designed for a larger scope of applications, and are seldom restricted to a single function; however, these applications are typically for smaller scale installations. When grouped onto a logarithmic curve of mass-flow rate and power production, however, it can be seen that these two industries collapse onto the same curve, as seen in Fig. 2.11.

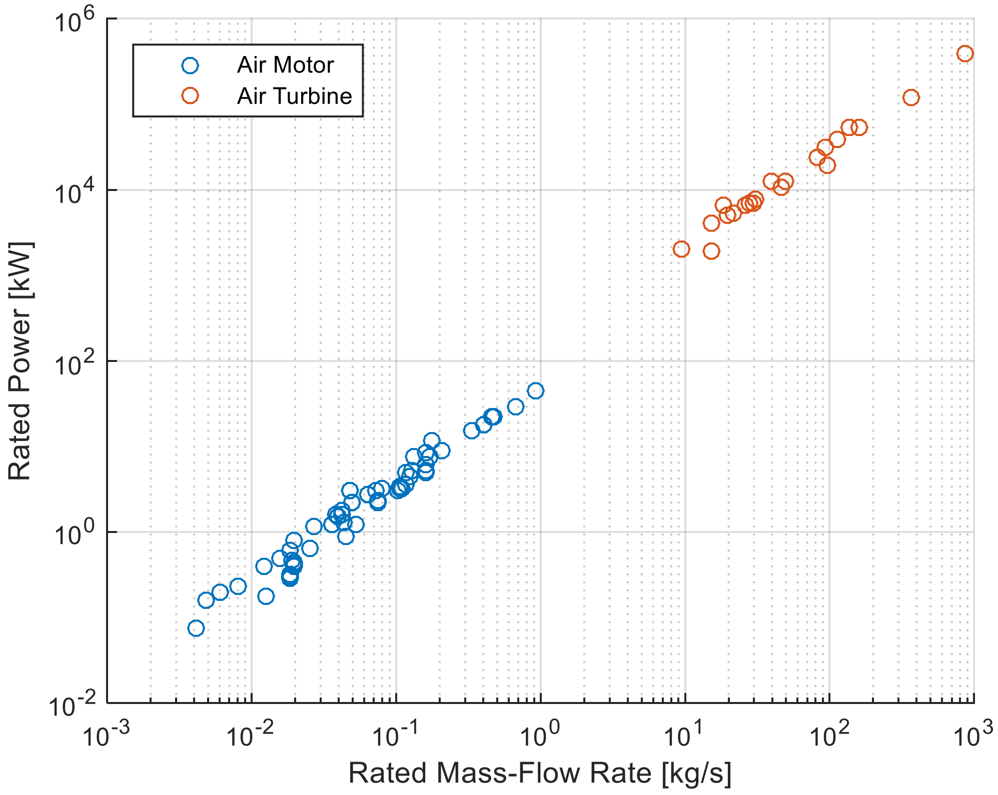

Figure 2.11: Summary of air turbine and air motor industry set-point data.

The two power/mass-flow relationship for both industries collapses onto the same curve when plotted on a logarithmic scale; notably, this correlation is irrespective of turbine geometry and operating pressure and temperature. As a result, it is not yet necessary to restrict the on-shore turbine configuration into one of these two industry categories. Instead, merely the limitations on the aggregate of both industries need to be considered. To obtain these limits, the set-point performance of a variety of motors/turbines, spread over multiple manufacturers, were considered. In particular, data on the pressure ratio, mass-flow rate, and power output of a number of was gathered. The mass flow rate is of particular interest, as it defines the minimum mass-flow that must be passed to shore in order for power to be generated. Furthermore, the pressure ratio defines the minimum/maximum supply pressure that must be passed to shore. The range of these design variables is given in Table 2.3.

Table 2.3: Range of air turbine/air motor industry set-points.

Manufacturer	**# of Devices Considered**	**Power [kW]**		**Mass-Flow Rate [kg/s]**		**Pressure Ratio**	
		Low	**High**	**Low**	**High**	**Low**	**High**
Air Motors							
Atlas Copco **[40]**	14	0.16	5.22	0.005	0.159	6.30	6.30
Deprag **[41]**	6	1.60	18.00	0.039	0.408	6.00	6.00
Ingersoll Rand **[42]**	8	0.47	22.37	0.019	0.474	6.21	6.21
MODEC **[43]**	8	1.25	3.00	0.036	0.048	6.00	6.00
Parker **[44]**	11	0.07	18.00	0.004	0.408	6.00	6.00
PSI Automation **[45]**	16	0.30	44.74	0.018	0.913	6.21	6.21
Air Turbines							
Dresser Rand **[46]**	2	1934	2000	9.5	15	4.00	7.00
MAN Turbo **[47]**	4	6630	10500	26.2	46.5	Unknown	
Siemens	15	5100	400000	19.5	869	10.2	33.6
Net Range							
		0.07	400000	0.005	869	4.00 (6.00)	33.6

As seen with the size of the summarized ranges, there is not expected to be any concern in staying within industry limits for mass-flow. However, the lower limit on the pressure ratio is not insignificant. The limit corresponds to a 4 bar supply pressure; however, this supply pressure is used in a 2 MW turbine, which is much higher than what can be achieved with the AOE device. Consequently, the 6 bar pressure limit seen in the air motor industry provides a more realistic lower pressure bound. Therefore, in order to ensure that the air supplied by the AOE device can be converted to electricity, the 6 bar lower pressure limit must be carried forward to the implementation of control in the AOE device.

2.6 Calculation of Power Output: Flow Exergy

Since the on-shore generation architecture is not fully resolved in the current system, the WEC power output is computed as a function of exergy; exergy describes the potential to do useful work. In contrast to energy, which is merely converted from one form to another, exergy is not necessarily conserved. In particular, exergy can be destroyed if there is an increase in entropy (disorder of the system). Accounting for this increase in disorder incorporates the fact that not all energy is useful. For example, pressure increases through heating cannot be converted to electricity as easily as an isothermal pressure increase from compression, as the temperature change results in an increase in the disorder of the system. Consequently, isothermal compression has a higher exergy.

In addition to exergy being representative of the potential of the outputted air to do work, this metric was selected as is not dependent on the geometry of the on-shore generation system. Some of the inherent difficulties in resolving the on-shore generator are described in Section 2.5. Instead, the calculation is based on the flow exergy of the air exiting the converter, which is given by [39]:

$$e = [h_{out} - h_{amb}] - T_{amb}(s_{out} - s_{amb}) \tag{2.26}$$

This expression can be rearranged to the following using ideal gas law:

$$e = C_p T_{amb}\left(\frac{T_{out}}{T_{amb}} - 1 - ln\left(\frac{T_{out}}{T_{amb}}\right)\right) + R_s T_{amb} ln\left(\frac{P_{out}}{P_{amb}}\right) \tag{2.27}$$

The flow exergy is then converted to the power output of the WEC using the mass flow output from the third device, as given by Eq. 2.28.

$$Power = \dot{m}_{tank,outlet}e \tag{2.28}$$

Since the power output is computed as a function of flow exergy, exergy has the units of power (watts); this is in contrast to closed system exergy, which has the units of energy (joules). To ensure clarity in subsequent discussions, the use of the term ‘exergy’ is taken to be flow exergy, unless otherwise stated.

2.7 Summary of the AOE Model Architecture

A dynamically coupled model architecture of the AOE WEC was developed using the finite element solver ProteusDS and MATLAB/Simulink. The model resolves the hydrodynamic, PTO, and mooring forcing acting on the three devices within the AOE WEC, which is then used to determine the complete state of the system at each time step of the simulation. Through the tracking of system states, the performance of the WEC can be monitored in real-time as a function of the current wave condition. In particular, the time-dependent change in the state of air within the piston chambers, tank, and pipes allows for the assessment of the impact of the geometry of these devices on performance. Furthermore, the impact of dynamic changes in the valve timing and selective tank throughput provides real-time evaluation of the effect of controllable geometries on WEC performance. In doing so, the developed model architecture allows for implementation and assessment of both passive and active control.

In addition to enabling control development for the current work, the application of this approach to a system with the complexity of the AOE WEC is a valuable contribution to WEC modelling literature. Prior to this work, no modelling approaches had been identified with sufficient fidelity and computational speed to resolve the real-time state of particular PTO components within multiple WEC devices. In doing so, the complexity of the modelling architecture was extended beyond that of Bailey et al [6] [27], to include the dynamic coupling of multiple WEC devices. To ensure the accuracy of the simulations, the model made use of experimentally verified hydrodynamic software [21], as well as literature-based thermodynamic calculations [35] [36]. Consequently, the model is assumed to be sufficiently accurate to test and implement both passive and active control strategies.

Chapter 3. Passive Control: Problem Formulation

The question of how to improve the performance of a wave energy converter presents a significant challenge, in large part due to complex nature of the changing wave environment. In addition to differences in the wave resource with changing deployment location, the wave resource at a single point changes on a spectrum of time scales. Intelligent device design can improve performance on large time-scales, such as seasonal variation, however, the study of control is crucial for maximizing power capture on a sea-state or wave-by-wave basis.

Conventionally, control is applied as variation in the operation of the device PTO, which in the AOE device presents a highly complex control problem. As described in Chapter 2, the operation of the AOE WEC is highly nonlinear; in particular, due to the cascaded nature of the device, minute changes in the PTO are expected to have significant impacts as these perturbations magnify in downstream devices. Therefore, it is not sufficient to select the geometry of the PTO arbitrarily for the purpose of implementing active control. Rather, the PTO geometry is the primary determinant of the PTO force, for which active control provides a method of perturbing the forcing signal in order to produce desirable characteristics on shorter timescales. Consequently, focus was first placed on the introduction of passive PTO force control. For this work, the passive control regime is viewed as an exercise in a priori selection of critical PTO parameters that produce the highest annual energy output for a particular deployment location. This definition of control aligns with that of Price [48], who note that while the term ‘PTO force control’ has taken on a variety of meanings in literature, it is conventionally viewed as an optimization of the PTO settings for the maximization of power output.

In practice, this reduces to an optimization problem, which has prompted a review of optimization techniques in wave energy literature. This is followed by the selection of eight critical design variables that are deemed most critical in optimizing airflow through the piston chambers, tanks, pipes, and valves that compose the PTO system. The optimization algorithm is then described, including how wave resource data from the Amphitrite Bank deployment location was included in creating a location-specific estimate of the annual power output.

3.1 Literature Review of WEC Optimization

While it has long been known that the performance of wave energy converters is highly dependent on the WEC geometry, loosely summarized as the fact that for a WEC to be a good absorber, it must also be a good wave generator [9], no universal laws exist for producing an optimal design. In part, this is due to the fact that no single WEC architecture has yet been identified as optimal, which has diluted research across a variety of devices [12]. Perhaps more importantly, however, there are a number of complex challenges in optimizing a highly nonlinear system, as well as meeting the necessary computational requirements. In particular, each WEC incorporates a variety of external geometries and PTO characteristics that must be selected intelligently in order to take full advantage of the particular device’s technological innovations. As an industry, taking advantage of these gains is a necessary step in penetrating the renewable energy market. Consequently, a large body of work has developed on creating methodologies for optimizing device geometries and PTO parameters, as well as the application of these procedures to particular devices. The breadth of research in the WEC optimization field has enabled a progression not only in the complexity of the optimization procedure, but the level of modelling fidelity with which the optimization is conducted. In order to best describe the current state of the field, a review of general optimization studies is presented, followed by those that add layers of complexity and specificity.

At the most widest level of applicability, studies have focused on optimizing generic WEC geometries, by using brute force simulations to assess the optimality of certain characteristics in generic sea-states [49] [50] [51] [52]. In order to manage the high computational requirements of these brute force studies, models are typically linearized or created with sufficiently low fidelity to allow numerous simulations to be conducted. For example, Ricci et al [49] optimized the external geometry and PTO damping coefficient of a single axisymmetric body in heave, which was then incorporated into a study on array spacing and shape. The optimization was conducted using a linear frequency domain hydrodynamic model in heave only, for which the PTO was modelled as a linear damper. Similarly, Zhang et al [50] optimized the external geometry of an axisymmetric point absorber. To study multiple geometries, Zhang et al [50] performed a semi-analytical decomposition of the body into a series of surfaces, which allowed the body to be modelled in the frequency domain. Bouali and Larbi [51] optimized the geometric configuration, followed by the specific geometry, of the front wall of an OWC converter. The simulations were conducted with CFD, using a simplified geometry that resolved the front wall and air vent. Gomes et al [52] optimized the OWC chamber geometry with the application of Constructal Design fundamentals. The OWC device was modelled using CFD, with head losses across the turbine being accounted for; however, the turbine itself was not resolved.

While the results of the above studies are sufficiently general that they can be applied to a wide range of devices, there is insufficient fidelity to conduct full design development. To do so, certain papers have tailored the procedure to a particular WEC, such that device-specific geometries can be optimized. Two papers that were identified that performed device optimization through the use of brute force techniques in generic sea-states [53] [54]. Durren [53] performed a brute-force experimental optimization of the wing geometry of a novel WEC design, the Aqua-fly. Mundon and Nair [54] performed a geometry optimization, conducted over multiple stages, on a novel magnetostrictive wave energy converter developed by Oscilla Power, Inc. The initial stage was conducted using a frequency domain representation of the converter, developed with the ORCAFLEX hydrodynamic code; within this model, the WEC generator was modelled with an equivalent stiffness. The second stage of the optimization studied the optimality of certain hydrodynamic parameters by means of experimental testing.

To improve the performance of the optimization algorithm in terms of specific device design, Goggins and Finnegan [55] incorporate site-specific data into the optimization procedure. They state that the inclusion of location-specific wave energy data is necessary for optimal device design, as alternative wave spectra will yield a WEC design that does not operate at resonance during predominant wave conditions in the deployment location; this will result in lower energy absorption [55]. Goggins and Finnegan [55] optimized the site-dependent external geometry of an axisymmetric point absorber WEC through the brute force assessment of a series of parameterized shapes as well as the PTO damping coefficient. The optimal geometry was determined using the significant velocity, which is a function of the device RAO, while the PTO damping coefficient was optimized using a linear hydrodynamic model with coefficients imported from ANSYS AQWA.

However, while site-specific sea-states are a marked improvement on optimizations based on a generic wave spectrum, brute force optimization requires expert knowledge of the domain [56]. Therefore many studies have instead progressed to the use of more complex optimization algorithms, such as evolutionary-based approaches [56] [57] [58] [59]. Making use of the gains in computational speed that are achieved with heuristic optimization algorithms, studies have implemented multi-objective fitness functions in order to capture some of the complex trade-offs in the WEC design process [57] [58]. These trade-offs are studied with a Pareto front, such as in the work by McCabe et. al [57]. McCabe et. al [57] used the genetic algorithm to conduct a multi-objective optimization on the shape of an arbitrarily defined point-absorber collector. The study was conducted in sea-states that were averaged over multiple sites across the UK; this was used in conjunction with a 2-DOF hydrodynamic model to maximize the power output of the WEC while minimizing the size and penalizing large velocities. Babarit and Clement [59] implemented a site-specific, dual layered optimization procedure for the study of the SEAREV converter; initially the genetic algorithm was used in order to optimize the external shape, followed by a gradient algorithm optimization for the determination of the optimal reactive mass within the body. The optimization function was a dual maximization of the absorbed power while minimizing the displacement, which was used as a cost function; trade-offs between these objectives were assessed by means of a Pareto front. The device hydrodynamics were modelled in the frequency domain, while the PTO was modelled as a linear damper.

To further increase the fidelity of the modelling procedure, many studies have incorporated more accurate PTO and mooring models into the optimization. In order to reduce computational expense in modelling a more complex WEC configuration, studies have found ways to approximate the objective function [30] [56]. One such approach is found in the work of Colby et. al [56], who optimized PTO parameters for a novel design developed by Columbia Power Technologies Inc. The device made use of ballast for real-time geometry control, which necessitated resolving the PTO within the optimization. The device was modelled in the time domain for a particular location, after which the data was used to develop a function approximation by means of neural networks; using the computational gains achieved with this functional approximator, the control loop timing and ballast configuration were optimized using an evolutionary algorithm. Ortiz [30] used a meta-model based optimization approach to optimize the mooring configuration of a self-reacting point absorber WEC. The meta-model based approach enabled the use of a full fidelity hydrodynamic model, created in nonlinear BEM solver ProteusDS, while still maintaining reasonable computational times.

Furthermore, studies have also looked at the incorporation of control into the optimization, to provide a more holistic approach to device design [56] [58] [60]. Kurniawan [58] performed a multi-objective optimization on the external geometry of an oscillating water column converter, using an evolutionary algorithm. The power of the device was maximized in conjunction with the minimization of the device surface area, which was used as a cost function. The hydrodynamic and PTO models are created with bond graph representations, with hydrodynamic coefficients inputted from WAMIT. This study had the highest fidelity PTO model seen in WEC geometry optimization literature, with the model including the piston, accumulator tanks, and check valves of the hydraulic system; in addition, the study also assessed the gains achieved with geometry control. Victor et. al [60] optimized the slope angle and crest freeboard of an overtopping WEC, in order to maximize the produced power. Empirical relationships were converted to analytical formulae for optimal geometries, in order to assess the performance of five different geometry control strategies in three different wave climates; these strategies covered both fixed and real-time varying device geometry. Incorporating control in the optimization process has been found to produce substantially different results, when compared to conventional control-independent optimization methods [61]. Gilloteaux and Ringwood [61] studied the influence of latching on the optimal draught and radius of a heaving buoy. When compared to optimization in the absence of control, they found that control-informed optimization led to a significantly different geometry, such that two different natural resonance periods resulted. The optimization was performed using the simplex algorithm, with a linear time domain hydrodynamic model, as well as a linear damper PTO force.

From the review of optimization techniques, it is clear that no universal approach to optimization exists. However, there are a variety of techniques presented in literature for improving the accuracy and applicability of the optimization procedure in terms of a particular device. In particular, it has been shown that location-specific data is necessary for accurately determining an optimal device geometry. Furthermore, it is possible to include high fidelity PTO models in the optimization process, if heuristic algorithms are used to intelligently search the design space [58]. Consequently, these improvements are carried forward to the development of the current optimization procedure. Despite these improvements, no methods have been identified that aim to optimize the geometry of the PTO in sufficient fidelity to apply the techniques directly to the AOE device. In particular, the complexities inherent to the AOE WEC prevent the use of function approximators such as meta-models or neural network based approaches. These methods are not believed to have sufficient fidelity to resolve the real-time thermodynamic changes seen in the AOE system. Furthermore, the cascaded nature of the AOE WEC prevents the implementation of control directly in the optimization procedure. This gap in literature prompted the generation of a novel optimization method for introducing passive force control.

3.2 Optimization Procedure

While in the ideal case, it would be possible to optimize the entire PTO geometry, the optimization procedure is limited by computational time. Therefore, several steps were undertaken to alleviate some of the computational requirements. Since the computational expense of the optimization scales rapidly with the number of design parameters, a limited number of parameters were selected. Furthermore, the optimization was conducted in two phases in order to improve the convergence rate of the genetic algorithm. The first stage of the optimization performed an unconstrained search on a large multi-dimensional search area. The function of this stage was to shrink the search area to a manageable size, within which the global optimum is ideally contained. Following the completion of this first stage, the search area was shrunk, and constraints were added in order to restrict the progression of the genetic algorithm to a more fruitful search area. These improvements in the algorithm allowed results to be obtained in a moderate timeframe, while still allowing the full fidelity AOE model to be used in the evaluation of the objective function for each set of design variables. The selection of appropriate design variables for the optimization procedure is discussed in the following section, followed by a detailed discussion on the selection of the optimization algorithm, associated objective function, and initial conditions.

3.2.1 Design Variables

The intelligent selection of ideal PTO parameters is critical for optimizing the PTO force of the AOE WEC, as well as improving the throughput of air. In particular, it is expected that the optimal PTO geometry incorporates the following characteristics:

1. Air is produced at a sufficient pressure to drive on-shore generator.
2. Air is produced steadily, with minimal interruptions as it passes through the cascade.
3. Optimal PTO forcing characteristics, to aid in power capture.

Many of these characteristics require trade-offs, which complicates the selection of an optimal set of parameters. There is a trade-off between the production of air at a sufficiently high pressure and the continual production of air. Secondly, there is a trade-off in the increase of the allowable mass flow rate (increase in valve diameters), and minimization of temperature losses (which would require a reduction in the exposed surface area). These trade-offs are expected to produce performance peaks in the design space. To properly explore these design peaks, focus was placed on parameters that not only have a direct impact on how well the desired characteristics are met, but are also incorporated in the trade-offs between these characteristics. This selection procedure limits the optimization to only the most pertinent set of parameters. The set of parameters chosen for the optimization is summarized in Table 3.1. Parameters that were not selected are the dimensions of the tank, for which $\boldsymbol{V_{tank}} =$ 8.82 m^3, and $\boldsymbol{a_{tank}} = 62.57$ m^2, as well as the length of the pipe, which was 70 m.

Table 3.1: Design variables in the optimization procedure, and variable limits.

Variable	**Lower Limit**	**Upper Limit**	**# Variables**
Cylinder Diameter, Devices 1 - 3	1 m	3 m	3
Cylinder Length, Devices 1 - 3	2 m	4.5 m	3
Orifice Ratio, Devices 1 - 3	0.05	0.5	1
Regulated Pressure, Device 3	6 bar	15 bar	1
		Total	**8**

The cylinder diameter and length were selected due to the substantial impact that the cylinder dimensions have on both the magnitude and continuity of air production, as well as the impact on PTO force scaling. The regulated pressure is the pressure at which air is sent to shore, which in turn will impact the pressure within each of the devices; similar to the cylinder dimensions, this has a nonlinear impact on the continuity of air throughput as well as the PTO force. Lastly, the orifice ratio is the calculated as the orifice diameter divided by the cylinder diameter. This ratio determines the maximum flow rate through the valves, as well as the pipe diameter (since the pipe and orifice diameters are the same). While the orifice diameter will scale with each device, since the cylinder diameter will change, all valves within a particular device have the same diameter.

The limits on each of these parameters is also summarized in Table 3.1; within these limits, the optimization may select values for the design variables on a continuum. These limits apply to the first stage of the optimization, after which more restrictive bounds were placed; the development of these new variable limits is described in Section 4.1.1. For the initial optimization stage, the upper limits on the cylinder diameter and length were determined as conservative estimates of expected manufacturing limits following discussions with AOE Accumulated Ocean Energy Inc. These limits were not restricted by the external geometry of the spar, as if significant performance benefits were found through the optimization, there may have been a possibility of altering the external geometry to fit a larger piston design. This is seen with the piston diameter limit of 3 m, which exceeds the column diameter of 2.74 m listed in Table 1.2. The lower limit of the regulated pressure corresponded to the minimum design pressure of available off-the-shelf air turbines, of which a comprehensive listing of manufacturer data is listed in Table 2.3. The remaining limits were selected to ensure that variable selection would not be restricted. Within the bands placed on each of the variables, the parameter values were selected according to the optimization algorithm discussed in the following section. Given the nonlinear nature of the relationships between the variables, the variables were not assessed independently; instead, the objective of the optimization is to assess and ultimately select a set of eight variables, which is collectively referred to as the optimal design.

3.2.2 Optimization Algorithm

Given the highly nonlinear nature of the optimization function, it is not possible to define a strictly convex objective function; rather, it is likely that the problem is highly non-convex, such it is not possible to guarantee the identification of a global optimum. As a result, rather than using deterministic algorithms it is necessary to make use of probabilistic algorithms, which use heuristics to identify the processing order of the candidate solutions [62]. A variety of probabilistic algorithms exist, such as stochastic methods, evolutionary algorithms, or swarm intelligence, for which a classification is provided by Weise [62]. For the current work, the genetic algorithm was selected, based on its capacity to search a large multi-variable space with relatively fast computational times. Furthermore, the algorithm, through the use of crossover and mutation functions, incorporates methods to avoid getting stuck in a local minimum. In addition, the use of this algorithm has precedent in wave energy literature, and provides a proven method of intelligently searching the design space [57] [59].

The genetic algorithm is based off genetics and evolutionary principles [63], in which desirable combinations of design variables are carried forward to future generations, and mutated in order to introduce the potential for random positive change. The genetic algorithm optimization procedure is detailed below [63]:

1. A group of candidate solutions is selected as an initial starting point (referred to as a population).
2. The optimality of the candidate solutions is assessed using a fitness function (referred to as the objective function).
3. A certain number of strong candidate solutions are carried forward to the next generation of the optimization.
4. In addition to the carried-over candidate solutions, new candidate solutions are produced by:

    a. Mutating existing solutions (producing entirely new candidates).
    b. Crossing over characteristics of existing solutions
5. The new candidate solutions are re-assessed using the fitness function, and the process is repeated.

For the current study, the genetic algorithm procedure is implemented using MATLAB's prebuilt *"ga"* function. In the first stage of the optimization, the generation size was limited to 60 candidate designs, which increases the frequency with which candidate mutation and crossover occur; in turn, this increases the speed of progression towards an optimal design. Following the completion of the first optimization procedure, the generation size was expanded to 90 candidate designs, in order to reduce the likelihood of encountering a local minimum within the reduced search area.

Objective Function

The objective of the optimization is to maximize the expected annual average power output from the device, such that for each candidate design, a single value for the objective function was determined. Since the optimal design is highly dependent on the wave climate in which the WEC is placed, representative sea-states for a potential deployment location were used in the optimization procedure. The deployment location was taken to be Amphitrite Bank, off the west coast of Vancouver Island, Canada, which was selected as its energetic wave climate and near-shore placement facilitate the passing of compressed air to shore. Furthermore, the Amphitrite Bank location is in close proximity to coastal communities as well as the AOE Accumulated Ocean Energy Inc. headquarters in Victoria. A wave histogram for this location was created by Robertson et al [33] from wave buoy data obtained by the West Coast Wave Initiative; to do so, directional wave data was gathered with hourly resolution for the 2013 calendar year. Existing WCWI wave buoy locations in relation to Vancouver Island are provided in Fig. 3.1.

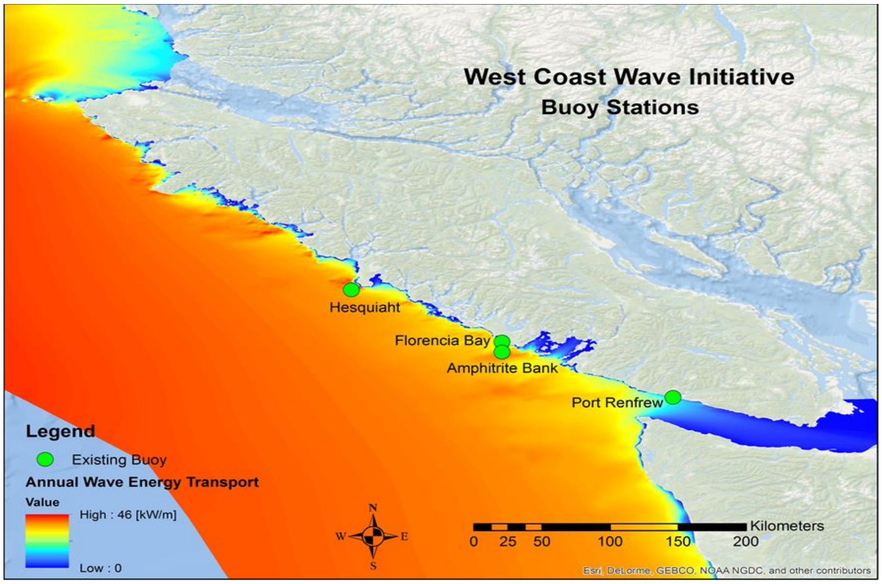

Figure 3.1: West Coast Wave Initiative wave buoy locations.

Wave histograms of significant wave height and wave energy period for the Amphitrite Bank location, indicating the annual distribution of occurrence, as well as the annual wave energy flux of each sea-state are given in Fig. 3.2 and Fig. 3.3.

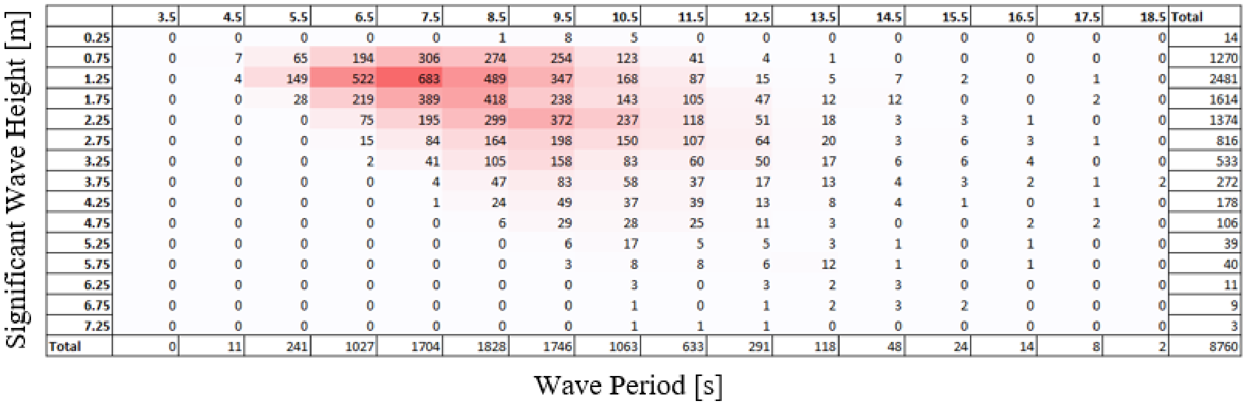

	3.5	4.5	5.5	6.5	7.5	8.5	9.5	10.5	11.5	12.5	13.5	14.5	15.5	16.5	17.5	18.5	Total
0.25	0	0	0	0	0	1	8	5	0	0	0	0	0	0	0	0	14
0.75	0	7	65	194	306	274	254	123	41	4	1	0	0	0	0	0	1270
1.25	0	4	149	522	683	489	347	168	87	15	5	7	2	0	1	0	2481
1.75	0	0	28	219	389	418	238	143	105	47	12	12	0	0	2	0	1614
2.25	0	0	0	75	195	299	372	237	118	51	18	3	3	1	0	0	1374
2.75	0	0	0	15	84	164	198	150	107	64	20	3	6	3	1	0	816
3.25	0	0	0	2	41	105	158	83	60	50	17	6	6	4	0	0	533
3.75	0	0	0	0	4	47	83	58	37	17	13	4	3	2	1	2	272
4.25	0	0	0	0	1	24	49	37	39	13	8	4	1	0	1	0	178
4.75	0	0	0	0	0	6	29	28	25	11	3	0	0	2	2	0	106
5.25	0	0	0	0	0	0	6	17	5	5	3	1	0	1	0	0	39
5.75	0	0	0	0	0	0	3	8	8	6	12	1	0	1	0	0	40
6.25	0	0	0	0	0	0	0	3	0	3	2	3	0	0	0	0	11
6.75	0	0	0	0	0	0	0	1	0	1	2	3	2	0	0	0	9
7.25	0	0	0	0	0	0	0	1	1	1	0	0	0	0	0	0	3
Total	0	11	241	1027	1704	1828	1746	1063	633	291	118	48	24	14	8	2	8760

Figure 3.2: Frequency of sea-state occurrence [# Hours/Year] for Amphitrite Bank, as defined by significant wave height [m] and wave energy period [s].

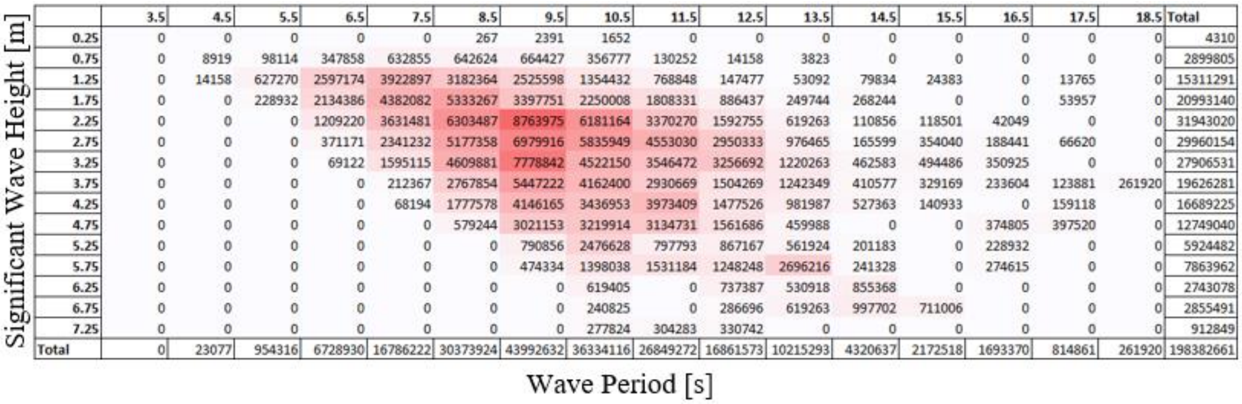

	3.5	4.5	5.5	6.5	7.5	8.5	9.5	10.5	11.5	12.5	13.5	14.5	15.5	16.5	17.5	18.5	Total
0.25	0	0	0	0	0	267	2391	1652	0	0	0	0	0	0	0	0	4310
0.75	0	8919	98114	347858	632855	642624	664427	356777	130252	14158	3823	0	0	0	0	0	2899805
1.25	0	14158	627270	2597174	3922897	3182364	2525598	1354432	768848	147477	53092	79834	24383	0	13765	0	15311291
1.75	0	0	228932	2134386	4382082	5333267	3397751	2250008	1808331	886437	249744	268244	0	0	53957	0	20993140
2.25	0	0	0	1209220	3631481	6303487	8763975	6181164	3370270	1592755	619263	110856	118501	42049	0	0	31943020
2.75	0	0	0	371171	2341232	5177358	6979916	5835949	4553030	2950333	976465	165599	354040	188441	66620	0	29960154
3.25	0	0	0	69122	1595115	4609881	7778842	4522150	3546472	3256692	1220263	462583	494486	350925	0	0	27906531
3.75	0	0	0	0	212367	2767854	5447222	4162400	2930669	1504269	1242349	410577	329169	233604	123881	261920	19626281
4.25	0	0	0	0	68194	1777578	4146165	3436953	3973409	1477526	981987	527363	140933	0	159118	0	16689225
4.75	0	0	0	0	0	579244	3021153	3219914	3134731	1561686	459988	0	0	374805	397520	0	12749040
5.25	0	0	0	0	0	0	790856	2476628	797793	867167	561924	201183	0	228932	0	0	5924482
5.75	0	0	0	0	0	0	474334	1398038	1531184	1248248	2696216	241328	0	274615	0	0	7863962
6.25	0	0	0	0	0	0	0	619405	0	737387	530918	855368	0	0	0	0	2743078
6.75	0	0	0	0	0	0	0	240825	0	286696	619263	997702	711006	0	0	0	2855491
7.25	0	0	0	0	0	0	0	277824	304283	330742	0	0	0	0	0	0	912849
Total	0	23077	954316	6728930	16786222	30373924	43992632	36334116	26849272	16861573	10215293	4320637	2172518	1693370	814861	261920	198382661

Figure 3.3: Annual wave energy flux [J / m] for Amphitrite Bank, as defined by significant wave height [m] and wave energy period [s].

The frequency of occurrence is calculated as the number of hours throughout the year that the wave data falls into a particular bin, while the annual energy from wave energy flux (wave power incident per metre) is calculated using Eq. 3.1 [55].

$$E_{flux} = \frac{\rho g^2}{64\pi} T_e H_s^2 \ \cong 490 N_{hours} T_e H_s^2 \qquad (3.1)$$

Where N_{hours} is the number of hours per year in which a particular sea-state occurred, as seen in Fig. 3.2. While in the ideal case, it would be possible to provide an annual estimate based on the entire histogram of wave data, the computational expense is unfeasible. Instead, the annual power estimate for each candidate design was calculated as a weighted average of the device performance in six different sea-states. These six sea-states were selected in order to provide a holistic representation of the entire wave histogram. To do so, the wave histogram was grouped into sections, from which a single sea-state was chosen for the analysis. Each section was partitioned so that its contents have similar wave characteristics, while incorporating knowledge of the frequency of occurrence. This data was included so that areas of the histogram with a higher frequency of occurrence would be divided with a better resolution. In particular, the divisions were made so that a weighted average of the annual frequency of occurrence and the wave energy flux was approximately constant, as seen in Eq. 3.2.

$$0.2\frac{\sum_{i=1}^{M} N_i}{N_{Total}} + \quad 0.8\frac{\sum_{i=1}^{M} E_{flux_i}}{E_{Total}} \cong Constant \tag{3.2}$$

Where M is the number of sea-states within each section, and N_{Total} and P_{Total} are the number of hours per year (8760 Hours) and annual wave energy flux (198.4 MJ/m), respectively. These values are included in Fig. 3.2 and Fig. 3.3. The distribution of the wave power transport was weighted higher in the calculation, as it is a stronger metric for similarity in sea-state conditions. The resulting divisions are shown in Fig. 3.4, with a summary of the weight averages presented in Table 3.2.

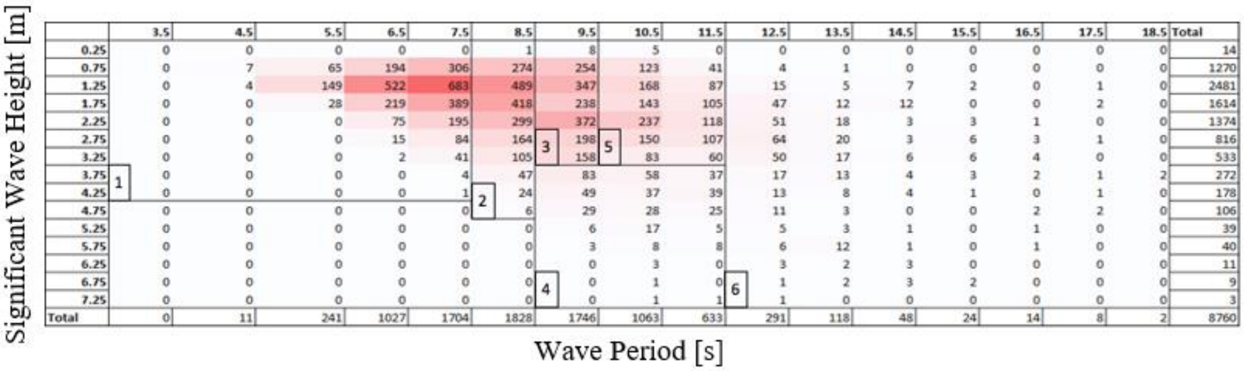

	3.5	4.5	5.5	6.5	7.5	8.5	9.5	10.5	11.5	12.5	13.5	14.5	15.5	16.5	17.5	18.5	Total
0.25	0	0	0	0	0	1	8	5	0	0	0	0	0	0	0	0	14
0.75	0	7	65	194	306	274	254	123	41	4	1	0	0	0	0	0	1270
1.25	0	4	149	522	683	489	347	168	87	15	5	7	2	0	1	0	2481
1.75	0	0	28	219	389	418	238	143	105	47	12	12	0	0	2	0	1614
2.25	0	0	0	75	195	299	372	237	118	51	18	3	3	1	0	0	1374
2.75	0	0	0	15	84	164	198	150	107	64	20	3	6	3	1	0	816
3.25	0	0	0	2	41	105	158	83	60	50	17	6	6	4	0	0	533
3.75	0	0	0	0	4	47	83	58	37	17	13	4	3	2	1	2	272
4.25	0	0	0	0	1	24	49	37	39	13	8	4	1	0	1	0	178
4.75	0	0	0	0	0	6	29	28	25	11	3	0	0	2	2	0	106
5.25	0	0	0	0	0	0	6	17	5	5	3	1	0	1	0	0	39
5.75	0	0	0	0	0	0	3	8	8	6	12	1	0	1	0	0	40
6.25	0	0	0	0	0	0	0	3	0	3	2	3	0	0	0	0	11
6.75	0	0	0	0	0	0	0	1	0	1	2	3	2	0	0	0	9
7.25	0	0	0	0	0	0	0	1	1	1	0	0	0	0	0	0	3
Total	0	11	241	1027	1704	1828	1746	1063	633	291	118	48	24	14	8	2	8760

Figure 3.4: Division of wave histogram for optimization procedure.

Table 3.2: Weighted average calculation for division of wave histogram.

Section	**Ratio of Total Wave Energy Flux**	**Ratio of Total Hours**	**Weighted Average**
1	0.1235	0.3407	0.1669
2	0.1531	0.2086	0.1642
3	0.1518	0.1799	0.1574
4	0.2136	0.0501	0.1809
5	0.1748	0.1630	0.1725
6	0.1832	0.0577	0.1581

Within each of these sections, a weighted average of the encompassing sea-states was taken, based on the number of hours of occurrence. This was used to compute the average significant wave height and energy period within the section, using, as seen in Eq. 3.3 and 3.4.

$$\overline{H_s} = \frac{\sum_{i=1}^{M} H_{s,i}\, N_i}{\sum_{i=1}^{M} H_{s,i}} \tag{3.3}$$

$$\overline{T_e} = \frac{\sum_{i=1}^{M} T_{e,i}\, N_i}{\sum_{i=1}^{M} T_{e,i}} \tag{3.4}$$

The sea-state that was closest to the average was selected as the representative of that section for the optimization procedure. It is important to note that while weighting based on hours does not provide the strongest representation of the section in terms of energy similarity (for which the wave power transport would be used to weight the sea-states), it ensures that the optimization will tend to focus on sea-states with a high probability of occurrence. This will in turn promote the continuity of power output throughout the year. For the purpose of the optimization procedure, the probability of occurrence of each sea-state corresponds to the probability of a wave condition falling within its parent section. The summary of the selected sea-states, as well as that section's probability of occurrence throughout the year, is given in Table 3.3.

Table 3.3: Selected sea-states for optimization procedure.

#	**Significant Wave Height (H_s) [m]**	**Wave Energy Period (T_e) [s]**	**Probability of Occurrence [%]**
1	1.25	6.5	34.07
2	1.75	8.5	20.86
3	1.75	9.5	17.99
4	2.25	10.5	16.30
5	3.25	13.5	5.77
6	4.25	10.5	5.01

To reproduce a realistic wave spectrum using these wave parameters, the simulations are run using a Pierson-Moskowitz spectrum. To do so, the spectrum was discretized into 140 wave segments, which were manually inputted into ProteusDS. These wave segments included directional spreading and random phase offset in order to more closely approximate realistic sea-states.

With these six representative wave conditions determined, an estimate of the annual power production was computed as the sum of the average power produced in each sea-state, weighted by the sea-state's probability of occurrence. This is the objective function of the optimization, and is summarized in Eq. 3.5.

$$Obj. = \sum_{Sea\ State=1}^{6} Power_i\ Probability_i \tag{3.5}$$

The power is computed as a function of flow exergy, for which motivation is provided in Section 2.6. The flow exergy is then converted to average outputted power as a function of the flow exergy at a given time step, e_t, and the mass-flow rate at the outlet of the third device in the WEC chain.

$$Power = \frac{\sum_{t=1}^{t_{total}} \dot{m}_t e_t}{t_{total}} \tag{3.6}$$

Where t_{total} is the time period over which the available power is averaged. A description of how this time period was determined, including the set of initial conditions used in each simulation, is described in the following section.

Initial Conditions

In order to reduce the impact of start-up effects on the calculation of the objective function, the average outputted power is not determined from the start of the simulation. Rather, several checks are put in place to ensure the system is as close to steady-state as possible for the duration of the simulation, while not significantly increasing the computation time. In developing these checks, it is understood that the PTO state is a function of both the sea-state and PTO geometry. Since a particular PTO geometry is held for the simulation of six different sea-states, two checks are used to adjust the thermodynamic state of air as a function of the set of chosen parameters. These initial conditions are then carried forward for the six different simulations, each of which use a final check to ensure the system is near steady-state prior to the calculation of the objective function. These checks are summarized as follows:

1. A 20 min simulation was run for a random set of seven sea-states, each with randomly selected input variables. This data was used to identify trends in the state variables (at steady state) as a function of the regulated pressure, which allowed an intelligent selection of initial parameters, included expected temperatures and pressures for each of the components.
2. Using these initial conditions, a 5-minute simulation was run using a moderate sea-state (H_s = 2.25m and T_e = 10.5s). This simulation was designed to smooth out variation in thermodynamic properties from changes in the PTO geometry. This thermodynamic state data is then carried forward as the initial condition for each of the six simulations.
3. A 2-minute simulation was conducted in each sea-state, to allow for the geometry-adjusted state to adapt to the current wave conditions.

Following these checks, the average power is then determined over a five-minute simulation.

3.3 Summary of Passive Control Problem Formulation

The formulation of the passive control problem is viewed as the optimal selection of critical PTO geometries for the maximization of power output in the Amphitrite Bank deployment location. In practice, this reduces to an optimization algorithm, for which key parameters are summarized below:

1. Algorithm – Genetic algorithm, conducted over two stages using MATLAB’s “*ga”* function.
2. Objective Function - Highest annual power output, determined using flow exergy and calculated as a function of 6 representative sea-states in the Amphitrite Bank location.
3. Variables – diameters and lengths of all three piston chambers, orifice ratio, and crack pressure.

Using this optimization procedure, it is expected that significant gains in power production at the Amphitrite Bank location can be achieved. Furthermore, the developed methodology provides a framework for implementing passive control in alternate WEC geometries. In doing so, a detailed procedure is provided for the selection of representative sea-states for a potential deployment location, which reflects the sensitivity of control implementation to the wave climate in which the WEC is placed.

Chapter 4. Passive Control: Implementation and Results

The formulation of the passive control problem developed in Chapter 3 provides a method of increasing the power output of the AOE WEC through the optimal selection of eight critical design variables. In this chapter, the results of the optimization procedure are presented, and an optimal design is selected. This is followed by a discussion on the effect of the optimization procedure on the power quality and end-stop collision rate of the WEC. While these additional considerations were not included in the objective function, they are important markers for the feasibility of grid integration and device survivability; both are critical for eventual WEC deployment. Lastly, the optimal design is carried forward to the development of a power matrix for the AOE WEC in the Amphitrite Bank location. This power matrix is critical for producing a baseline power production estimate against which the performance of the actively controlled design can be measured.

4.1 Optimization Results

Due to the high computational requirements of evaluating the objective function, the optimization was conducted using a distributed computed center provided by Ocean Networks Canada, for which the computations were completed over a three-month period on 17 machines. This set-up incorporated a managing ‘boss’ machine, as well as 16 ‘worker’ machines, which used a batch set-up to fully utilize the available CPU power on each machine. The optimization procedure was conducted for a total of 15 generations, spread over both stages of the optimization. Including both optimization stages, a total of 942 unique variable combinations were studied.

4.1.1 Results from First Stage of Optimization

In order to reduce the number of generations needed for convergence to an optimal solution, the initial set of parameters was selected intelligently as a combination of potential candidate solutions and random sets of variables; this was intended to provide a warm start to the optimization, while not prematurely limiting the search to a given area. Including this initial, user-defined, generation, the first stage of the optimization lasted seven generations. The progression of the objective function realized within each generation is shown in Fig. 4.1. The peak value of the objective function within each generation is shown in Table 4.1.

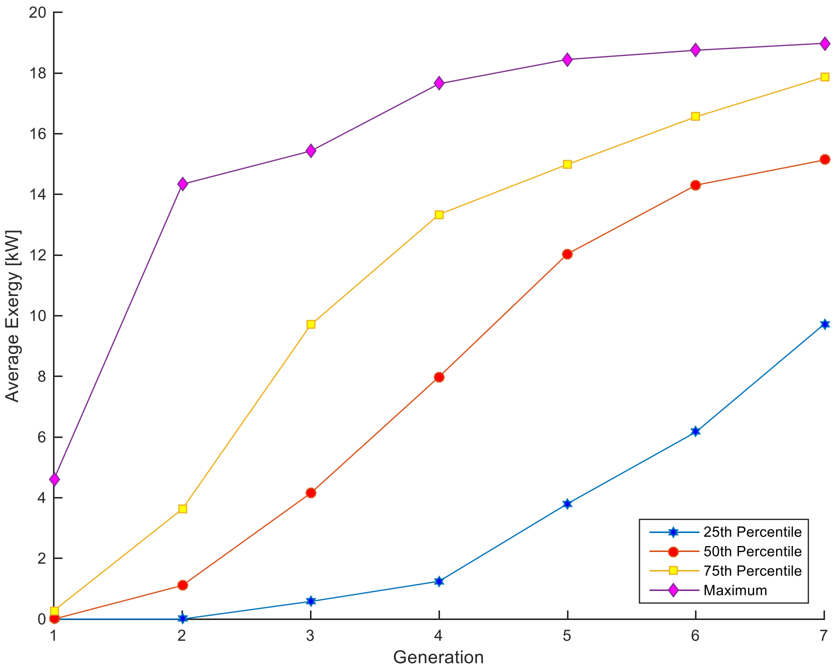

Figure 4.1: Progression of objective function within each generation.

Table 4.1: Progression of objective function in first stage of optimization.

Generation	Obj. Function [kW]	Increase from Previous Gen. [%]
1	4.607	~
2	14.34	211.16
3	15.43	7.63
4	17.65	14.38
5	18.45	4.54
6	18.75	1.65
7	18.98	1.22

As the optimization progressed, the gains achieved with each subsequent generation were progressively smaller. Further, the range of values within each generation decreases, which shows that there is progression to peaks within the design space. While there is not yet a basis for stating the algorithm has converged, the function of the first stage of the optimization was merely to shrink the initial search area to a manageable size; within this reduced parameter space it is likely that the global optimum is located. To identify areas in which the breadth of the design space can be reduced, the variation in each of the parameters as a function of the objective function is shown in Fig. 4.2.

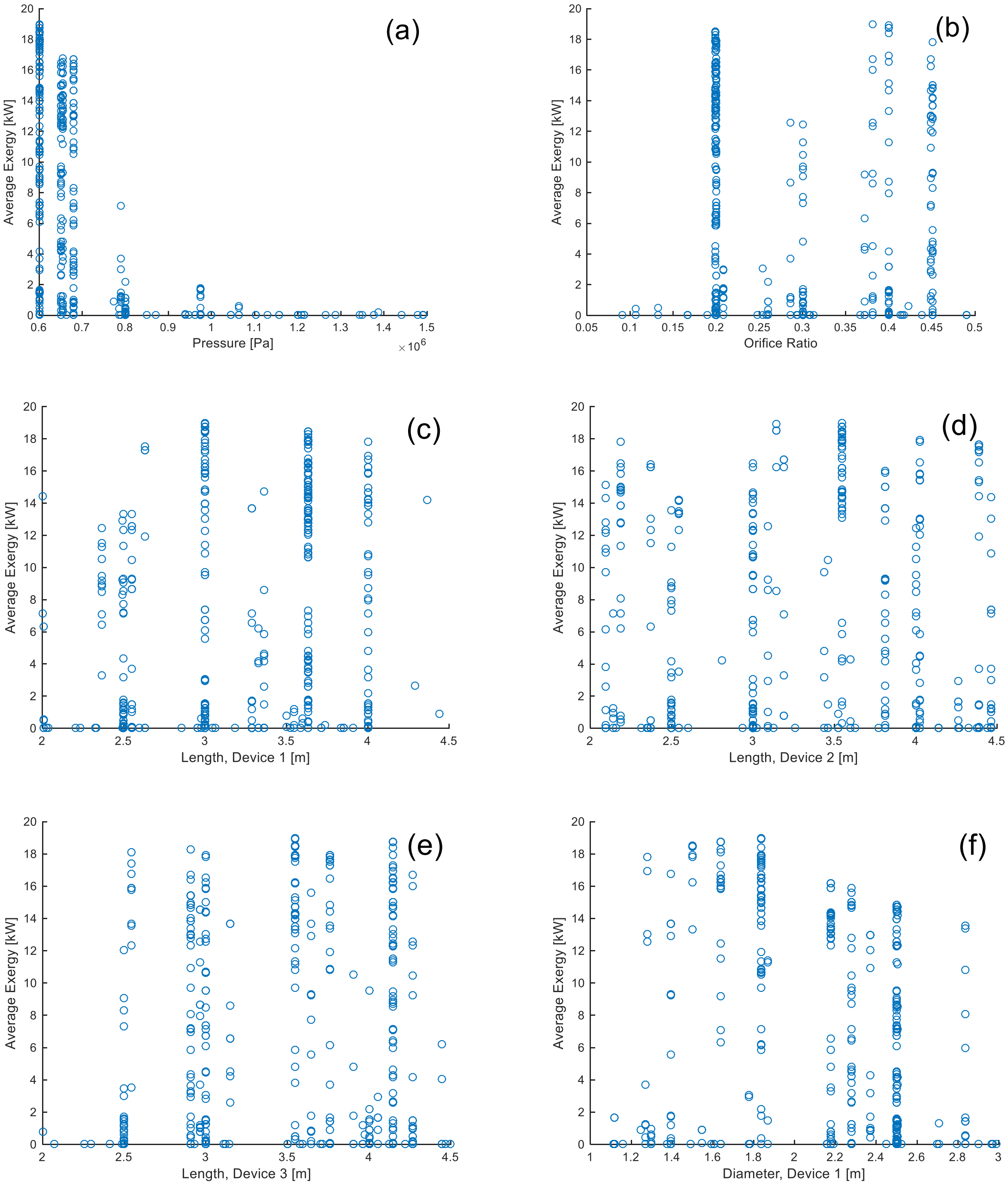

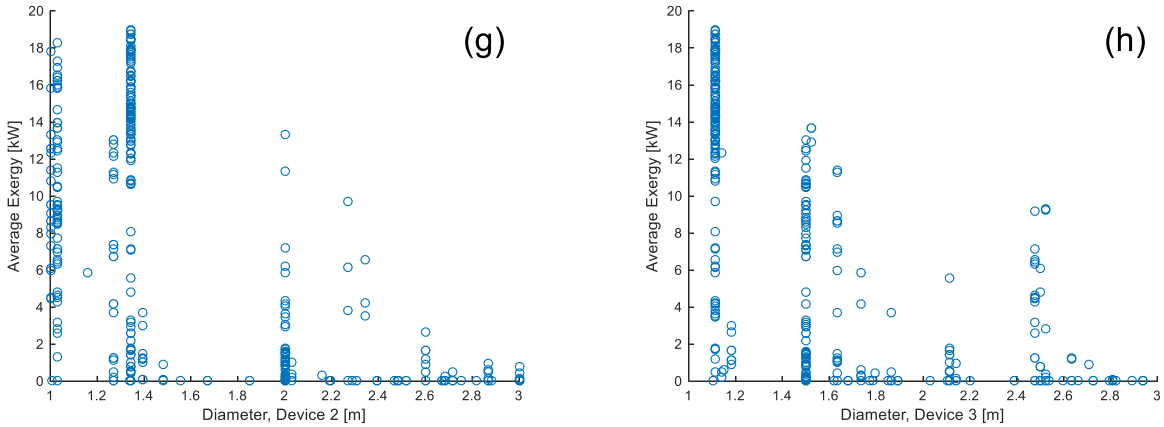

Figure 4.2: Exergy as a function of each of the design variables for the first stage of the optimization.

While it is clear that an exhaustive search of the entire search area has not yet been conducted, several trends are apparent. In particular, as seen in Fig. 4.2a it is clear that the outlet pressure has a strong negative correlation with the objective function, such that the optimal outlet pressure corresponds with the lower bound of air turbine manufacturing pressure limits. This trend is most likely caused by the fact that slight increases in pressure, while marginally increasing the exergy per unit volume of outlet flow, could potentially place severe limitations on the frequency with which mass-flow events are triggered. As a result, the frequency of occurrence of mass-flow events appears to be the limiting factor in determining optimal exergy scenarios. Consequently, while there is not yet sufficient data to select 6 bar as the optimal pressure, the search area can be reduced to below 9 bar. This allows the higher pressure 6.8 bar local optimum to be included the second stage of the optimization.

All other variable limits contain the current optimal value well within the optimization bounds, which is an indication that variable bounds were selected with enough breadth to contain the optimal value. However, none of the geometry variables are sufficiently correlated to the objective function to shrink the bounds of the second stage of the optimization. Instead, the relationship between the diameters and lengths were assessed, with the ratio between each of the diameters and lengths being shown in Fig. 4.3. Unity is indicated in red as a comparative measure for further discussion.

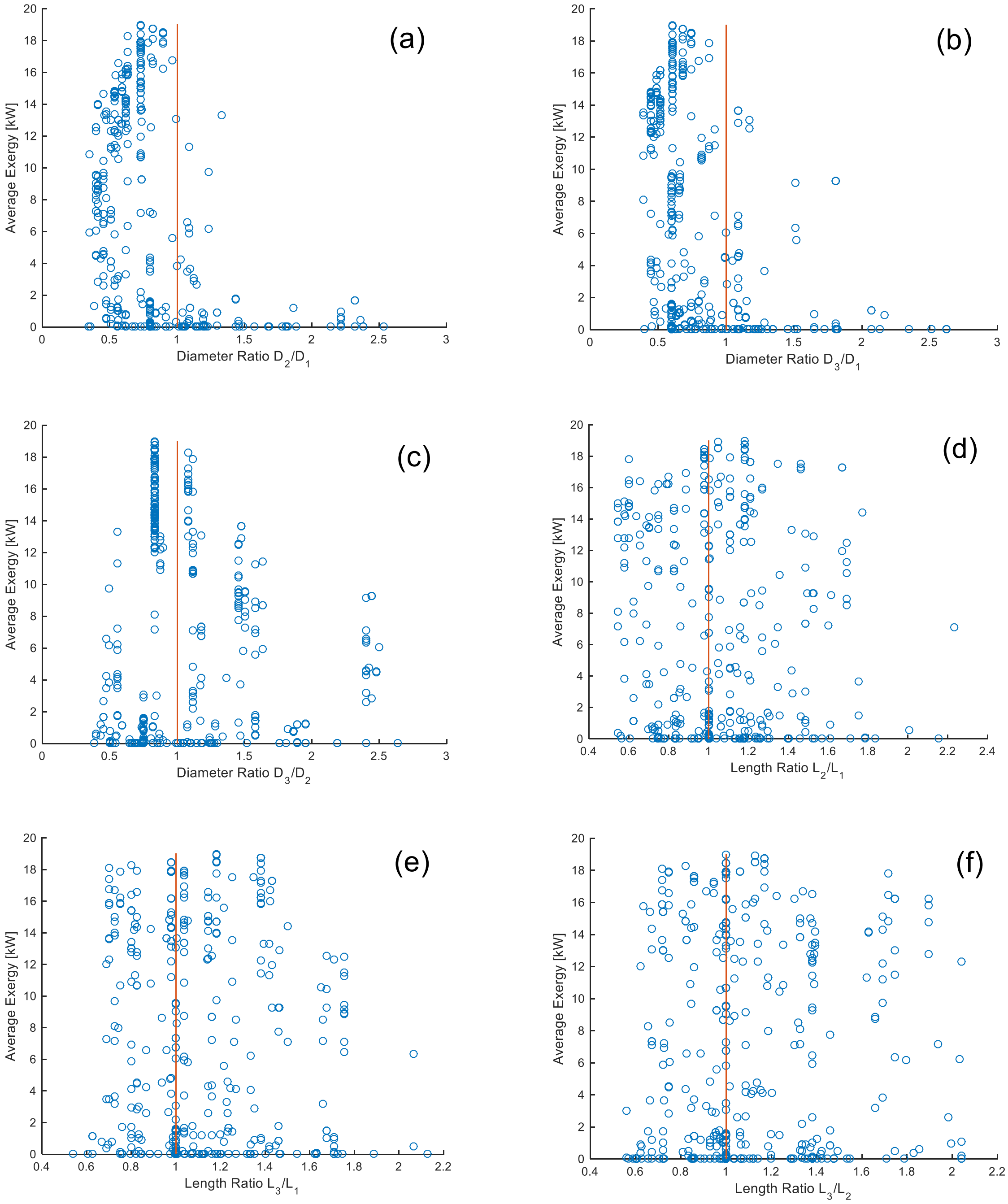

Figure 4.3: Diameter and length ratios between different devices for the first stage of the optimization.

Several trends are apparent from the plots of the diameter ratios. In particular, in all of the near-optimal scenarios $\frac{D_2}{D_1} < 1$ and $\frac{D_3}{D_1} < 1$. This makes sense, as the volume of piston chamber must continually decrease in order to maintain the pressure of the compressed air as it is passed between devices. Therefore, it is somewhat surprising that the diameter ratio from the second to third device does not need to be below unity. A potential explanation for this phenomena is that there is a penalty in shrinking the volume in the third device. In particular, while shrinking the third piston volume would allow for higher pressures to be maintained during air transfer from the second to third devices, this is only applicable in lower energy sea-states. For more energetic sea-states, in which the final crack pressure is easily achieved, the mass flow rate will decrease if the volume in the third device is shrunk. Therefore, the algorithm may have discovered a local optimum in which the volume is maintained at a high level in order to maximize production in high energy sea-states, while sacrificing output from lower energy seas. This is not expected to be a global optimum, in which it is likely that exergy production will be produced across the entire wave spectrum, but this possibility means there is not yet sufficient data to constrain the diameter of the third device relative to the second.

As seen by the scattered distribution of exergy among available length ratios, there is not a strong increase/decrease in the length of the latter devices. This is expected, as while there is a necessary decrease in volume between devices in order to maintain pressure, doing so with a decrease in diameter does not incur a penalty; conversely, decreases in the piston length may lead to losses in efficiency through an increased frequency of end-stop collisions. With this in mind, it can be further stated that the length among devices should be largely constant. Since the wave condition experienced by all devices is the same, and the diameter is smaller in latter, higher pressure devices, it is expected that the motion of the piston is largely constant, which would lead to similar piston lengths in each of the devices.

Given the identified trends in each of the eight variables, several additional constraints were placed in order to shrink the search area of the second stage of the optimization. These constraints are summarized in Table 4.2.

Table 4.2: Revised set of constraints for second stage of optimization.

	Stage 1		**Stage 2**		
Variable	Lower Limit	Upper Limit	Lower Limit	Upper Limit	Linear Constraints
D_1 –D_3	1 m	3 m	1 m	3 m	$\boldsymbol{D1 \geq D2}$ $\boldsymbol{D1 \geq D3}$
L_1 – L_3	2 m	4.5 m	2 m	4.5 m	-
OR	0.05	0.5	0.05	0.5	-
Pres.	6 bar	15 bar	6 bar	**9 bar**	-

Using this revised search area, the second stage of the optimization was conducted.

4.1.2 Results from Second Stage of Optimization

In addition to changes in the search area, the second stage of the optimization also uses a larger generation size of 90 sets of variables. This increase reduces the likelihood of the optimization getting stuck on a local minimum, by expanding the breadth with which the search area is studied. However, since the generation size is increased, it is not possible to merely use the latest generation as the starting point of the second stage. Instead, in order to ensure that the best combinations of variables were carried forward to the second stage of the optimization, the best 90 unique sets of variables from the first stage were gathered. Eight cases were identified that had strong similarities, and were subsequently replaced with eight high pressure cases in which the pressure was over 7 bar. This was used to maintain variation in the starting generation. With this set of starting parameters, the second stage of the optimization was run for eight generations, not including the initial starting generation (which did not introduce any new data). The progression of the objective function realized within each generation is shown in Fig. 4.4. The peak value of the objective function within each generation is shown in Table 4.3. Both stages of the optimization are included in order to show the complete progression of the objective function.

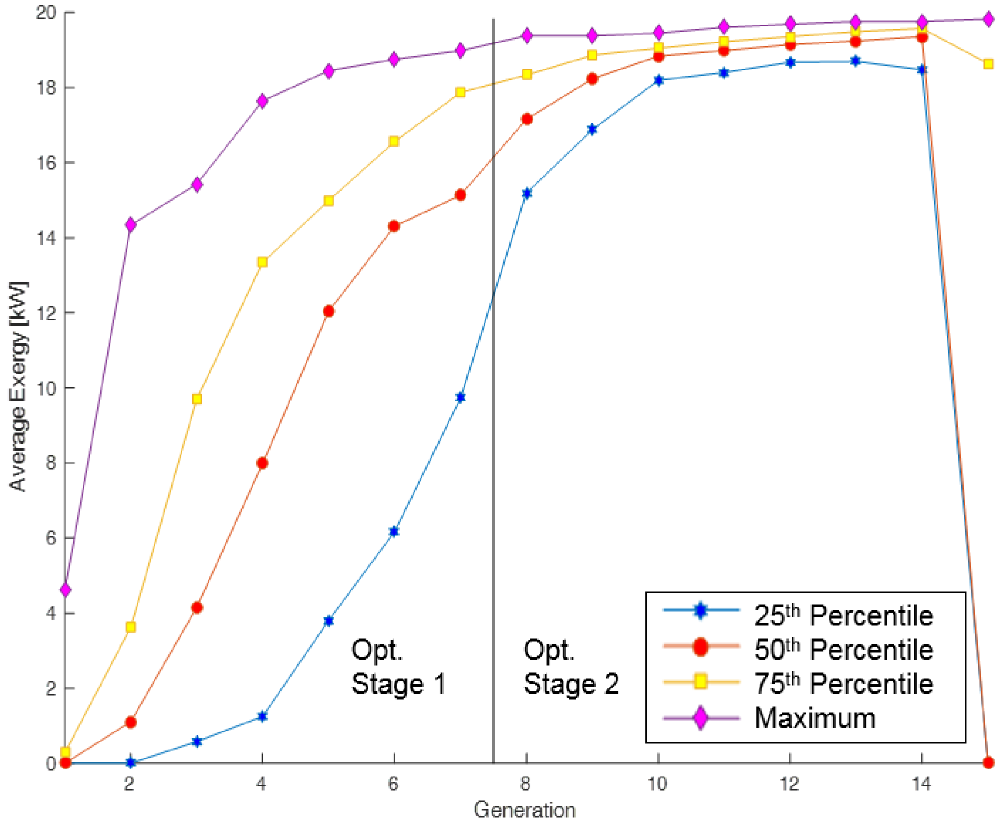

Figure 4.4: Progression of objective function within both stages of optimization.

Table 4.3: Progression of objective function in both stages of optimization.

Generation	Obj. Function [kW]	Increase from Previous Gen. [%]
7	18.98	Total Increase in Stage 1: 311.98
8	19.38	2.12
9	19.38	0.00
10	19.45	0.34
11	19.61	0.81
12	19.69	0.41
13	19.76	0.37
14	19.76	0.00
15	19.83	0.33

From generation 1 to 15, there is a net increase of 330.35% in the objective function, which shows the large value in performing the optimization procedure. This gain was achieved after 14 complete generations, after which the optimization was halted. While it is impossible to state if a global optimum has been reached when using the genetic algorithm, there are several indications of convergence in the present study.

For one, in later generations there are progressively smaller increases in the objective function; this can clearly be seen in Table 4.3. As a result, while the first stage of the optimization led to a 311.98% increase in the objective function, the entire second stage of the optimization only produced an 18.37% increase. The decrease in the rate at which gains are achieved is a strong indication of convergence towards a particular set of design parameters. This is further corroborated by the fact that aside from the last generation, which was stopped mid-simulation and hence is incomplete, there is a decrease in the range. In particular, within each generation there is an increase in the objective function at the 25th, 50th, and 75th percentiles, which is a further indication that there is convergence towards a particular set of design parameters. These design parameters may constitute a single peak in the design space, or a group of different peaks that have a similar value for the objective function.

With these factors in mind, it was concluded that the optimization algorithm has sufficiently converged to the point at which results can be extracted. While it is unlikely that a global optimum has been found, the best set of design variables produced by the optimization (reached in the 15th generation) is referred to as the best estimate for the global optimum. This estimate of the globally optimum set of design parameters is listed in Table 4.4.

Table 4.4: Best estimate of globally optimum set of design variables.

Design Variable	**Value**	**Design Variable**	**Value**
Diameter, Device 1	1.6298 m	**Length, Device 1**	3.3400 m
Diameter, Device 2	1.2938 m	**Length, Device 2**	3.5440 m
Diameter, Device 3	1.1167 m	**Length, Device 3**	3.1185 m
Orifice Ratio	0.3744	**Crack Pressure**	600.75 kPa

While the optimal design is not likely known to 5 significant figures, these values were fully reported to maintain the unique nature of the optimal solution. For example, a significant number of designs incorporate a crack pressure between 600.00 and 600.75 kPa, for which a slight distinction was made during the optimization process. In order to demonstrate the scope of the complete set of studied cases, the variation in each of the parameters as a function of the objective function is shown in Fig. 4.5.

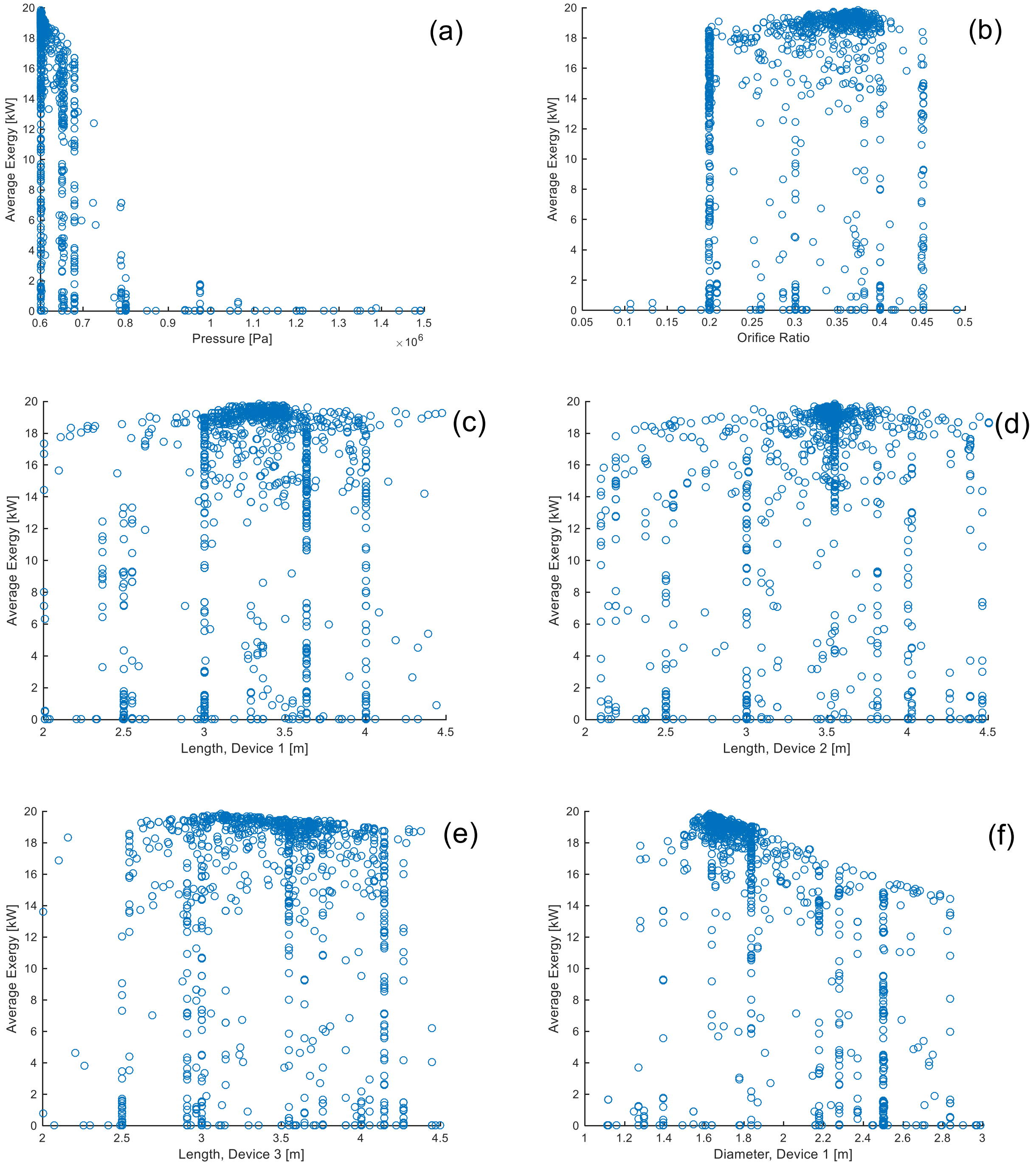

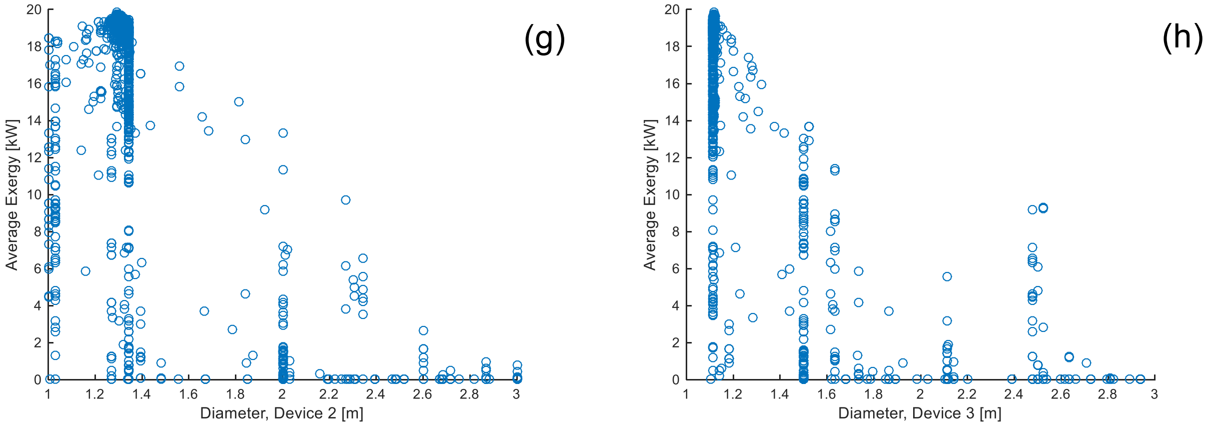

Figure 4.5: Exergy as a function of each of the design variables for both stages of the optimization.

It is apparent that there is strong clustering within the design space on two levels, vertically and in bunches (typically around the optimal point). While not done intentionally, vertical clusters form as a result of the algorithm varying combinations of the remaining seven variables while holding a particular value constant. Conversely, intensive study of the area around the optimal value is done intentionally through the use of mutation and design crossover; this ensures the algorithm progresses in the ideal direction from the current optimal, when considering the 8-variable design space. Unfortunately, these groupings prevent the entire design space from being exhaustively studied. However, by examining the range of near-optimal values within each sub-figure it is typically clear that the algorithm has identified a design peak. The exception to this is seen with the lengths of the first and third devices, in which there is a wide range of values that correspond to near-optimal cases. As a result, the objective function is not believed to be highly sensitive to these variables. To assess if the objective function is sensitive to the ratio of the device diameters and lengths, these ratios are plotted in Fig. 4.6.

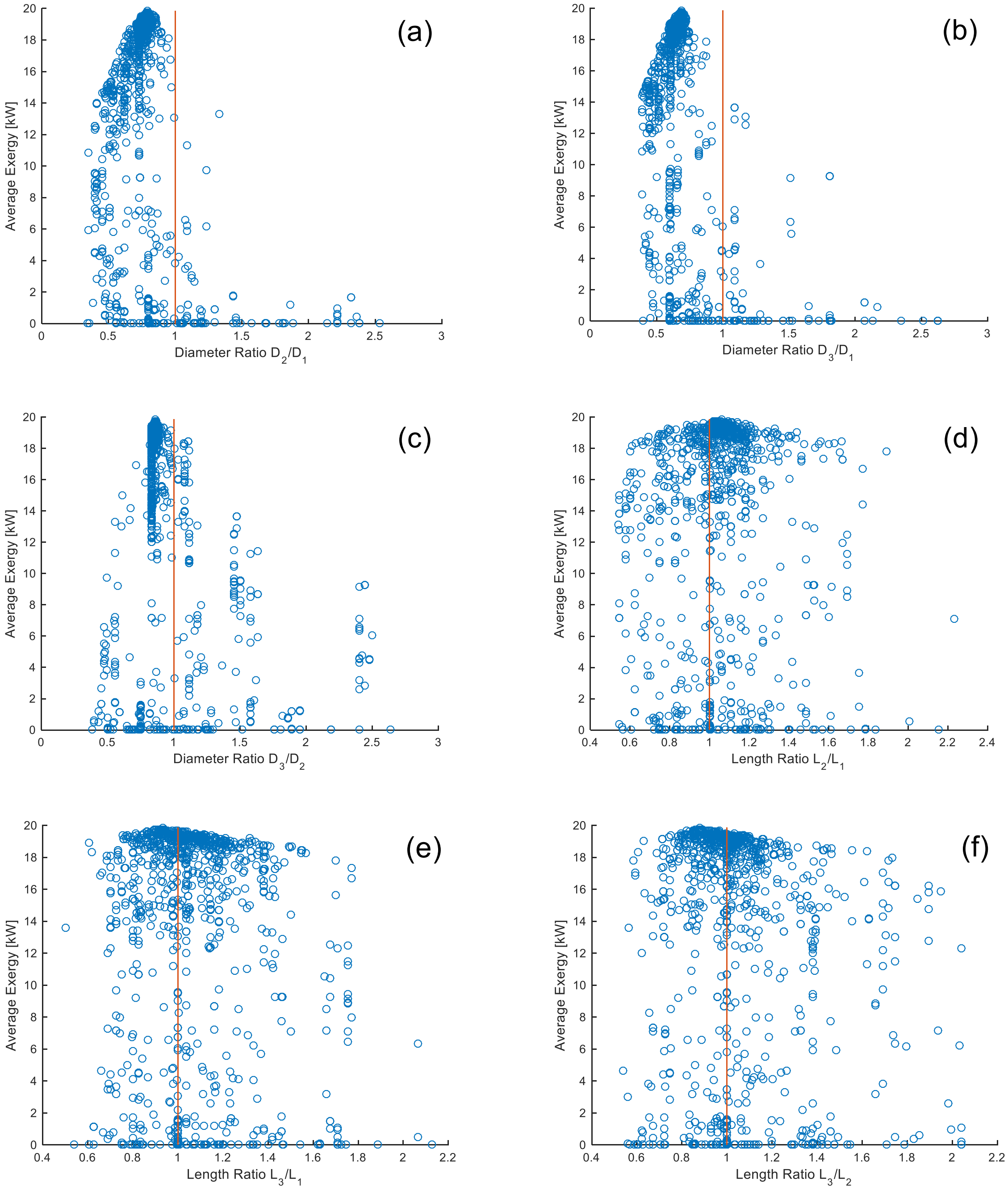

Figure 4.6: Diameter and length ratios between different devices for both stages of the optimization.

As expected, plots of diameter ratios all exhibit a clear peak that is definitively less than one; this is an indication that not only has a near-optimal solution been identified, but that it is a contributing factor in decreasing the volume between devices. Conversely, the length ratios do not exhibit a clear peak, and surprisingly while $\frac{L_3}{L_1} < 1$ and $\frac{L_3}{L_2} < 1$, it can be seen that $\frac{L_2}{L_1} > 1$. This is counter-intuitive, as while the length does not necessarily need to decrease in order for the volume to be reduced in latter devices, there is no straightforward reasoning for why the second device should behave markedly different from the other two devices. Instead, a potential explanation relies on knowledge of the nature of the motion in each device.

While the sea-state impacting each device is identical, the pressure within the piston chamber creates a different PTO force; in turn, this affects the magnitude of the motion of the piston. To provide a basic idea of the magnitude of piston motion for each of the three devices, the average trough and peak height in the piston motion was calculated. This was used to compute the average swept distance of the piston motion in each of the three devices, as well as for each of the six sea-states. The motion is given for the optimal device design in Table 4.5; collision data is also given as a function of each sea-state.

Table 4.5: Mean piston motion as a function of device and sea-state.

Sea-State	**Device 1 (m)**	**Device 2 (m)**	**Device 3 (m)**	**Number of Collisions**
1	0.129	0.116	0.083	0
2	0.243	0.162	0.113	1
3	0.177	0.154	0.100	2
4	0.494	0.479	0.306	12
5	0.592	0.707	0.537	25
6	0.767	0.896	0.779	55

In sea states 1-4, the motion decreases from device 1 to 3; however, in the two highest energy sea-states the motion of device 2 is significantly larger than the other two devices. This trend was also exhibited in a sub-optimal design in which the lengths in device 1, 2, and 3 were approximately constant at 3.4703 m, 3.5256 m, and 3.5112 m respectively. This implies that the changes in motion are pressure driven, rather than merely caused by the changes in lengths themselves. In particular, it is believed that due to the lack of a consistent inlet or outlet pressure in the second device, the motion in the device alternatively experiences high and low pressure states; this pressure variation serves to restrict the motion to low and high sections of the stroke respectively, which ultimately increases the range of motion of the piston.

With an estimate of globally optimum set of design parameters determined, it is necessary to assess the quality of the converter power. The objective function only speaks to the magnitude of the converted energy over the course of the year, not whether the power time series has advantageous characteristics. Therefore, it is possible that the optimal design, while providing a high annual power production, did so through the use of large and infrequent peaks in exergy; this would be severely detrimental to the quality of the power output. Consequently, it is important to assess the time-dependence of exergy production on shorter time-scales.

4.2 Impact of Optimization Procedure on Quality of Converted Power

The incorporation of wave energy into the grid provides a number of significant challenges, as the temporal variation of the converted power introduces instability into the matching of demand and electrical supply. While these challenges are largely outside the scope of this thesis, one can see that a significant issue is the fact that not all power is created equal: ‘useful’ power is consistent and predictable, while sub-optimal power supply may be sporadic. As a result, in the absence of significant daily or seasonal variation, the continuity of power output can be assessed as a basic metric for power quality. Namely, in the ideal case there should be near continual power production on a wave-by-wave basis. Furthermore, while the power produced on a sea-state basis will clearly scale with the energy in the sea-state, the optimal design should not sacrifice power output in lower energy sea-states in order to produce large power spikes in relatively infrequent high-energy seas.

To determine variation in the power output on these shorter time-scales, four representative sets of design variables were selected. These cases are differentiated based on exergy and pressure, such that there are two high and two low pressure cases with a high and low performance case selected for each pressure. Differentiation based on exergy is a measure of how overall performance changes with selection of the other seven design variables. The cases are summarized in Table 4.6; to ensure reproducibility, values to five significant figures are reported.

Table 4.6: Test cases for study of exergy production on smaller time scales.

Case	D_1 [m]	D_2 [m]	D_3 [m]	L_1 [m]	L_2 [m]	L_3 [m]	OR	Pres. [kPa]
L Pres./ H. Obj	1.6298	1.2938	1.1167	3.3400	3.5440	3.1185	0.3744	600.575
L Pres./ L. Obj	1.8367	1.3417	1.5	3.6303	3	3	0.2	600.001
H. Pres./ H. Obj	1.8367	1.3273	1.1282	3.2650	3.3716	3.7083	0.2005	725.303
H. Pres./ L. Obj	2.0621	1.3320	1.2117	2.8803	3.1658	3.0598	0.2702	723.307

The high pressure, high objective function case (H. Pres./H. Obj.) corresponded to the highest average power output of any pressure over 7×10^5 Pa, while the low pressure, high objective case is the optimal design. The exergy for each of these cases is given in Table 4.7.

Table 4.7: Performance data for smaller time scale analysis test cases.

Sea-State	Exergy [kW]	Obj. Function [% of Optimal]
Low Pres. / High Obj.	19.83	100
Low Pres. / Low Obj.	10.65	53.7
High Pres. / High Obj.	12.42	62.6
High Pres. / Low Obj.	7.146	36.0

For each of these four cases, the percent contribution of each sea-state to the average exergy output was determined. The results are presented in Fig. 4.7, as well as the probability of occurrence of each sea-state.

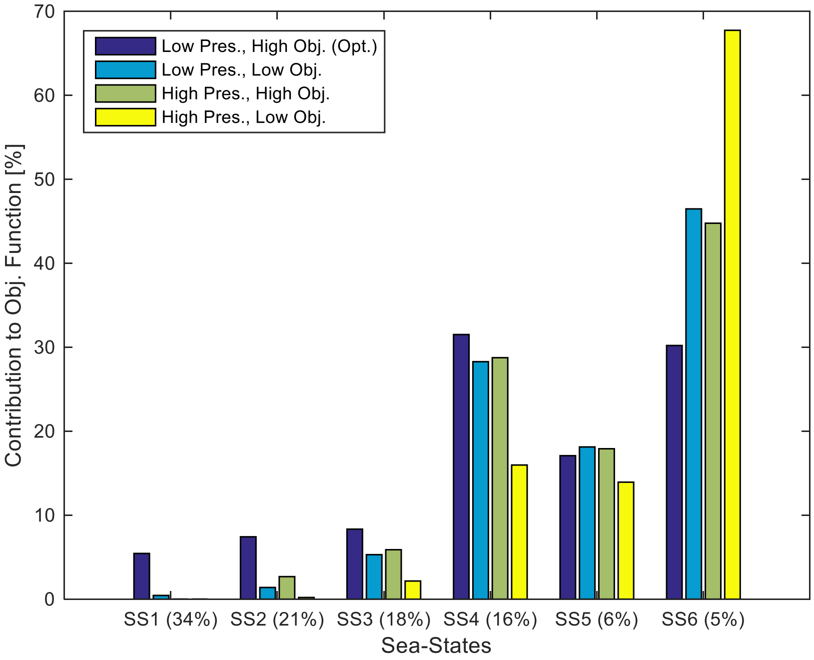

Figure 4.7: Contribution of sea-states to average power output.

While it is expected that higher energy sea-states would have a greater contribution to the average power output, cases with lower objective functions had a more disproportionate contribution from the higher energy sea-states. While the globally optimal case (low pres., high obj.) had a maximum contribution of 31.5% from a particular sea-state, the worst case (high pres., low obj.) had 67.7% of the power output from the highest energy sea-state. In addition to a flattening of the peak power contributions, the optimal case also had the highest contribution of power output from the three lowest energy sea-states. In particular, it was one of only two cases to produce any power in SS1, despite the 34% probability of occurrence of this type of sea-state. It is clear that the optimization algorithm has converged to a case in which power is produced from the complete range of sea-states, especially when compared to sub-optimal cases. This ensures that power is continuously produced throughout the year, and indicates the importance of implementing WEC force control through an optimization of the PTO geometry, rather than a potentially suboptimal selection of PTO parameters.

To assess these four cases on a wave-by-wave basis, a five-minute time series of the cumulative energy output from each WEC was analyzed. The simulation was conducted for T_e =

10.5 s and H_s = 2.25 m (SS4); this sea-state was selected based on the significant power contribution for most cases, and relatively high probability of occurrence.

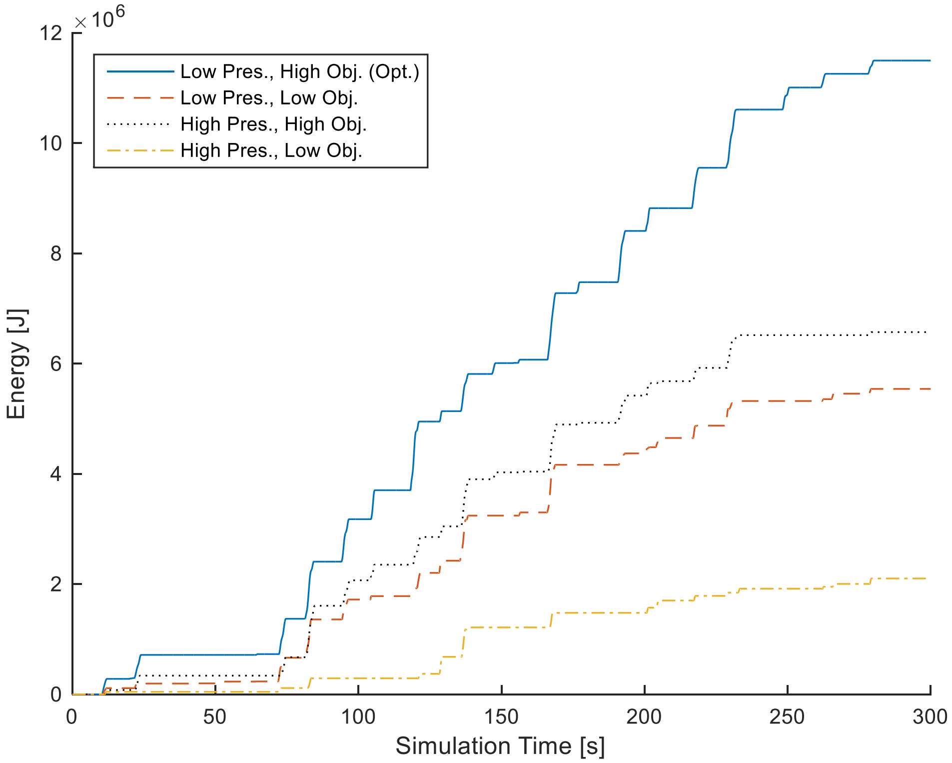

Figure 4.8: Time series of energy output for Te = 10.5 s and Hs = 2.25 m (SS4).

The optimal case had a steady production of power throughout the simulation, which is an indication of smooth power output on a wave-by-wave basis. The energy output from suboptimal cases had an increased reliance on large infrequent contributions.

Therefore, while power quality was not considered directly in the objective function it is clear that the continuity of the power output was not sacrificed in order to produce a high annual power output. Intrinsically, a high annual production is achieved in conjunction by increasing the continuity of power output. However, what may not relate as strongly is the survivability of the device. No consideration was made in the objective function for how the device may be adversely affected by high energy sea-states, and as a result it is possible that the annual power production is increased at the expense of the survivability of the design. A metric for tracking the survivability of the device design is the number of collisions between the piston and its endstops. These collisions will significantly decrease the life of the device; as a result, the effect of collisions is studied in the following section.

4.3 Impact of Optimization Procedure on End-Stop Collision Rate

In addition to measuring the objective function, the number of end-stop collisions in each simulation were tracked. While device survivability is not a primary focus of the present study, this metric provides a coarse basis for assessing the relative feasibility of the optimal design. In particular, while there is no known collision limit at which survivability is ensured, it is safe to state that designs with lower collision rates have a greater chance of surviving high energy wave conditions. To convert the optimization simulation results to a meaningful time scale, the number of collisions in each simulation were used to calculate to an estimate of the expected collisions per minute in real seas, as seen in Eq. 4.1.

$$\frac{Collisions}{minute} = \frac{1}{5} \sum_{Sea\ State=1}^{6} Collisions_i Probability_i \tag{4.1}$$

Collisions are measured as a non-zero instance in the end-stop forces, which are applied if the float moves within 5% of either end of the cylinder (see Eq. 2.7 and 2.8). This method provides a conservative metric of survivability, particularly since the magnitude of each collision is treated equally. However, this data provides important information on the compromise between performance and survivability. For each set of design variables, the expected number of collisions per minute are shown in Fig. 4.9. As a representation of the range of the design space, the cases corresponding to the minimum level of collisions and maximum power are indicated directly.

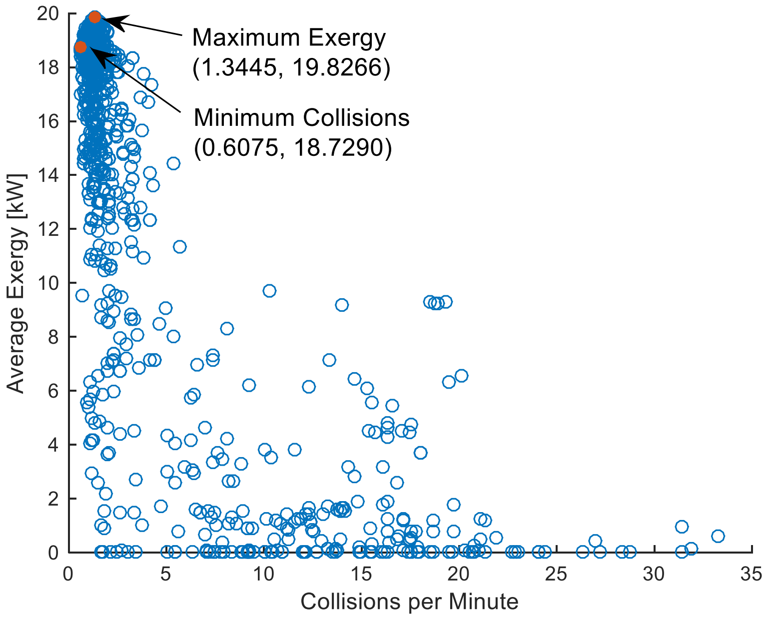

Figure 4.9: Estimated collisions per minute in real seas.

For the two key points on Fig. 4.9, a 5.5% reduction in exergy output correlated to a 55% reduction in collisions. This is an indication that a range of design possibilities exist, with potential compromises in power production in favour of lower collision rates. However, no design possibilities existing with no collisions. The reason behind this was that one of the studied sea-states had a significant wave height of 4.25 m, which was only 0.25 m smaller than the maximum allowable piston length. Consequently, a non-zero collision rate was inevitable. In this extreme sea-state it is likely that the AOE design would need to transition to a survivability-focused configuration, through the application of an active control strategy. If this strategy was implemented, then the collision rate could be calculated as a function of the other five sea-states, to estimate the collision rate in 'power-producing' sea-states. The estimated collision rate in power-producing seas is given in Fig. 4.10.

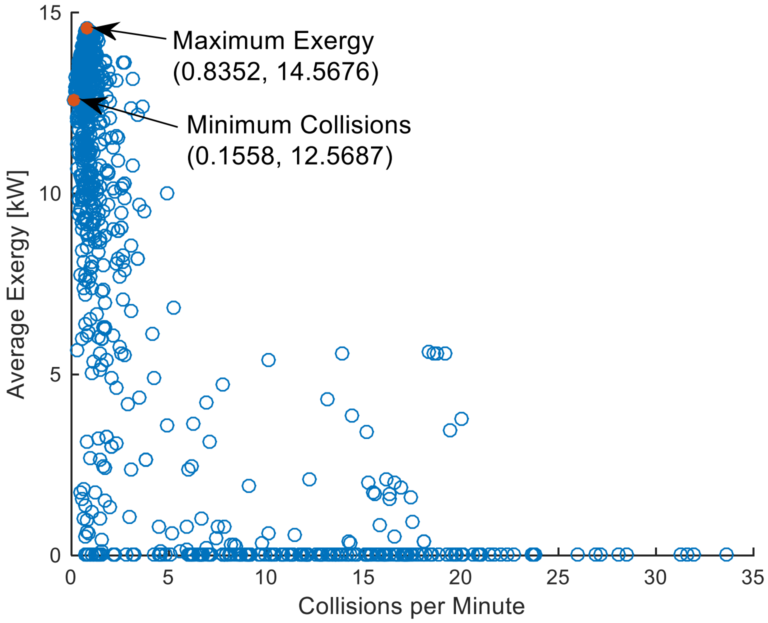

Figure 4.10: Estimated collisions per minute in power-producing seas.

The average exergy production was also calculated as an average over SS1 - SS5, such that that the maximum exergy is shifted to 14.6 kW. Using the set of key points indicated on Fig. 4.10, a 13.7% reduction in exergy correlated to an 81.3% reduction in collisions. Furthermore, the minimum collision rate was 74.4% lower than the best collision case from Fig. 4.9, while only having a 32.9% decrease in exergy. While this collision rate is still likely unacceptable for a final design, there are several design considerations that are worth addressing.

For one, the study of only power-producing seas demonstrates that factors in addition to the design may play a key role in increasing the survivability of the AOE device; these factors may include sea-state dependent control. Furthermore, if high energy sea-states are excluded from consideration, it is possible to achieve much more dramatic reductions in the collision rate with comparatively small decreases in exergy. This is an indication that the survivability-based design space also becomes much wider if a non-design based method (e.g. active control strategy) is used to exclude the highest energy sea-states from consideration. While the function of the current work is not to re-design the AOE device, these considerations may provide potential research directions for both the design of the device and control strategy.

In order to assess some of these design possibilities, it is possible to redefine the objective function as a combination of the average exergy and collision rate. Using the complete set of data shown in Fig. 4.9, the minimum collision rate and maximum exergy were identified and used to as scaling ratios for power and survivability performance in the other design cases. As an example of a potential compromise, these can then be combined with a weighting of 80% exergy and 20% collision rate, in order to provide a revised objective function given by:

$$Obj_{\ rev} = 0.2\frac{Collisions_{min}}{Collisions} + 0.8\frac{Exergy}{Exergy_{max}} \tag{3.10}$$

The revised set of points determined using this alternate objective function is given in Fig. 4.11.

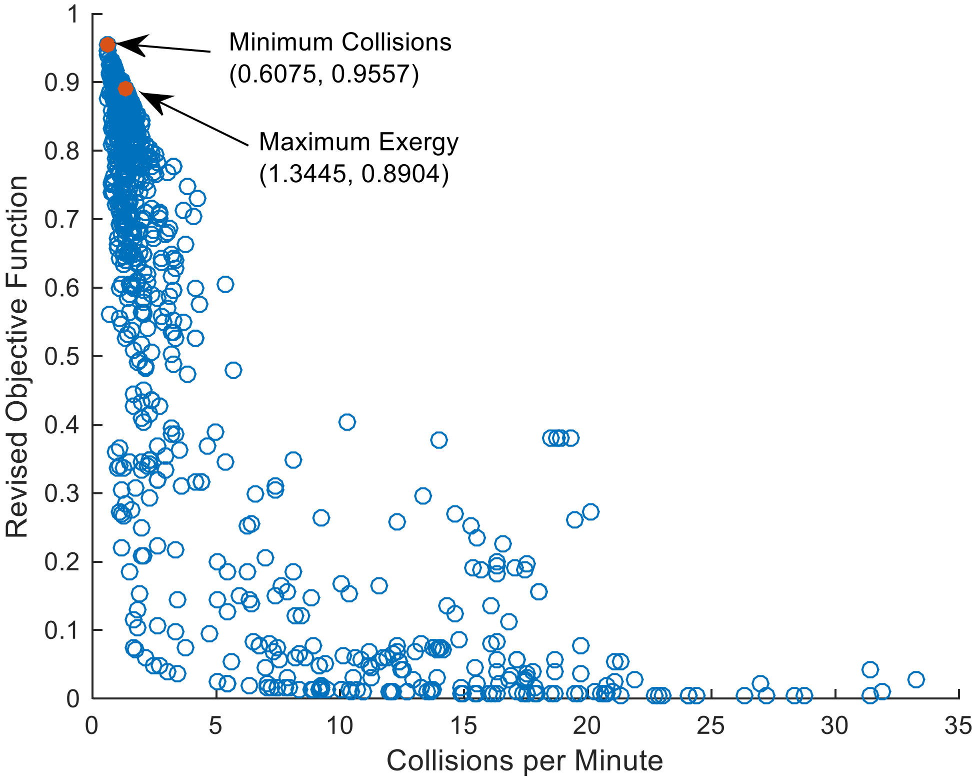

Figure 4.11: Revised objective function incorporating collision effects.

The optimal case using this revised objective function (maximum exergy) is given in Table 4.8, along with a comparison to the optimal case provided by the optimization algorithm.

Table 4.8: Optimum set of design variables determined using alternate objective function.

Design Variable	**Value – Optimization**	**Value – Revised Obj.**	**% Change**
Diameter, Device 1	1.6298 m	1.6444 m	+0.9%
Diameter, Device 2	1.2938 m	1.2243 m	-5.4%
Diameter, Device 3	1.1167 m	1.1152 m	-0.1%
Orifice Ratio	0.3744	0.3562	-4.9%
Length, Device 1	3.3400 m	3.6026 m	+7.9%
Length, Device 2	3.5440 m	4.0299 m	+13.7%
Length, Device 3	3.1185 m	4.0190 m	+28.9%
Crack Pressure	600.75 kPa	600.00 kPa	-0.1%
Average Exergy	19.83 kW	18.73 kW	-5.5%
Collision Rate	1.3445 /min	0.6075 /min	-54.8%
Revised Obj.	0.8904	0.9557	+7.3%

The optimal value for the collision-dependent fitness function had the smallest possible collision rate of any of the sets of parameters, due to the relatively small compromise in exergy for a large reduction in the number of collisions. To achieve this reduction in collisions, the length of each of the devices was increased significantly, particularly in latter devices.

This study on the inclusionary effect of collisions in the objective function presents an indication of the type and magnitude of design changes that are needed to reach a compromise between power production and survivability. However, as mentioned these considerations are not resolved in the present study. Instead, the optimal design produced by the optimization procedure (contained in Table 4.4) is carried forward for the development of the active control strategy. In order to provide a base case against which the actively controlled device performance can be measured, a power matrix is developed using the optimal PTO geometry, otherwise referred to as the passively controlled system.

4.4 Power Matrix for Passively Controlled System

A power matrix provides a method of tracking device performance across a range of sea-states, which can be overlaid with the wave histogram for a particular location in order to provide estimates of annual power production. For the present study, the power matrix was generated using a 10-year averaged wave histogram for Amphitrite Bank, for which the data was generated by Robertson et al using an SNL-SWAN model [5]. The use of SNL-SWAN serves to smooth out variation associated with buoy measurements, which in conjunction with the input of 10 years of wave data, provides a strong representation of the wave climate. To reduce computational time, not every sea-state was included in the power matrix. Instead, focus was placed on sea-states with over 24 hours of occurrence annually; however, the study was rounded out with other sea-states of interest. The 66 sea-states used as a representation of the overall wave histogram are included in Fig. 4.12.

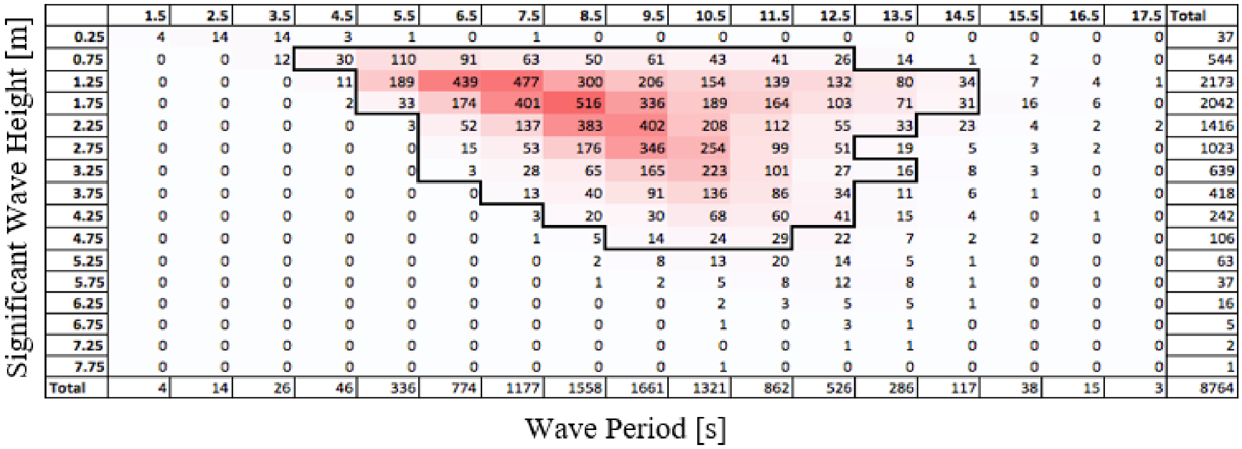

	1.5	2.5	3.5	4.5	5.5	6.5	7.5	8.5	9.5	10.5	11.5	12.5	13.5	14.5	15.5	16.5	17.5	Total
0.25	4	14	14	3	1	0	1	0	0	0	0	0	0	0	0	0	0	37
0.75	0	0	12	30	110	91	63	50	61	43	41	26	14	1	2	0	0	544
1.25	0	0	0	11	189	439	477	300	206	154	139	132	80	34	7	4	1	2173
1.75	0	0	0	2	33	174	401	516	336	189	164	103	71	31	16	6	0	2042
2.25	0	0	0	0	3	52	137	383	402	208	112	55	33	23	4	2	2	1416
2.75	0	0	0	0	0	15	53	176	346	254	99	51	19	5	3	2	0	1023
3.25	0	0	0	0	0	3	28	65	165	223	101	27	16	8	3	0	0	639
3.75	0	0	0	0	0	0	13	40	91	136	86	34	11	6	1	0	0	418
4.25	0	0	0	0	0	0	3	20	30	68	60	41	15	4	0	1	0	242
4.75	0	0	0	0	0	0	1	5	14	24	29	22	7	2	2	0	0	106
5.25	0	0	0	0	0	0	0	2	8	13	20	14	5	1	0	0	0	63
5.75	0	0	0	0	0	0	0	1	2	5	8	12	8	1	0	0	0	37
6.25	0	0	0	0	0	0	0	0	0	2	3	5	5	1	0	0	0	16
6.75	0	0	0	0	0	0	0	0	0	1	0	3	1	0	0	0	0	5
7.25	0	0	0	0	0	0	0	0	0	0	0	1	1	0	0	0	0	2
7.75	0	0	0	0	0	0	0	0	0	1	0	0	0	0	0	0	0	1
Total	4	14	26	46	336	774	1177	1558	1661	1321	862	526	286	117	38	15	3	8764

Figure 4.12: Wave histogram of sea-state frequency of occurrence for Amphitrite Bank [2], in which the sea-states used to generate power matrix are indicated.

The sea-states included in the power matrix calculation represent 95.54% of the hours of the year, and cover sufficient breadth of the common wave heights and periods to provide an accurate representation of the Amphitrite Bank location. Furthermore, the selected sea-states account for 84.49% of the total wave power transport throughout the year.

A total of 450 wave segments were used to represent each of these sea-states, which were spread across 15 directions; the phases of each of the components were randomly generated in order to ensure the sea-state is representative of a realistic wave condition. This aligns with the Det Norske Veritas (DNV) recommendation of a minimum of 100 frequency components for standard seas, or 1000 components in extreme seas [64]. The simulations were run for 20 minutes following an initialization period of 200 s in order to comply with IEC standards [65].

The initialization period changed from that of the optimization in order to reduce the risk of power being artificially injected into the system by means of running a moderate sea-state at the beginning of the simulation; this risk is no longer necessary due to the longer simulation length. The power matrix data was generated using these established requirements, for which the results are given in the following section.

4.4.1 Power Matrix Results

The power matrix for the AOE device is given in Fig. 4.13. The power is calculated using flow exergy, in order to provide an estimate of the total useful power output from the converter.

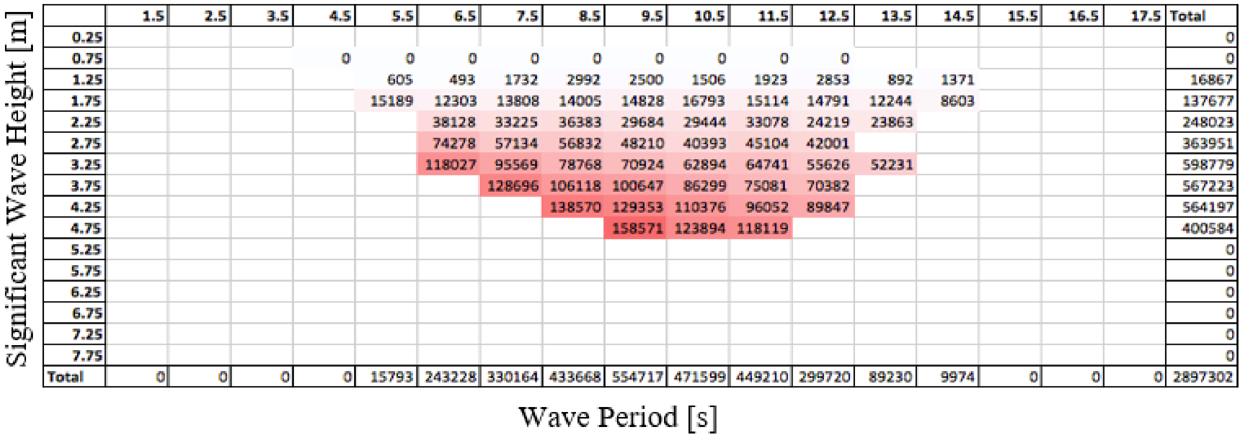

	1.5	2.5	3.5	4.5	5.5	6.5	7.5	8.5	9.5	10.5	11.5	12.5	13.5	14.5	15.5	16.5	17.5	Total
0.25																		0
0.75				0	0	0	0	0	0	0	0	0						0
1.25					605	493	1732	2992	2500	1506	1923	2853	892	1371				16867
1.75					15189	12303	13808	14005	14828	16793	15114	14791	12244	8603				137677
2.25						38128	33225	36383	29684	29444	33078	24219	23863					248023
2.75						74278	57134	56832	48210	40393	45104	42001						363951
3.25						118027	95569	78768	70924	62894	64741	55626	52231					598779
3.75							128696	106118	100647	86299	75081	70382						567223
4.25								138570	129353	110376	96052	89847						564197
4.75									158571	123894	118119							400584
5.25																		0
5.75																		0
6.25																		0
6.75																		0
7.25																		0
7.75																		0
Total	0	0	0	0	15793	243228	330164	433668	554717	471599	449210	299720	89230	9974	0	0	0	2897302

Figure 4.13: Power production [W] as a function of sea-state for passively controlled system.

As expected, the power production increases with significant wave height; for a particular height, the power production decreases with energy period. The maximum power production of 158.6 kW is reached in 4.75 m waves with an energy period of 9.5 s; conversely, the minimum of 0 kW is achieved in all sea-states of 0.75 m. For these sea-states, power was produced from the first two devices in the cascade; however, the crack pressure in the third device was never reached. As a result, no useful power (compressed air over 6 bar) was produced. However, these maximum and minimum values for power production are achieved in relatively infrequent sea-states. In order to determine the relative contribution of each sea-state to the annual energy production, the power matrix is overlaid with the hours of occurrence for the Amphitrite Bank location, as given in Fig. 4.14.

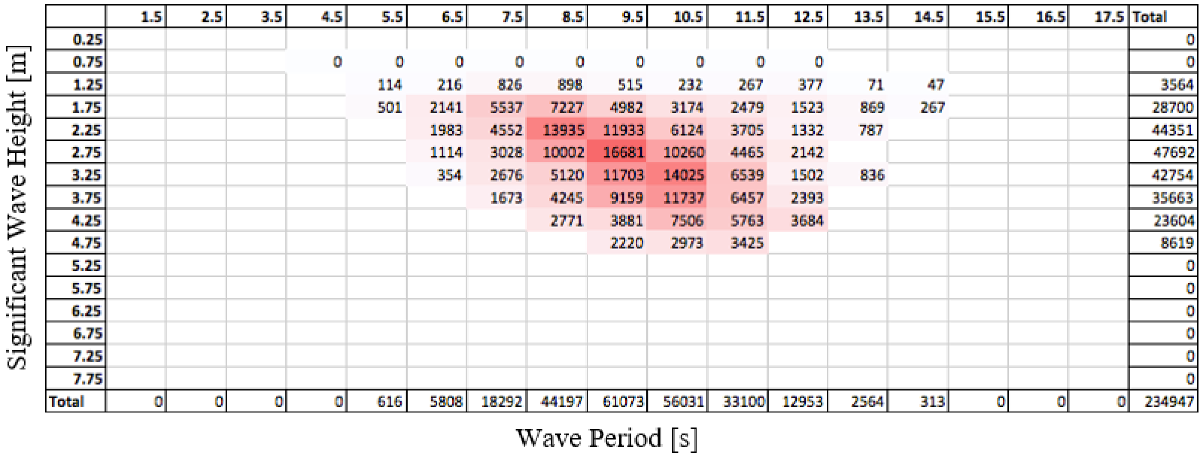

	1.5	2.5	3.5	4.5	5.5	6.5	7.5	8.5	9.5	10.5	11.5	12.5	13.5	14.5	15.5	16.5	17.5	Total
0.25																		0
0.75				0	0	0	0	0	0	0	0	0						0
1.25					114	216	826	898	515	232	267	377	71	47				3564
1.75					501	2141	5537	7227	4982	3174	2479	1523	869	267				28700
2.25						1983	4552	13935	11933	6124	3705	1332	787					44351
2.75						1114	3028	10002	16681	10260	4465	2142						47692
3.25						354	2676	5120	11703	14025	6539	1502	836					42754
3.75							1673	4245	9159	11737	6457	2393						35663
4.25								2771	3881	7506	5763	3684						23604
4.75									2220	2973	3425							8619
5.25																		0
5.75																		0
6.25																		0
6.75																		0
7.25																		0
7.75																		0
Total	0	0	0	0	616	5808	18292	44197	61073	56031	33100	12953	2564	313	0	0	0	234947

Figure 4.14: Annual energy [kWh] as a function of sea-state for passively controlled system.

For the Amphitrite Bank location, moderate sea-states account for the bulk of the energy production, while low energy sea-states, particularly those with a wave height below 1.75 m, provide relatively small contributions. In total, the 66 studied sea-states result in the generation of 234.9 MWh, which is produced over 95.54% of the year. When converting this average to production over the entire year, the AOE device generates an average of 29.37 kW. This power comes solely out of the third device, since the feed-through of the first two devices is contained within the system. In order to assess the relative contribution of the three devices to the power output, the power increase from the first to second, and second to third device is given in Fig. 4.15 and Fig. 4.16, respectively.

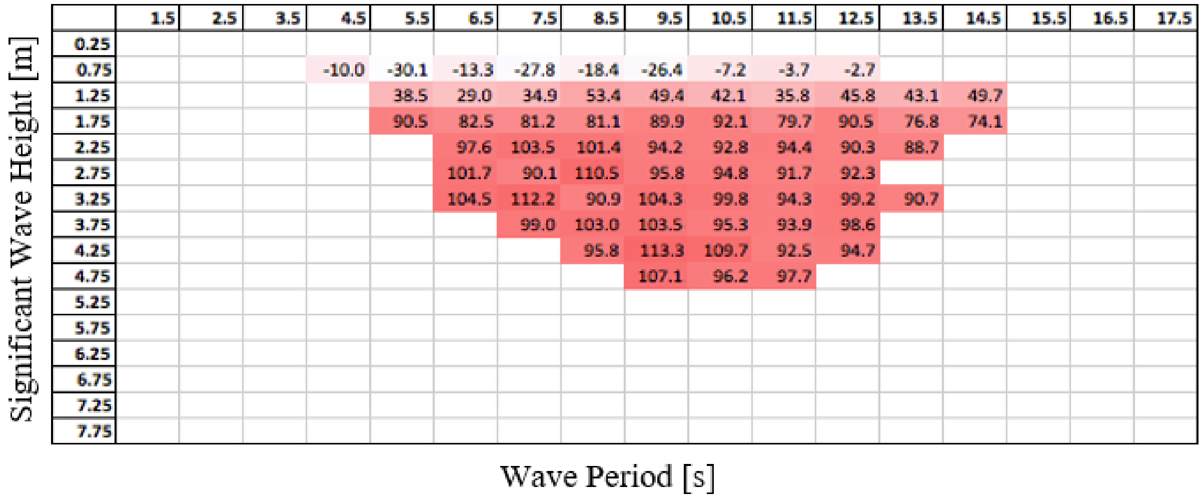

	1.5	2.5	3.5	4.5	5.5	6.5	7.5	8.5	9.5	10.5	11.5	12.5	13.5	14.5	15.5	16.5	17.5
0.25																	
0.75				-10.0	-30.1	-13.3	-27.8	-18.4	-26.4	-7.2	-3.7	-2.7					
1.25					38.5	29.0	34.9	53.4	49.4	42.1	35.8	45.8	43.1	49.7			
1.75					90.5	82.5	81.2	81.1	89.9	92.1	79.7	90.5	76.8	74.1			
2.25						97.6	103.5	101.4	94.2	92.8	94.4	90.3	88.7				
2.75						101.7	90.1	110.5	95.8	94.8	91.7	92.3					
3.25						104.5	112.2	90.9	104.3	99.8	94.3	99.2	90.7				
3.75							99.0	103.0	103.5	95.3	93.9	98.6					
4.25								95.8	113.3	109.7	92.5	94.7					
4.75									107.1	96.2	97.7						
5.25																	
5.75																	
6.25																	
6.75																	
7.25																	
7.75																	

Figure 4.15: Percentage increase in power from device 1 to device 2 as a function sea-state for passively controlled system.

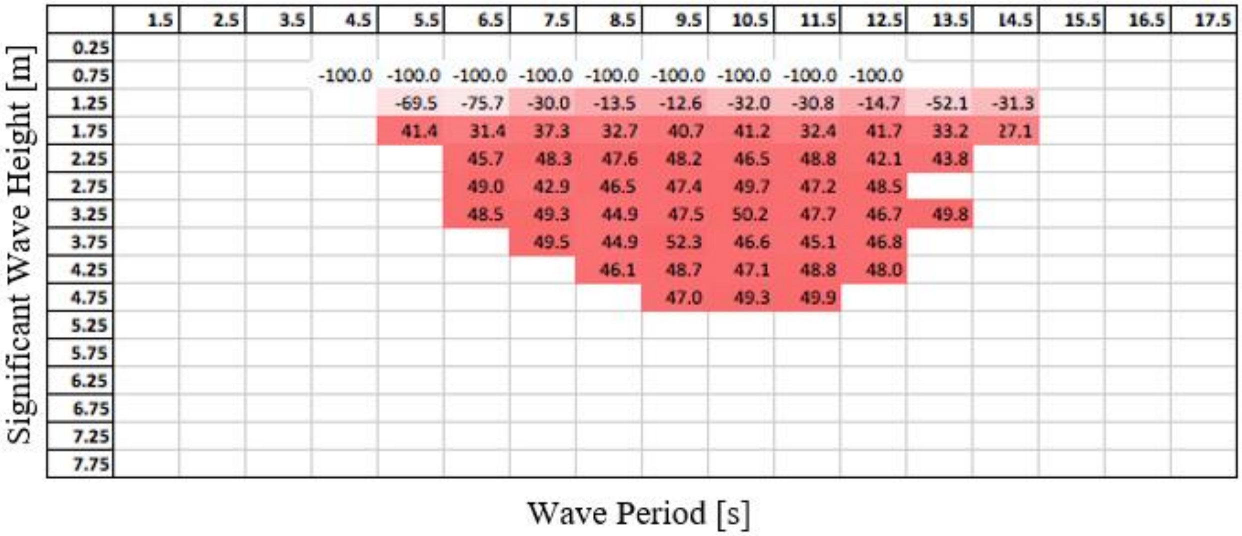

	1.5	2.5	3.5	4.5	5.5	6.5	7.5	8.5	9.5	10.5	11.5	12.5	13.5	14.5	15.5	16.5	17.5
0.25																	
0.75				-100.0	-100.0	-100.0	-100.0	-100.0	-100.0	-100.0	-100.0	-100.0					
1.25					-69.5	-75.7	-30.0	-13.5	-12.6	-32.0	-30.8	-14.7	-52.1	-31.3			
1.75					41.4	31.4	37.3	32.7	40.7	41.2	32.4	41.7	33.2	27.1			
2.25						45.7	48.3	47.6	48.2	46.5	48.8	42.1	43.8				
2.75						49.0	42.9	46.5	47.4	49.7	47.2	48.5					
3.25						48.5	49.3	44.9	47.5	50.2	47.7	46.7	49.8				
3.75							49.5	44.9	52.3	46.6	45.1	46.8					
4.25								46.1	48.7	47.1	48.8	48.0					
4.75									47.0	49.3	49.9						
5.25																	
5.75																	
6.25																	
6.75																	
7.25																	
7.75																	

Figure 4.16: Percentage increase in power from device 2 to device 3 as a function of sea-state for passively controlled system.

These figures illustrate several trends in how air flows between devices. In sea-states with heights below 2.25 m, the pressure requirements of the final device, as well as the pressure increase from the first to the second device, hinders flow between devices. As a result, the energy production successively decreases in the chain of devices, despite the increase in exergy per unit volume of flow as the air is compressed. Conversely, in higher energy seas there is a consistent increase of approximately 100% from the first device to the second, and an additional 50% from the second to third. This demonstrates that there is no net improvement to introducing more devices in the cascade, as each device adds approximately the same power output in high energy seas. Collectively, there is no net gain in introducing more devices, while harboring a risk in low energy seas that there will be a successive reduction in power with the introduction of more devices. However, this configuration is necessary for meeting the minimum on-shore pressure requirement needed for conversion of pressurized air to electricity.

To further illustrate the nature of the power transport in the AOE WEC, the efficiency of the device is calculated as a function of the absorbed power. The absorbed power is calculated as the work due to the motion of the piston, which is given in Eq. 4.2.

$$\begin{aligned} Absorbed\ Energy &= -\int_{t=1}^{t_{total}} \frac{dV_{cyl}}{dt}(P_{Cyl,ch,2} - P_{Cyl,ch,1}) \\ &= -\int_{t=1}^{t_{total}} \frac{dz}{dt} A_{cyl}(P_{Cyl,ch.2} - P_{Cyl,ch,1}) \end{aligned} \tag{4.2}$$

Eq. 4.2 is merely the integration of the PTO force multiplied by the velocity of the float. However, this integral is not straightforward to calculate. While the Simulink model uses a constant time step, the ProteusDS model uses a variable time step in order to resolve high frequency motion. Consequently, the velocity is not constant over a single Simulink time step, such that $-\int_{t=1}^{t_{total}} \frac{dz}{dt} A_{cyl}(P_{Cyl,ch,2} - P_{Cyl,ch,1}) \neq \sum_{t=1}^{t_{total}} \frac{dz}{dt} A_{cyl}(P_{Cyl,ch,2} - P_{Cyl,ch,1})\Delta t$. Therefore, it is necessary to calculate the absorbed energy directly using the change in internal energy of the piston. The total internal energy change in the piston across a time step from $t \rightarrow t+1$ is given in Eq. 4.3.

$$\begin{aligned} \Delta U = {} & (m_{Cyl,ch.1} C_v T_{Cyl,ch.1})_{t+1} - (m_{Cyl,ch.1} C_v T_{Cyl,ch.1})_t + (m_{Cyl,ch.2} C_v T_{Cyl,ch.2})_{t+1} \\ & - (m_{Cyl,ch.2} C_v T_{Cyl,ch.2})_t \end{aligned} \tag{4.3}$$

The component of the internal energy change resulting from the motion of the piston is given in Eq. 4.4.

$$\begin{aligned} Absorbed\ Energy = {} & \sum_{t=1}^{t_{total}} \left(\frac{1}{\gamma - 1}\right) A_{cyl}(z_{t+1} - z_t)(P_{Cyl,ch,2} - P_{Cyl,ch,1}) \\ & - \left(\frac{\gamma}{\gamma - 1}\right) \frac{dz}{dt} A_{cyl} \Delta t \left(P_{Ch.2} \left(\frac{L_{cyl} + z_{t+1}}{L_{cyl} + z_t}\right) - P_{Ch.1} \left(\frac{L_{cyl} - z_{t+1}}{L_{cyl} - z_t}\right) \right) \end{aligned} \tag{4.4}$$

Using the above, the average absorbed power is calculated as a function of sea-state. As with the power output, which is the cumulative sum of power production across all three devices, the sum of the absorbed power is given in Fig. 4.17.

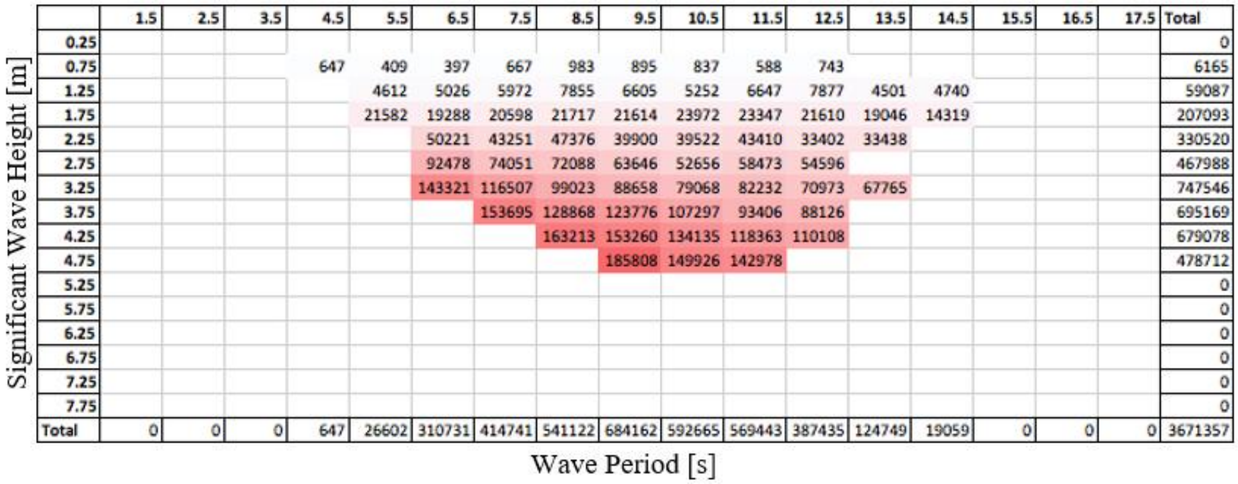

	1.5	2.5	3.5	4.5	5.5	6.5	7.5	8.5	9.5	10.5	11.5	12.5	13.5	14.5	15.5	16.5	17.5	Total
0.25																		0
0.75				647	409	397	667	983	895	837	588	743						6165
1.25					4612	5026	5972	7855	6605	5252	6647	7877	4501	4740				59087
1.75					21582	19288	20598	21717	21614	23972	23347	21610	19046	14319				207093
2.25						50221	43251	47376	39900	39522	43410	33402	33438					330520
2.75						92478	74051	72088	63646	52656	58473	54596						467988
3.25						143321	116507	99023	88658	79068	82232	70973	67765					747546
3.75							153695	128868	123776	107297	93406	88126						695169
4.25								163213	153260	134135	118363	110108						679078
4.75									185808	149926	142978							478712
5.25																		0
5.75																		0
6.25																		0
6.75																		0
7.25																		0
7.75																		0
Total	0	0	0	647	26602	310731	414741	541122	684162	592665	569443	387435	124749	19059	0	0	0	3671357

Figure 4.17: Absorbed power [W] as a function of Hs [m] and Te [s] for passively controlled system.

The absorbed power in wave heights of 0.75 m – 1.25 m is several orders of magnitude below that of higher energy wave conditions. In particular, in the lowest energy sea-states, virtually no power is absorbed. The reason for this is that when the piston is compressed, the pressure is increased as a result of the absorption of energy; however, there must be mass transfer between devices in order to retain this energy. If no mass transfer occurs, the energy is passed directly back to the system when the piston chamber expands, which creates an air spring effect in which no energy is absorbed. Therefore, in high energy seas with frequency mass flow events, a larger amount of power is absorbed.

Using the absorbed power, coupled with the change in internal state between the start and end of the simulation, the conversion efficiency of the WEC can be calculated. This efficiency is calculated using Eq. 4.5 as a measure of the readiness with which absorbed power is converted to useful power output.

$$Conversion\ Efficiency = \frac{\sum_{t=1}^{t_{total}} P_{Produced}\Delta t + E_{Final} - E_{inital}}{\sum_{t=1}^{t_{total}} P_{Absorbed}\Delta t} \qquad (4.5)$$

Using the above, the conversion efficiency is computed as a function of sea-state, as seen in Fig. 4.18.

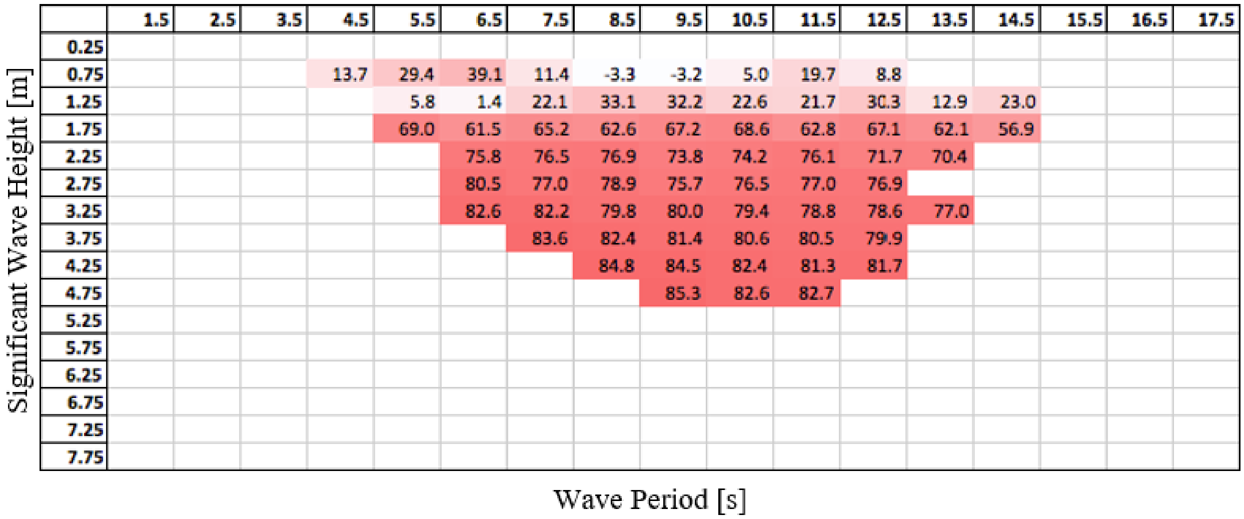

	1.5	2.5	3.5	4.5	5.5	6.5	7.5	8.5	9.5	10.5	11.5	12.5	13.5	14.5	15.5	16.5	17.5
0.25																	
0.75				13.7	29.4	39.1	11.4	-3.3	-3.2	5.0	19.7	8.8					
1.25					5.8	1.4	22.1	33.1	32.2	22.6	21.7	30.3	12.9	23.0			
1.75					69.0	61.5	65.2	62.6	67.2	68.6	62.8	67.1	62.1	56.9			
2.25						75.8	76.5	76.9	73.8	74.2	76.1	71.7	70.4				
2.75						80.5	77.0	78.9	75.7	76.5	77.0	76.9					
3.25						82.6	82.2	79.8	80.0	79.4	78.8	78.6	77.0				
3.75							83.6	82.4	81.4	80.6	80.5	79.9					
4.25								84.8	84.5	82.4	81.3	81.7					
4.75									85.3	82.6	82.7						
5.25																	
5.75																	
6.25																	
6.75																	
7.25																	
7.75																	

Figure 4.18: Conversion efficiency [%] as a function of Hs [m] and Te [s] for passively controlled system.

When considering the annual total of absorbed and produced energy, the annually-averaged conversion efficiency is 74.3%. The efficiency in each particular sea-state increases with the significant wave height, such that a peak efficiency of 85.3% is reached in 4.75 m waves with an energy period of 9.5 s. This peak value is relatively consistent across moderate and high energy sea-states, all of which have efficiencies over 70%. This efficiency is relatively high, as the only losses are heat transfer to the surroundings and friction in the piston. In high energy sea-states, heat transfer losses are reduced as the residency time of air within the system is low. However, in sea states with wave heights of 0.75 m or 1.25 m, these heat transfer losses are significant; in particular, the lowest efficiency is actually negative. In these cases, energy was lost from the system throughout the course of the simulation, as the air that was present in the WEC following the initialization period of 200 s was gradually reduced in temperature, while only marginal airflow into the system occurred. This band of low efficiency sea-states occupies all wave conditions below 1.25 m. Within this band, the highest efficiency of 39.1% is reached in 0.75 m waves with an energy period of 6.5 s. This efficiency was likely artificially driven up by the fact that very little energy was absorbed, due to the infrequency of mass-flow events. Consequently, a better measure of how efficiently the device works in a particular sea-state is the absorption efficiency, which is computed using Eq. 4.6, for which the denominator is the wave power transport per metre [55], multiplied by the collective wave front of the device.

$$Absorption\ Efficiency = \frac{\sum_{t=1}^{t_{total}} P_{Absorbed} \Delta t}{3D_{float}(490T_e H_s^2)} \tag{4.6}$$

For the AOE device, the wave front is three times the float diameter, or 32.91 m. The resulting absorption efficiency is given in Fig. 4.19.

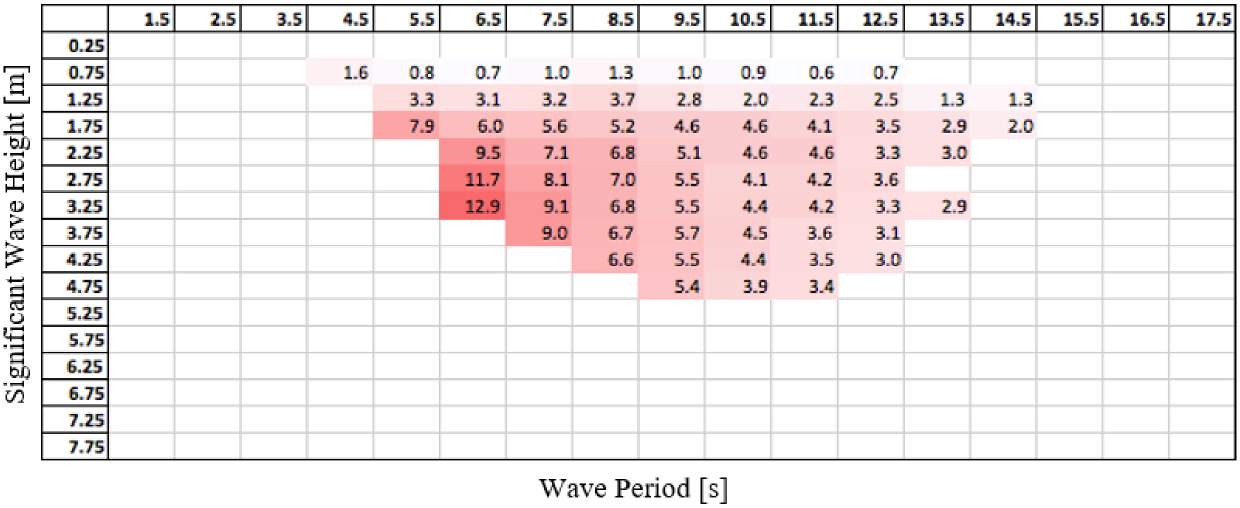

	1.5	2.5	3.5	4.5	5.5	6.5	7.5	8.5	9.5	10.5	11.5	12.5	13.5	14.5	15.5	16.5	17.5
0.25																	
0.75				1.6	0.8	0.7	1.0	1.3	1.0	0.9	0.6	0.7					
1.25					3.3	3.1	3.2	3.7	2.8	2.0	2.3	2.5	1.3	1.3			
1.75					7.9	6.0	5.6	5.2	4.6	4.6	4.1	3.5	2.9	2.0			
2.25						9.5	7.1	6.8	5.1	4.6	4.6	3.3	3.0				
2.75						11.7	8.1	7.0	5.5	4.1	4.2	3.6					
3.25						12.9	9.1	6.8	5.5	4.4	4.2	3.3	2.9				
3.75							9.0	6.7	5.7	4.5	3.6	3.1					
4.25								6.6	5.5	4.4	3.5	3.0					
4.75									5.4	3.9	3.4						
5.25																	
5.75																	
6.25																	
6.75																	
7.25																	
7.75																	

Figure 4.19: Absorption efficiency [%] as a function of Hs [m] and Te [s] for passively controlled system.

When considering the total absorbed energy annually, the annually-averaged absorption efficiency is 4.7%. To summarize the sea-state dependent efficiency of the converter, the conversion and absorption efficiencies were computed for each wave – height band within the wave histogram. The results are summarized in Table 4.9. The total efficiency is determined as the product of the conversion and absorption efficiencies.

Table 4.9: Summary of the efficiency and energy production of the AOE WEC as a function of significant wave height.

Wave Height [m]	**0.75**	**1.25**	**1.75**	**2.25**	**2.75**	**3.25**	**3.75**	**4.25**	**4.75**
Conversion Efficiency [%]	17.12	19.13	64.59	75.09	76.79	79.56	80.96	82.51	83.19
Absorption Efficiency [%]	0.90	2.91	4.92	5.72	5.40	5.08	4.84	4.26	4.01
Total Efficiency [%]	0.13	0.56	3.18	4.31	4.16	4.05	3.93	3.52	3.34
Probability of Occurrence [%]	6.15	25.68	24.10	16.51	11.87	7.50	4.78	2.62	0.80
Component of Annual Wave Power Transport [%]	0.55	6.98	13.72	16.02	17.84	16.42	14.14	10.39	3.93
Component of Energy Production [%]	0.00	1.52	12.22	18.88	20.30	18.20	15.18	10.05	3.67

NOTE: All probabilities are calculated relative to the sea-states included in the generation of the PM spectrum, not all sea-states annually. These values were selected to ensure the scaling of the percentage difference in the resource and energy production was consistent.

Table 4.9 serves to illustrate the large discrepancy in the energy production in high energy sea-states when compared to low energy wave conditions. When considering solely the sea-states used in the generation of the power matrix, seas with wave heights between 0.75 m – 1.75 m encompass 55.93% of the hours, but only account for 13.74% of the energy production. Aside from the highest energy sea-state of 4.75 m wave height, these three low energy cases are the only wave conditions to contribute less than their percentage of the annual wave power transport. In large part, this is due to the net efficiencies of less than 1% for the 0.75 m and 1.25m sea-states. This was significantly lower than the annually-averaged efficiency of 3.5%. Aside from the lowest energy sea-states, the production of energy is fairly consistent, however, which speaks to the continuity of power production from the AOE WEC. This data provides a strong idea of sea-states to target in the development of a power-maximizing active control strategy. Prior to the selection of this strategy, however, it is necessary to confirm that the optimization methodology leading to the selection of a finalized PTO geometry was valid. To do so, the power matrix data is compared to the optimization results, in order to confirm that the calculated power output was consistent.

4.4.2 Comparison to Optimization Results

In order to fulfill the IEC requirements for creating an accurate power matrix, the simulation duration and sea-state were altered from that used in the optimization procedure. In particular, the duration was increased from 5 minutes to 20 minutes, in addition to the use of a different initialization condition. Furthermore, the number of frequencies used in re-creating the desired sea-state was increased from 140 to 450. As a result, it is expected that exergy results will vary slightly from those produced in the optimization, as seen in Table 4.10. An annual estimate is calculated using the same sea-state weighting used in the optimization procedure.

Table 4.10: Comparison of sea-state dependent exergy in optimization and power matrix results.

Sea-State	**H_s [m]**	**T_e [s]**	**Average Exergy – Power Matrix [kW]**	**Average Exergy - Optimization [kW]**	**% Change**
1	1.25	6.5	0.493	3.166	+542.2
2	1.75	8.5	14.01	7.055	-49.6
3	1.75	9.5	14.83	9.187	-38.0
4	2.25	10.5	29.44	38.33	+30.2
5	3.25	13.5	52.23	58.70	+12.4
6	4.25	10.5	110.4	119.54	+8.3
Annual Estimate			19.10	19.83	+3.8

Particularly in low-energy sea-states, there is a large discrepancy in the exergy production seen in the optimization and the power matrix. This difference is not consistently positive, which is an indication that rather than a consistent misrepresentation of the power production, the differences instead arise from the nature of the AOE device; in particular, since the objective of the WEC is to produce a finite pressure ratio, the device is dependent on infrequent contributions from high energy waves. This results in high wave-by-wave dependence in sea-states 1 and 2 in particular, for which changes in the wave spectrum components would have resulted in substantial differences in exergy production. Conversely, in higher energy sea-states (such as 5 and 6), the power production levels were much closer; within these sea-states, even moderate waves provide sufficient power to meet the finite pressure ratio, such that wave-by-wave dependence is lessened. Overall, the annual power production estimate provided by the optimization aligns well with that provided by the power matrix, when the same probabilities of occurrence are used for both cases.

When compared to the average power prediction of 29.37 kW calculated using data from all 66 sea-states, however, the optimization estimate of 19.83 kW was much lower. This is an indication that the probabilities of occurrence in the optimization overvalued low energy sea-states. This was done intentionally since the weighting used to calculate the representative sea-state within each section was based on hours of occurrence, not energy. This ensured that focus was placed on optimizing sea-states with a high probability of occurrence. Therefore, the discrepancy in the annual power estimate does not invalidate the optimization procedure.

Consequently, it can be stated that the optimization procedure provided a strong holistic representation of the performance of the WEC in real-seas, when measured against power matrix data obtained according to IEC standards. Therefore, the optimal design selected with the optimization procedure can be carried forward in the design process to the implementation of an active control strategy.

4.5 Summary of Passive Control Implementation

Through the implementation of passive control in the AOE WEC, significant improvements in exergy output, as well as power quality, were generated. The formulation of the passive control problem was realized as an optimization of eight critical PTO parameters, for which over 15 generations there was a net increase of 330.35% in the objective function; the objective function provided an estimate of the annual exergy output at the Amphitrite Bank deployment location. Over the course of the optimization, a total of 942 unique variable combinations were studied. Consequently, while it is unlikely that a global optimum was identified, the optimization was halted due to progressively smaller increases in latter generations, as well as a decrease in the range of values within each generation.

The spread of performance across the studied designs demonstrates the sensitivity of the optimal design to particular design parameters; this provides motivation for resolving these geometries in the model of the device. In addition, when considering the significant performance improvement over the initial ‘best guess’ of the optimal geometry that was used in the first generation, there is clear value in the implementation of passive PTO force control. In particular, there is reduced reliance on complete knowledge of the WEC design space when attempting to maximize power output; however, several other benefits were also identified. When compared to several sub-optimal designs, the optimal design exhibited an increase in power quality, as measured by the continuity of power output on both a sea-state by sea-state and wave-by-wave basis. Furthermore, the end-stop collision rate for the optimal design was compared to the complete design space in order to identify potential design compromises in the survivability and power output of the device. If this compromise is selected intelligently, such as through the creation of a separate objective function to balance the weighting of the collision rate and power output, then a 5.5% reduction in exergy output was sufficient to produce a 55% reduction in the collision rate. However, the annually-averaged collision rate is estimated to be ~1.34 collisions/min for the optimal design. This is prohibitively high; however, given that the collision-rate based study conducted in Section 4.3 does not provide a holistic representation of what device survivability, there is insufficient data to develop a survivability-focused active control strategy in the current study.

Following the completion of the optimization algorithm, the optimal design was carried forward to the creation of a power matrix for the passively controlled AOE WEC. The power matrix data was used to validate the annual exergy prediction provided through the optimization, while simultaneously providing comprehensive performance data for the AOE WEC. Using this data, at the Amphitrite Bank location the device was found to produce 29.37 kW annually, with a total power conversion efficiency of 3.5%. While the efficiency was fairly consistent in moderate and high energy sea-states, it dropped in sea-states with significant wave heights of 0.75 m – 1.75 m. As a result, despite improvements provided by the optimization algorithm there is still disparate power production in low energy sea-states. As a result of this discrepancy, the improvement of power production in low energy sea-states is labelled as a primary objective for the implementation of active control.

Chapter 5. Development of Active Controller

Following the implementation of power-maximizing passive control, an active control strategy is now developed for the AOE WEC. The active controller acts as an additional layer of control in order to improve the continuity of power production in low energy sea-states; this objective is motivated by the nature of the power matrix for the passively controlled system (Section 4.4.1). In particular, the AOE WEC performed well in moderate sea-states, while providing consistent, yet limited, output in low energy wave conditions. As described in Table 4.9, seas with significant wave heights between 0.75 m – 1.75 m encompass 55.93% of the hours on average throughout the year, but only account for 13.74% of the energy production. Furthermore, sea-states with wave heights of 0.75 m produced no energy. Consequently, while the optimization procedure has made gains in the continuity of power production, there is still a substantial performance gap between low and moderate wave conditions. This provides strong motivation for the implementation of an active control strategy, focused on improving the performance of the device in low energy sea-states. For the purpose of active control implementation, low-energy sea-states are defined as sea-states with wave heights of 1.75 m or lower.

Towards this goal, this Chapter first reviews the existing literature to identify viable control techniques for the AOE WEC. Underlying principles from a subset of existing techniques are then coalesced into a novel control strategy that is specific to the unique constraints of the AOE WEC – namely that the PTO reaction force can only be adjusted indirectly, and in discrete increments, through control of the valves and accumulator tanks. The performance of the actively controlled system is then compared to the passively controlled system in order to assess the benefit of active control implementation in the context of annual energy conversion.

5.1 Review of Active Control Implementation for Wave Energy Converters

Wave energy control has been studied fairly extensively, with numerous control strategies having been developed for achieving a variety of different objectives; these include WEC power production performance, WEC array cooperation, WEC survivability, or power quality improvements downstream in the power conversion delivery pathway. For brevity, this literature review focuses on strategies most relevant to the increase of power production, which more closely aligns with the present work. For a review of strategies pertaining to other control objectives, one can refer to a series of existing articles [66] [67] [68] [69] [70].

Regarding power production, the broad types of control techniques seen in literature are the following [66]: phase control, latching control, proportional integral (PI), optimal, and predictive control. Since the PI control strategy has only been applied to regular wave conditions [66], it is not considered in detail in this Chapter. The remaining four major control types each encompass a wide range of particular implementation techniques. These include widely adopted, yet sub-optimal, techniques such as velocity proportional control [71] [72], as well as implementations that are specific to particular converter or PTO dynamics. Here select implementations that are applicable to pneumatic or accumulator-based wave energy converters are addressed. These control techniques were developed with similar physical constraints to the AOE WEC in mind, and thus have the greatest potential for implementation in the AOE device.

5.1.1 Theoretically Optimal Control

Theoretically optimal control strategies are developed using known optimal phase and amplitude motion conditions [68] [11] [67]. For optimal power capture, the velocity of the WEC must be in phase with the excitation force (phase condition). Furthermore, the amplitude of motion must be such that there is maximum destructive interference between the incoming wave and the wave radiated from the WEC (amplitude condition). These two conditions may be expressed as a single optimal condition through the use of a complex mechanical impedance. Making use of this result, complex conjugate control was developed as a means of applying an optimal PTO force through continual matching of the PTO impedance with the complex conjugate of the internal impedance [67]. If the PTO force is assumed to be represented by a mass-spring damper, then complex-conjugate control can be used to dictate the optimal PTO characteristics (mass, spring and damping coefficients) for maximizing power capture. These PTO characteristics are then varied in real-time to produce the optimal PTO force.

An analytical solution for the optimal PTO mass-spring damper coefficients of an arbitrary two-body WEC in regular waves is provided by Falnes [73]. As seen in these analytical results, the application of complex conjugate control requires bi-directional power flow, which is why it is sometimes referred to as reactive control [11]. It is important to note that in practice, it is not possible for this strategy to be fully optimal as the strategy is non-causal [72] and velocities can become extremely high [69]. Non-causality requires knowledge of future states, which is not possible for practical control implementation; however, complex conjugate control has still seen significant attention in literature. In particular, numerous papers have studied both the implementation of idealized and causal approximations for complex conjugate control [72] [74] [75].

However, the application of complex conjugate control is not the only method of implementing optimal phase and amplitude control. Falnes [67] provides an analogous optimal condition for OWC devices, which is defined as phase matching of the dynamic air pressure and excitation volume flow. Additional forms for implementing optimal control also exist elsewhere in literature, such as optimal stochastic control presented by Nielson et al [71]; however, this control strategy also suffers from non-causality. Furthermore, known optimal phase conditions have prompted additional power maximizing control objectives such as the direct trajectory control of the velocity [76] [77], in which the desired set point of the controller is defined with the optimal phase condition.

5.1.2 Sub-Optimal Control

Given the difficulties in implementing optimal phase and amplitude PTO force control, a substantial body of research has developed on the implementation of sub-optimal, yet realistic, PTO control strategies. Perhaps the most widely implemented of these strategies is latching control. Latching is a form of phase control that operates by selectively holding the WEC in place ('latching') or releasing the converter at opportune times in the wave cycle. In doing so, the velocity of the WEC is placed more closely in phase with the waves, which is necessary in order to maximize power absorption. A primary advantage of latching control is that no reactive power is needed, as the WEC is latched at the point of zero velocity and hence no work is applied by the actuators that complete the latching motion. In regular waves, analytically determined optimal timing of the WEC latch and subsequent release is given by Babarit et al [78]. However, consensus has not been reached on the point of optimal release in irregular waves as no analytically determined optimal timing condition exists. In addition to the study of the timing of latching release, numerous papers exist on the study of latching control in a variety of WEC devices, such as OWC devices [79] and single degree of freedom point absorbers [78].

In order to implement constraints in the control objective, several studies have assessed the implementation of model predictive control (MPC). MPC solves an optimization problem at each time step that can incorporate different design constraints. The constrained problem yields an optimal PTO force at each time step. In order to apply MPC to actual mechanical systems, a fast optimization algorithm is required. As a result, the optimization problem is typically formulated as a convex quadratic problem, so as to make use of efficient optimization algorithms [80] [81]; a consequence of doing so is that the model must be linearized [82]. Despite these limitations, MPC been studied extensively in wave energy literature, such as for a generic heaving buoy [83] [82] [83] or specific converters such as the Archimedes Wave Swing [76]. In order to avoid having to linearize the WEC model, Li et al examined a dynamic programming implementation [81]. While a non-linear WEC model was used, the control signal required to achieve the optimal condition was a bang-bang type of signal [81]. This restricts the nature of the control signal that may be used to formulate the MPC control problem.

5.1.3 Control for Pneumatic or Accumulator-based WEC Designs

In addition to the general control techniques detailed above, several strategies have been designed specifically for particular WECs with characteristics that resemble the AOE device. The first of these strategies is valve based air-flow control for OWC WECs, which was developed by Falcao and Justino [84]. The function of the strategy is to reduce aerodynamic stall losses in the turbine blades using either a by-pass or throttle valve. Both valve types are controlled in order to adjust the mass-flow rate, for which their usage is designed for systems that are over-damped and under-damped, respectively. Babarit et al [85] studied two control strategies for hydraulic accumulator-based systems. The first provides pseudo-continuous control through the use of multiple bypass valves, coupled with several variable pressure accumulator tanks. Control is then used to cycle flow through these tanks during the wave cycle, in order to provide a variable force. Declutching control [85] is proposed as a simpler implementation of the above, which uses the Pontryagin principle to state that the optimal force is either a maximum or minimum value. As a result, flow is either directed to a low or high pressure accumulator, which provides a damping or latching force, respectively. Valve based latching has also been formulated as a form of "pseudo-latching" in the work of Falcao [86]. In this study, the latching force needed to hold the body motionless is dependent on the use of a hydraulic cylinder at sufficient pressure. Falcao [87] studied the development of control for a hydraulic PTO with two gas accumulator tanks; the strategy controlled the flow to the hydraulic motor as a function of the pressure difference across the two tanks.

5.2 Selection of an Active Controller for the AOE WEC

From the review of existing WEC controllers a promising option was identified for implementation in the AOE WEC: valve based control as described by Falcao and Justino [84]. Focus was placed on this control technique in particular, as it matched the unique constraints placed on nature of control implementation in the AOE WEC. This was in contrast to much of the original scope of control techniques, for which many techniques were identified that were reliant on idealized mass-spring damper PTO geometries (optimal control), additional controllable geometries (latching), or an approximately linear system (MPC). Others, while including several of the same PTO geometries, rely on the incompressible nature of hydraulic flow for PTO force modulation, and hence are not applicable to the AOE WEC which uses a compressible working fluid. These techniques include declutching [85], pseudo-continuous control [85], pseudo-latching [86], and pressure-based flow rate control [87].

The valve control seen in Falcao and Justino [84] was applied to improve efficiency in the air turbine of an OWC WEC. While their results are not directly applicable to the AOE WEC, this methodology aligns strongly with the objective of control in the AOE device. In contrast to much of the control literature, there are several issues associated with attempting to achieve a desired PTO force in the AOE WEC:

1. The compressibility of air makes it difficult to dictate the PTO force through the use of variable pressure accumulator tanks, especially in low energy sea-states
2. The use of valve based control only provides discrete control actions, which prevents continuous control.
3. The nonlinear nature of flow in the AOE WEC complicates the prediction of how a particular control action (e.g. valve opening) will subsequently alter the PTO force, particularly in downstream devices.

As a result, the AOE WEC does not lend itself to the generation of a targeted PTO force. Consequently, as with the work by Falcao and Justino [84], focus was shifted to improving the efficiency of a particular component directly. In the case of the AOE WEC, focus was placed on improving the energy absorption of the piston cylinder, particularly within low energy sea-states. This strategy is strongly tied to the nature of the AOE WEC, and as such does not have any precedent in literature.

5.3 Active Control Strategy

The absorption of energy in the AOE WEC is strongly correlated to the continual throughput of air; this is driven by the open system nature of the energy conversion process. During the piston upstroke, as air is compressed within the upper piston chamber, a pressure differential is produced between the upper (ch. 2) and lower (ch. 1) piston chambers. However, during the piston downstroke, as the upper chamber expands, the opposite is true: the pressure differential across the two piston chambers performs work back on the piston. This flow of reactive power decreases the total absorbed energy over the course of the wave cycle. In particular, if the air within both piston chambers is returned to the same state that it was prior to compression, no energy was absorbed. Consequently, the absorption of energy requires continuous air throughput; namely, a flow of compressed air onwards to the subsequent accumulator tank, coupled with the simultaneous replacement of this air from the ambient environment.

However, in low energy sea-states (defined as those with wave heights below 1.75 m), the majority of waves do not contain sufficient power to compress the air within the upper piston chamber to the tank pressure. Therefore, most wave cycles lead to a net zero absorption of energy. To prevent this from occurring, a strategy was developed that selectively pressurizes and de-pressurizes the piston at opportune times through the recirculation of air. Specifically, when the pressure in the piston is not at a sufficient pressure to pass air onto the next device via the throughput tank, it is instead sent to a recirculation tank before it has an opportunity to do work (e.g. supply reactive power) to the piston. The temporary shift of air mass to the recirculation tank lowers the quantity of air within the upper piston chamber, which allows the piston chamber to reach a lower pressure on the subsequent expansion stroke (downstroke). As a result, there is an increased likelihood of air flowing from the lower to the upper piston chamber during the piston downstroke. Following the transfer of air between piston chambers, the initial air volume is re-injected from the recirculation tank back into the upper piston chamber. This increases the pressure of the upper chamber prior to the next compression stroke (upstroke), which in turn increases the likelihood that the chamber pressure will be sufficient to pass air onto the subsequent recirculation tank. Consequently, the recirculation-based control strategy increases the throughput of air in both piston chambers, which in turn increases the absorbed power. Fig. 5.1 provides a schematic of airflow in a single device under the influence of the active control strategy. It is important to note that while airflow is shown across each of the three valves within the device for clarity, airflow likely does not occur within all three valves during every wave cycle. As described above, the instances that airflow does not occur are the motivation for the developed control strategy.

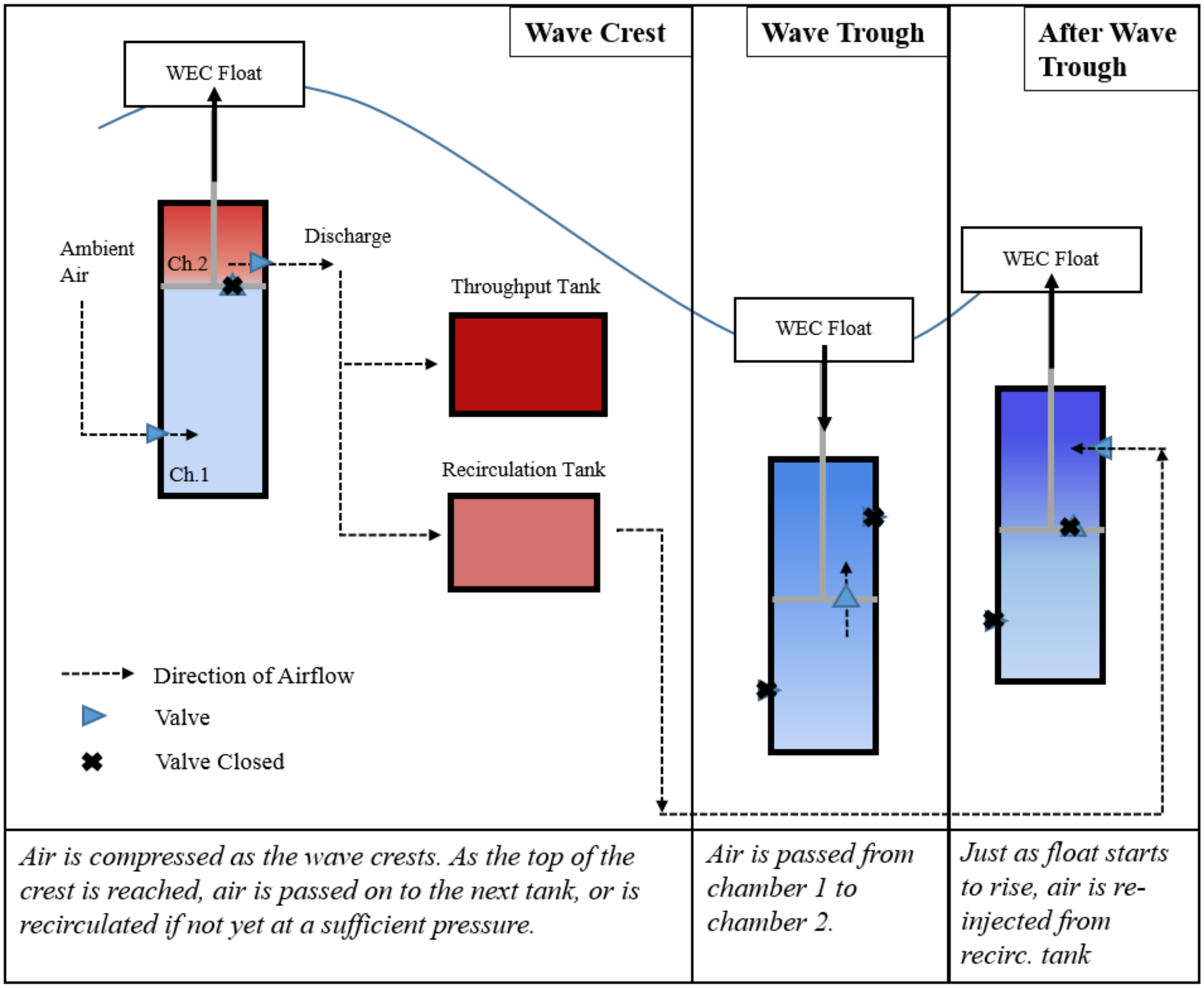

Figure 5.1: Schematic of airflow during a recirculation of the air mass in the upper piston chamber.

In order to implement this control strategy, the piston exit valve is changed to a two-way valve; this allows air to be re-injected into the upper piston chamber at the trough of the piston motion. While in theory it would be possible to re-inject air into the lower piston chamber instead, air is passed back to the upper chamber of the piston due to two factors:

1. The re-injection of air into the lower chamber would increase the chamber pressure; this which may prevent ambient air from being drawn into the lower chamber on the subsequent cycle.
2. Pumping air into the upper chamber allows pressure in this chamber to gradually build up over multiple cycles, which can occur even in the absence of additional flow from the

lower chamber if there is a net increase in the height of the float over the particular segment of wave motion.

Since recirculation of the upper chamber does not affect the nature of flow in the lower chamber, it is possible to recirculate air within the bottom chamber as well. Recirculation within the bottom chamber of the piston is shown in Fig. 5.2.

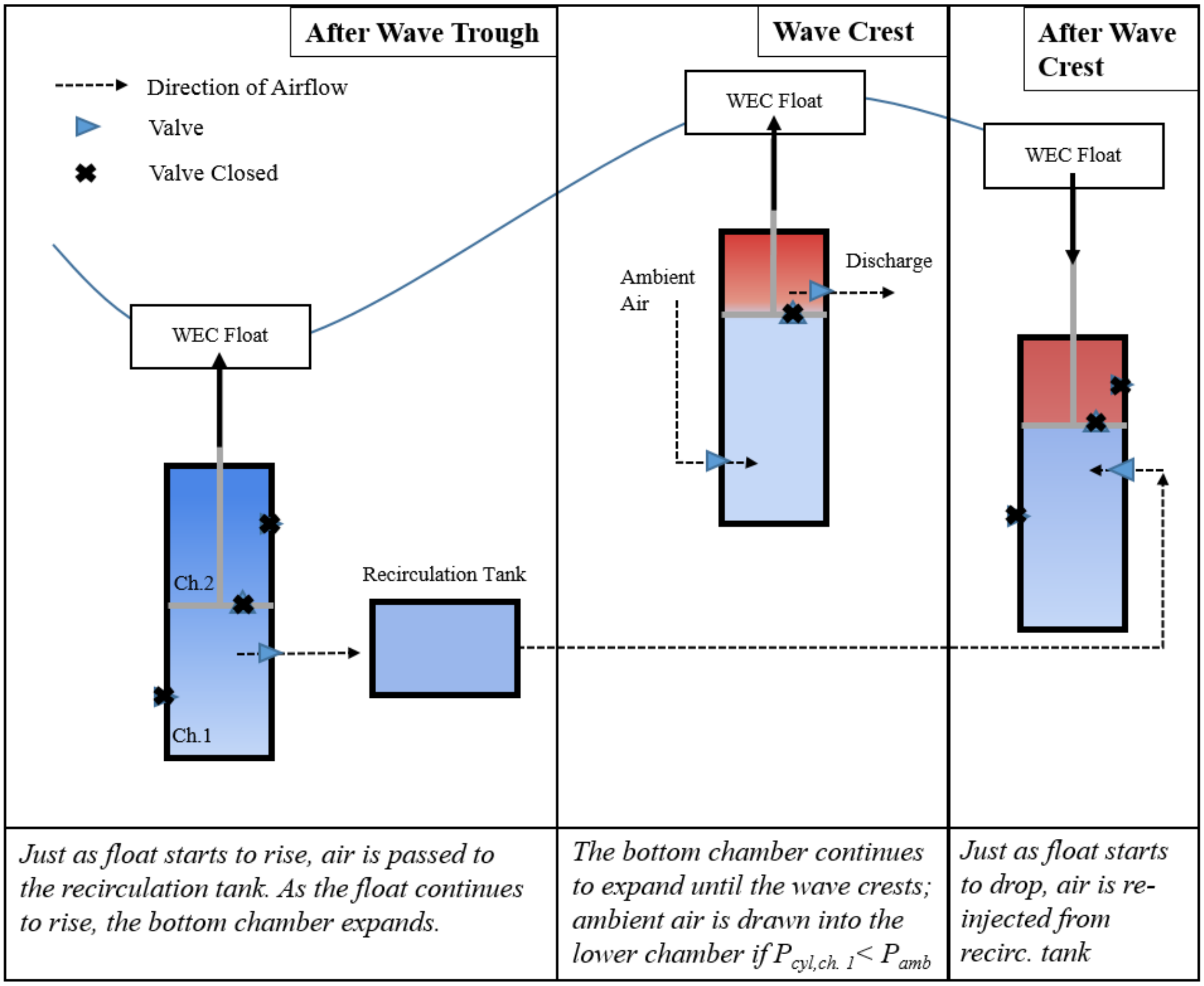

Just as float starts to rise, air is passed to the recirculation tank. As the float continues to rise, the bottom chamber expands.

The bottom chamber continues to expand until the wave crests; ambient air is drawn into the lower chamber if $P_{cyl,ch.\,1} < P_{amb}$

Just as float starts to drop, air is re-injected from recirc. tank

Figure 5.2: Schematic of airflow during a recirculation of the air mass in the lower piston chamber.

The temporary removal of air drops the pressure within the lower chamber of the piston, which increases the chance of atmospheric air flowing into the piston during the next expansion stroke (upstroke). Once ambient air is drawn into the lower chamber, air is re-injected from the recirculation tank back into the lower chamber. This increases the pressure of the lower chamber prior to the next compression stroke (downstroke), which in turn increases the likelihood that air will be at a sufficient pressure to flow between piston chambers prior to the next wave trough. Consequently, the lower chamber recirculation strategy further increases the likelihood of air flowing between chambers, as well as the likelihood of fresh ambient air flowing into the lower chamber, which is needed to produce useful power output. In order to implement recirculation in the lower piston chamber, an additional valve must be added that allows two-way flow to and from the lower chamber recirculation tank.

These two methods of recirculation can be used independently or in combination. In the following sections, the sequence of valve operations for the different combinations of air recirculation in the system are described. Each combination is a “controller” – a new WEC subsystem that operates in real-time to improve the mass of air that is being passed through the system. For each controller presented, the incremental performance achieved through recirculation is assessed. In order to assess the controllers in detail, they are applied solely to the first device of the three that comprise the complete AOE WEC system; since the resulting gains in the continuity of air throughput will carry through multiple devices, it is expected that the first device will have the strongest impact on airflow through the device chain.

5.4 Controller Implementation

In order to implement the recirculation control strategy, increased attention was placed on improving the model’s representation of the valve timing as well as modelling the flow of air through the two way valves that connect the recirculation tanks to the chambers of the piston cylinder. The changes made to these models are addressed in the following subsections.

5.4.1 Valve Layout and Piping

Each controller considered below introduces significant complexity into how the valves channel airflow. For example, the piston outflow valve must allow airflow to multiple destinations, i.e. the throughput and recirculation tank, as well as in multiple directions. In order to account for resulting complexities in the physical system, several assumptions/simplifications are applied. For one, while a more complex piping system would be required to route air between the chambers and the new tanks, this piping is not resolved in the current model as the flow losses as a result of bends in piping are assumed to be small. Furthermore, as with the original valve model, air is assumed to flow instantaneously from each of the valves to the recirculation tanks, and vice versa, with no loss in pressure. Lastly, in order to account for the change in the valve dynamics needed for flow to/from the recirculation tanks, the valves are implemented as if they are two one-way valves, for which only one valve of the pair may be open at a particular time. This is to ensure that backflow is not considered, which would greatly increase the simulation complexity. Rather, the valve flow direction is determined using a control signal, which allows flow to the recirculation or throughput tank, or manually reverses the flow direction. In doing so, the control signal may over-ride favourable pressure gradients that temporarily exist between certain chambers. This is in contrast to the existing valve control mechanism, that allows flow/shuts the valve solely on a pressure basis. To implement the control strategy in both piston chambers, two separate control signals are needed: one for each chamber.

5.4.2 Valve Timing: Upper Chamber Recirculation

The flow direction through the upper chamber exit valve is a function of the upper chamber control signal, R_2, which is a positive integer used to define the valve state; the ‘2’ references the dual definition of the upper cylinder chamber as ch. 2. The control-determined flow direction merely allows flow to a particular tank; however, flow will not occur unless a favourable pressure differential exists. The valve flow direction as a function of R_2 is shown in Eq. 5.1.

$$Upper\ Chamber\ Valve\ Flow\ Direction = \begin{cases} if\ R_2 = 2, Throughput\ Tank \\ if\ R_2 = 1, Recirculation\ Tank \\ if\ R_2 = 0, Flow\ Re - entry \end{cases} \tag{5.1}$$

The value of the control signal, R_2, is determined as a function of the pressure within the piston, as well as the piston motion. The value of the control signal is given as a flowchart in Fig. 5.3.

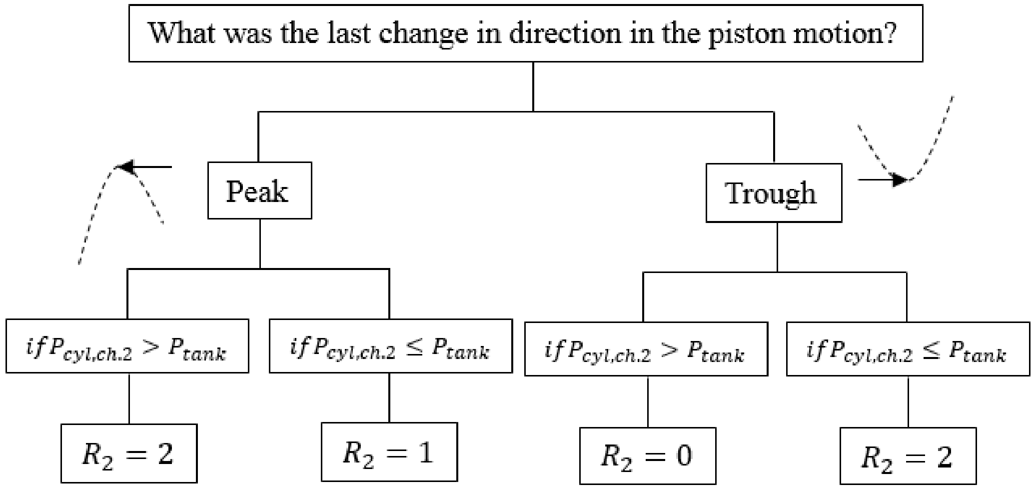

Figure 5.3: Flowchart used to determine value of control signal R_2.

A trough is the lowest local point in the piston motion, while a peak corresponds to the highest local point in the piston motion. The trough is ideal for flow re-entry into the upper piston chamber as the pressure has reached the lowest value within the wave cycle. As such, there is the greatest potential for air to flow from the recirculation tank to the upper chamber. Since air was sent to the recirculation tank at the peak pressure in the last wave cycle, air will always be able to re-enter the chamber at the trough. Furthermore, the trough marks the last point at which air can flow from the lower to the upper piston chamber, which ensures recirculation does not inhibit normal flow operation.

5.4.3 Valve Timing: Lower Chamber Recirculation

For the lower piston chamber, the flow direction through the tank recirculation chamber is given in Eq. 5.2.

$$Lower\ Chamber\ Valve\ Flow\ Direction = \begin{cases} if\ R_1 = 2, Piston\ Ch.2 \\ if\ R_1 = 1, Recirculation\ Tank \\ if\ R_1 = 0, Flow\ Re-entry \end{cases} \quad (5.2)$$

The value of the lower chamber control signal, R_1, is given as a flowchart in Fig. 5.4.

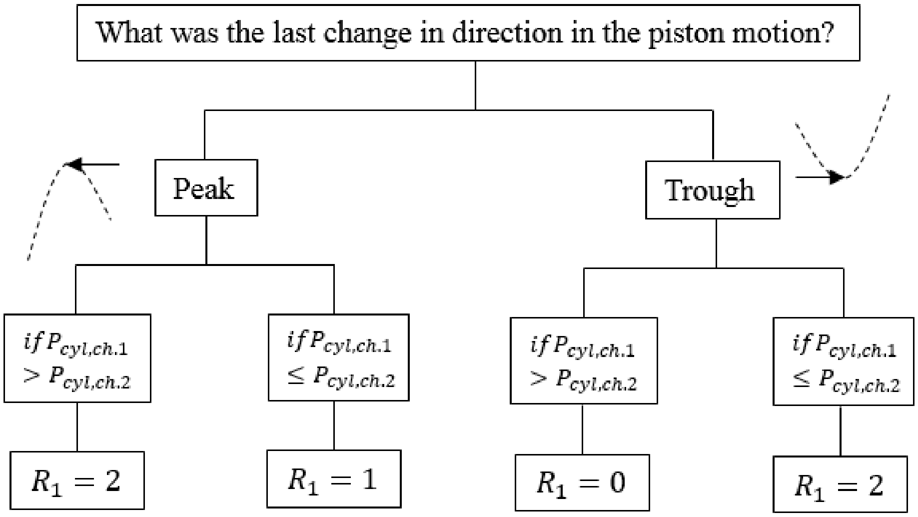

Figure 5.4: Flowchart used to determine value of control signal R_1.

5.4.4 Valve Timing: Peak and Trough Detection

As can be seen with Fig. 5.3 and Fig. 5.4, the determination of the peaks and troughs in the piston motion is critical for the timing of recirculation events, as these points in the motion trigger changes in the value of the recirculation variable. Consequently, care was taken to select these peaks and troughs accurately. The determination of a peak or trough is governed by the flowchart in Fig. 5.5.

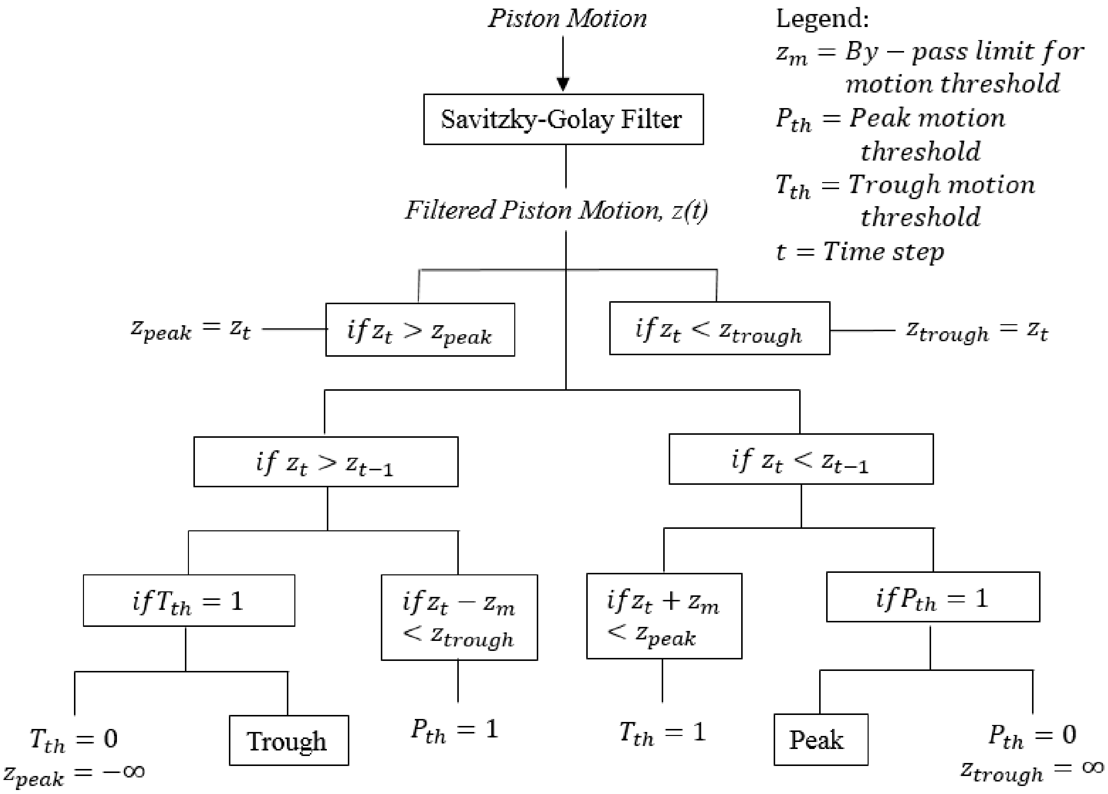

Figure 5.5: Flowchart used to determine whether current motion constitutes a peak or trough.

As given in Section 2.2, the piston motion is determined as the relative heave motion between the spar and float of the WEC. However, in order to only register significant peaks and troughs, two “filters” were placed on the original piston motion signal:

1. Savitzky-Golay Filter
2. Motion Threshold

The Savitzy-Golay (SG) filter is applied to smooth the piston motion signal, after which a motion threshold is applied in order to ensure peaks/troughs of a sufficient size are registered. These filters are applied “on the fly,” such that peaks/troughs are identified in real time using the past and current piston motion signal. The SG filter is implemented using MATLAB’s *sgolay* function, while the motion threshold was applied directly in the Simulink model. To understand the need for these filters, a sample piston motion signal (taken from the first device) is given in Fig. 5.6, as well as a sample filtered signal.

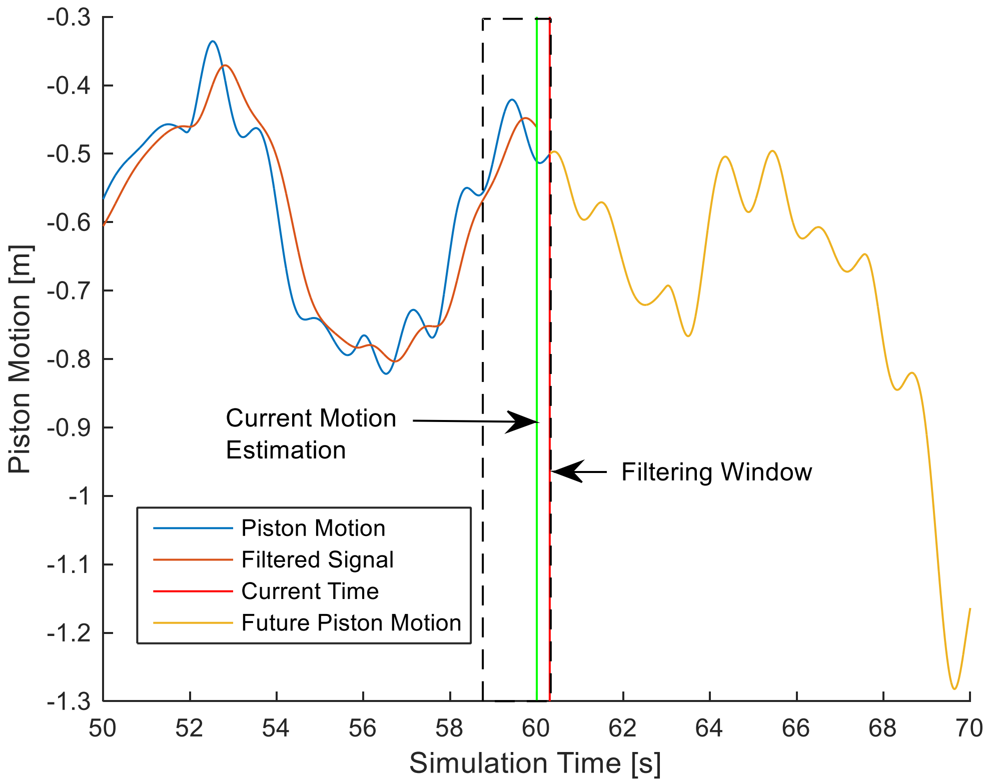

Figure 5.6: Comparison of raw piston motion and filtered signal in H_s *=1.75 m and* T_e *= 8.5 s.*

Within the piston motion signal, there are local peaks and troughs as well as large-scale (aggregate) peaks and troughs. In the majority of sea-states, large-scale peaks are the sole instances in which air is passed to the next device, as the energy contained in a local peak is not sufficient to compress the air beyond that of the subsequent tank. As a result, it is critical for these large-scale motions to be considered when recirculating air; otherwise, the recirculation strategy would remove air before it has the opportunity to reach the final peak of the motion. However, these peaks needed to be identified nearly instantaneously in order to apply time-sensitive control signals as close to true peaks/troughs as possible. Therefore, the SG filter and threshold limit were applied via a receding horizon filtering window. Since only past data was used to track real-time changes in the filtered signal (i.e. no predictive techniques were used), the filtered signal more accurately captured peaks/troughs if a slight delay was introduced in the filtering process.

The Savitzky-Golay filter was applied in order to prevent premature opening/closing of the valve based on high-frequency fluctuations. The optimal set of SG filter parameters are given in Table 5.1; the motivation behind the selection of these parameters, as well as the reasoning behind the selection of the SG filter in particular, is given in Appendix A.

However, this filter alone is insufficient for processing the piston motion signal, as the act of recirculating air introduces further high frequency oscillations in the piston motion. Every time air is injected back into the piston there is a slight oscillation in the motion. Similar to local oscillations in the motion as a result of minute changes in the wave height, these signals must be removed if the aggregate peaks and troughs in the piston motion are to be used effectively by the recirculation control strategy. However, due to the high frequency nature of these oscillations, the delay induced by the SG filter prevents the filter from removing these motions. Consequently, a motion threshold must be applied to the real-time signal in order to prevent recirculation-induced micro peaks from affecting the timing of subsequent recirculation events. The motion threshold ensures that a certain distance has been exceeded since the last trough/peak event. Since the motion threshold is not applied via a filter, it does not produce a delay, and as such is able to identify these high frequency motions. The micro-fluctuations produced by the recirculation of air are shown in a close up in Fig. 5.7. Fig. 5.7b shows a signal to which a motion threshold has been applied, and as a result does not include these fluctuations.

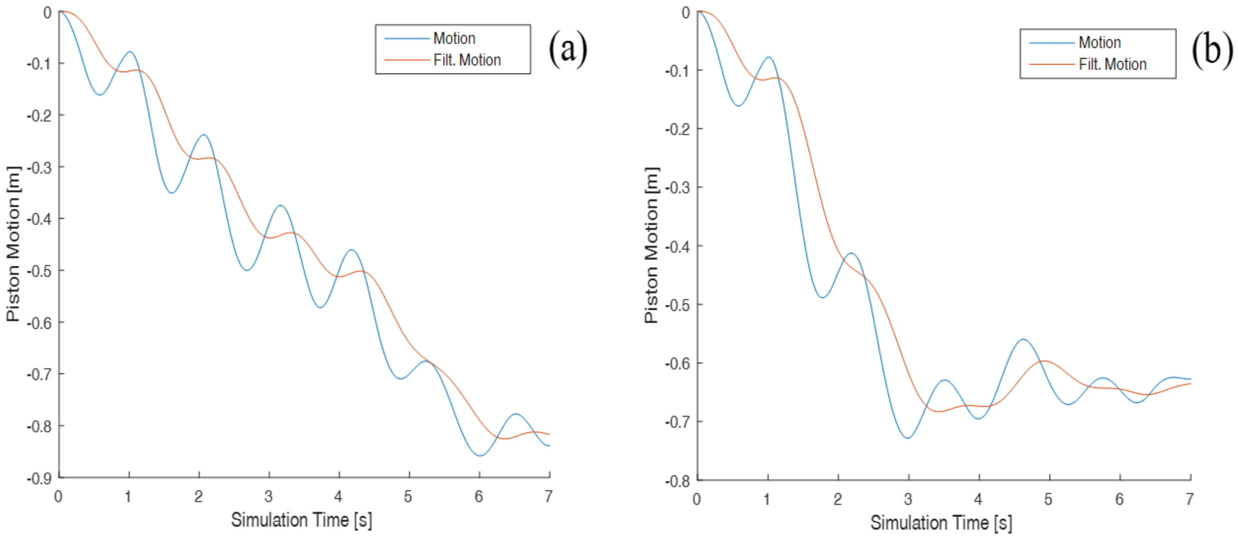

Figure 5.7: Comparison between (a) piston motion with no magnitude filter and (b) magnitude-filtered signal.

As can be seen in the filtered signal within Fig. 5.6, this change produces a fundamentally different piston motion. The selection of an optimal set of motion threshold filter parameters is given in Appendix A. Incorporating both the motion threshold and SG filter, the complete set of parameters for filtering the piston motion is given in Table 5.1.

Table 5.1: Parameters for filtering piston motion signal.

Savitzky – Golay Filter			**Motion Threshold**
Polynomial Order	**# of Points for Polynomial Fit**	**Delay**	z_m
2	801	0.3 s	0.005

With the selection of these filter parameters, the timing of the valves, given via the control signal decision trees in Fig. 5.3 and Fig. 5.4, is fully defined.

5.4.5 Valve Design

The valve control signals given in Section 5.4.2 and Section 5.4.3 define the particular downstream volume to which flow is being directed; as an example, that the flow through the piston outflow valve is going to the throughput tank (instead of a recirculation tank). In order to determine the mass flow rate between both volumes, Eq. 4.3 is applied; while this is identical to the flow rate given in Eq. 2.21 in Section 2.4.4, it is provided again here for clarity.

$$\dot{m} = \text{minimum}\begin{cases} \dot{m}_{\text{max}} \\ \dot{m}_{\text{control}} \\ \dot{m}_{\text{model}} \end{cases} \tag{5.3}$$

The model-based flow limits are extended to include flow to the recirculation tanks, yet the development of these limits are kept the same; a full set of mass flow limits is given in Appendix A. However, when a controller is added to the WEC the control-base flow limit $\dot{m}_{\text{control}}$ is adjusted, as well as the limit based on the state of the air, $\dot{m}_{\text{max}}$. In particular, the control signal is used to manually shut the valve when necessary. As a result, the control-based mass flow rate is restricted solely by the minimum of $\dot{m}_{max}$ and $\dot{m}_{model}$ when the control signal is positive, but is forced to zero when the control signal indicates flow in the opposite direction.

Furthermore, while the maximum mass flow rate used in the passively controlled system is sufficient to limit the magnitude of airflow through the valve to realistic levels, it does not account for the finite time over which the valve opens or shuts. Since the performance of the active control strategy is highly dependent on the timing of mass-flow events, it is critical to include this time dependence in the set of valve governing equations. The time dependent nature of the valve opening area is given in Eq. 5.4, which is based on a conically shaped valve such as that seen in Li et. al [88].

$$A_{open} = \frac{Ah}{H}(2 - \frac{h}{H}) \tag{5.4}$$

Where $\frac{h}{H}$ is the ratio of the current valve opening position to the maximum allowable opening. The valve opening rate is assumed to be linear with time, and reaches a maximum at 0.5s. This valve opening rate is the same as the valve response time used by Shin [89]. Therefore, the new maximum flow rate is given in Eq. 5.5.

$$\dot{m}_{max} = \begin{cases} \frac{A_{open}P2\gamma}{(\gamma - 1)RT}(\beta^{\frac{2}{\gamma}} - \beta^{\frac{\gamma+1}{\gamma}})^{0.5}, \beta > 0.5283 \\ \frac{0.0404A_{open}P}{T^{0.5}}, \beta \leq 0.5283 \end{cases} \tag{5.5}$$

5.4.6 Tank Design

The recirculation tanks are modelled using Eq. 2.15 - 2.17 for the pressure, mass, and temperature, respectively; these are the same set of equations used for the throughput tank. The recirculation tank is assumed to be of an equal volume to the initial throughput tank, as it was found that reducing the volume was severely detrimental to the performance of the control strategy. In particular, the recirculation tank volume must be significantly larger than either of the piston chambers, in order to maintain pressure in the tank as air is re-exhausted to the chamber; this increases the quantity of recirculated air. This effect on performance sets a minimum limit on the recirculation tank sizing that is, in principle, a violation of the initial design constraints set out by AOE. The throughput tank used in the optimization was a combination of the entire available volume of the 6 accumulator tanks; therefore, creating a recirculation tank of the same size exceeds the available tank volume. However, the change in the recirculation tank mass is far below the limit at which the changes would affect the operation of the AOE WEC. In particular, the combined mass of 6 accumulator tanks is only 314 kg, which is several orders of magnitude below the weight of the buoyancy tank (which has a mass of 93500 kg). As a result, the addition of more tanks will have virtually no impact on WEC motion. Therefore, if the control strategy produces substantial benefits, it is possible to add more accumulator tanks to the WEC design without significantly affecting the WEC hydrodynamics.

5.5 Active Control Strategy Results

The active control strategy is dependent on the number and configuration of the recirculation tanks that are included in the model. To assess the range of control possibilities that exist, four designs were assessed:

1. One recirculation tank, used to recirculate air in upper chamber of piston.
2. Two recirculation tanks, one of which is used to recirculate air in the upper chamber of the piston, while the other recirculates air in the lower chamber.
3. Three recirculation tanks, one of which is used to recirculate air in the upper chamber of the piston, while two are used to recirculate air in the lower chamber.
4. Four recirculation tanks, two of which are used to recirculate air in the upper chamber of the piston, while the two other tanks recirculate air in the lower chamber.

The addition of multiple recirculation tanks for the lower/upper chamber recirculation strategies is motivated by specific performance trends seen with controller #1 and #2. As such, the reasoning behind the inclusion of these tanks is described in Section 5.5.2 and Section 5.5.3, while the control laws defining the implementation of these tanks is described in Section 5.5.3 and Section 5.5.4. For now, it is sufficient to state the use of multiple recirculation tanks in the lower/upper chambers does not change the baseline operation of the strategies detailed in Section 5.3.

To scope the controller assessment exercise, the performance of each controller was determined via simulations at selected sea-states that are representative of the span of conditions within the low energy sea-state band defined at the beginning of the chapter (sea-states with significant wave heights below 1.75 m). These conditions are termed the ‘low’ (H_s = 1.25 m, T_e = 6.5 s) and ‘moderate’ (H_s = 1.75 m, T_e = 8.5 s) wave condition, as the moderate wave condition lies directly on the boundary of the active control target region. In both cases, controlled WEC system performance was compared to the performance of the baseline case: passive system defined in Table 4.4 of Section 4.1.2. The sea-states were simulated for 800 s, of which 200 s was allowed for the system to reach steady-state, with the following 10 min of simulation time used to track performance. Within the 200 s ‘warm-up’ period, the recirculation tanks were allowed to gather air. However, to ensure that the addition of multiple recirculation tanks did not artificially improve performance through the increased initial volume of air in the system, all recirculation tanks were started at atmospheric temperature and pressure at the start of the simulation. Therefore, all increases in air volume are physical, and not a result of bias in the simulation initial conditions. Following this performance assessment, the configuration that produced the greatest net benefit was carried forward to the creation of a new power matrix.

5.5.1 Single Recirculation Tank Controller

The first strategy makes use of a single recirculation tank, connected to the upper piston chamber of the cylinder. The performance of the control strategy in both the low and moderate sea-state is given in Table 5.2. In particular, the average flow exergy (power output) from each of the three devices, as well as the mass of air flowing between components of the first device, was tracked. Recall that the exergy of the air defines the useful power output, as a function of the mass-flow rate, temperature, and pressure of the air stream. The exergy of the outputted air was calculated using Eq. 3.6 and Eq. 3.7 of Section 3.2.2. In addition to reporting the exergy output, the mass flow between components is broken into two metrics: the total quantity of mass flow across the valve during the simulation, and the number of times that mass flow occurs across the valve, which is termed ‘mass flow events.’ Presenting both mass-flow and exergy data allows parallels in the contributions of the controller to air throughput, and subsequent device exergy improvements, to be drawn at multiple stages in the power conversion process. However, while exergy output is reported from all three devices, the mass-flow rate is restricted solely to the first device; this is driven by the fact that the controller exclusively acts on the first device, D_1^*.

Table 5.2: Performance comparison for passive and actively controlled system using 1 recirculation tank.

H_s = 1.25 m, T_e = 6.5 s				
Device	**Metric**	**Passive**	**Active, 1 Tank**	**Gain [%]**
D_1^*	Mass Flow, Inlet [kg]	22.30	25.48	14.3
	Mass Flow, Ch. 1 → Ch. 2 [kg]	21.95	25.22	14.9
	Mass Flow, Ch. 2 → Tank [kg]	21.77	22.84	4.9
	# of Mass Flow Events, Inlet	55	65	18.2
	# of Mass Flow Events, Ch. 1→Ch. 2	51	60	17.6
	# of Mass Flow Events, Ch. 2→Tank	47	45	-4.3
	Ave. Outlet Exergy, [kW]	1.7160	1.7800	3.7
D_2^*	Ave. Outlet Exergy, [kW]	1.9802	1.9959	0.8
D_3^*	Ave. Outlet Exergy [kW]	0.1088	0.1024	-5.9
H_s = 1.75 m, T_e = 8.5 s				
Device	**Metric**	**Passive**	**Active, 1 Tank**	**Gain [%]**
D_1^*	Mass Flow, Inlet [kg]	58.41	64.32	10.1
	Mass Flow, Ch. 1 → Ch. 2 [kg]	58.12	64.30	10.6
	Mass Flow, Ch. 2 → Tank [kg]	57.53	60.52	5.2
	# of Mass Flow Events, Inlet	49	72	46.9
	# of Mass Flow Events, Ch. 1→Ch. 2	60	70	16.7
	# of Mass Flow Events, Ch. 2→Tank	52	44	-15.4
	Ave. Outlet Exergy, [kW]	5.898	6.364	7.9
D_2^*	Ave. Outlet Exergy, [kW]	10.070	10.663	5.9
D_3^*	Ave. Outlet Exergy [kW]	12.680	13.259	4.6

NOTE: Ch. 1 refers to chamber 1 (lower chamber), Ch. 2 refers to chamber 2 (upper chamber)

As intended, this control strategy improved the mass flow through the first device, including both at the atmospheric inlet and from the upper chamber of the cylinder to the tank. However, there is a significant drop-off in the mass-flow improvement between the piston chambers and the flow onwards to the tank. This is an indication that in the first sea-state, ~10%

of the mass flow increase at the outlet of the piston cylinder may be attributed to filling the recirculation tank. As a result, ~90% of the airflow at the atmospheric inlet reached the throughput tank. Conversely, in the moderate sea-state ~5% of the mass flow increase at the outlet of the piston cylinder may be attributed to filling the recirculation tank, with , ~94% of the airflow at the atmospheric inlet reaching the throughput tank. In both cases, the remaining mass flow improvement led to a moderate improvement in the exergy out of the first device. For the low energy sea-state, this improvement was largely damped out by the time the compressed air exited the third device, as the 2nd and 3rd round of compression was still passively controlled. Consequently, throughput of air was still dependent on infrequent contributions from high energy waves. In the moderate sea-state, the exergy increases across all three devices, and the control strategy led to a small net positive improvement.

Since the 2nd and 3rd devices in the WEC chain are still passively controlled, it is not reasonable to expect to maintain the control-based performance improvement within latter devices. Therefore, to see a net improvement in the output from the 3rd device, it is necessary to further improve the mass flow of air exiting the first device. To do so, the recirculation strategy needs to further improve the number of mass flow events. When no air is drawn into the upper chamber of the piston following recirculation, the control strategy does not improve the likelihood of air passing onto the next tank, as the exact same quantity of air is re-injected prior to the next compression stroke. Consequently, while it is useful to improve the magnitude of mass flow per event (increasing the overall magnitude of airflow), the controller must primarily focus on improving the number of mass flow events, as this directly correlates to the ease of throughput of air. In particular, each time air is passed to the upper chamber prior to recirculation, there is a net increase in chamber pressure when air is re-injected to the chamber from the recirculation tank; this leads to an increased likelihood of air being transferred to the throughput tank on the subsequent compression cycle. As a result, in order to increase the number of mass flow events to the upper piston chamber, an additional recirculation tank was connected to the lower chamber.

5.5.2 Double Recirculation Tank Controller

The second strategy uses two recirculation tanks, one of which recirculates air in the upper chamber, while one recirculates air in the lower chamber. The recirculation of both chambers is conducted independently, using the upper and lower recirculation control signals and resulting valve timing described in Section 5.3. The performance of the control strategy in both the low and moderate sea-state is given in Table 5.3.

Table 5.3: Performance comparison for passive and actively controlled system using 1 upper chamber and 1 lower chamber recirculation tank.

H_s = 1.25 m, T_e = 6.5 s				
Device	**Metric**	**Passive**	**Active, 2 Tanks**	**Gain [%]**
D_1^*	Mass Flow, Inlet [kg]	22.30	27.29	22.4
	Mass Flow, Ch. 1 → Ch. 2 [kg]	21.95	56.25	156.3
	Mass Flow, Ch. 2 → Tank [kg]	21.77	25.02	14.9
	# of Mass Flow Events, Inlet	55	65	18.2
	# of Mass Flow Events, Ch. 1→Ch. 2	51	208	307.8
	# of Mass Flow Events, Ch. 2→Tank	47	45	-4.3
	Ave. Outlet Exergy, [kW]	1.7160	2.0800	21.2
D_2^*	Ave. Outlet Exergy, [kW]	1.9802	2.1652	9.3
D_3^*	Ave. Outlet Exergy [kW]	0.1088	0.1761	61.9
H_s = 1.75 m, T_e = 8.5 s				
Device	**Metric**	**Passive**	**Active, 2 Tanks**	**Gain [%]**
D_1^*	Mass Flow, Inlet [kg]	58.41	67.22	15.1
	Mass Flow, Ch. 1 → Ch. 2 [kg]	58.12	96.50	66.0
	Mass Flow, Ch. 2 → Tank [kg]	57.53	63.37	10.2
	# of Mass Flow Events, Inlet	49	61	24.5
	# of Mass Flow Events, Ch. 1→Ch. 2	60	191	218.3
	# of Mass Flow Events, Ch. 2→Tank	52	52	0
	Ave. Outlet Exergy, [kW]	5.898	7.0978	20.3
D_2^*	Ave. Outlet Exergy, [kW]	10.070	10.973	9.0
D_3^*	Ave. Outlet Exergy [kW]	12.680	13.511	6.6

NOTE: Ch. 1 refers to chamber 1 (lower chamber), Ch. 2 refers to chamber 2 (upper chamber)

When recirculating air within both the upper and lower piston chamber, there is a significant increase in both the mass-flow from the lower to the upper cylinder chamber and onwards to the subsequent tank. This is due to the large increase in mass-flow between the lower and upper chambers of the cylinder, which ensures that air can flow more readily from the inlet to the upper piston chamber. As a result, there is an improvement of over 20% in the exergy being delivered by the first device when compared to baseline operation. While this improvement continues to be damped in the low energy sea-state, the improvement over the base case is significant. Furthermore, the improvement in the moderate sea-state is larger than what is seen with a single recirculation tank. While the number of mass flow events at the atmospheric inlet and onwards to the throughput tank has remained the same or slightly increased, there is a substantial increase in mass flow events from the lower to the upper piston chambers. These events include flow to both recirculation tanks, which accounts for part of the increase. However, this is also an indication that there is increased airflow to the upper piston chamber. To further improve air throughput, and consequently exergy output, it is necessary to increase the number of inlet flow events. As described in Section 5.5.1, the number of mass-flow events is a direct determinant of the number of cases in which recirculation produces a net positive change in pressure. Currently, the recirculation of air in the lower chamber produces a substantial increase in the inlet flow of atmospheric air; however, since the AOE WEC is an open system, increases in the outflow of air must be simultaneously matched with increases in mass-flow at the atmospheric inlet.

5.5.3 Triple Recirculation Tank Controller

The three tank configuration makes use of one recirculation tank for the upper piston chamber, and two tanks in the bottom chamber. The operation of the lower recirculation tanks is still the same as what is illustrated in Fig. 5.2; however, the two recirculation tanks in the lower chamber are cascaded together, so as to draw air in sequence on every compression cycle. At the trough of the piston motion, if air is not at a sufficient pressure to flow to the upper piston chamber, it is dumped instead to the two recirculation tanks. At first, the highest pressure recirculation tank draws air until the pressure within the tank and piston chamber are equal, followed by the second tank. Similarly, at the peak of piston motion, air within the lower pressure tank is re-inputted into the lower piston chamber until the pressures within the tank and chamber are equalized; this is followed immediately by airflow from the highest pressure tank. In doing so, a greater quantity of air is drawn from the lower chamber prior to expansion, which increases the likelihood of air being drawn into the piston from the atmosphere, while subsequently re-dumping air back to the piston chamber in a manner so as to minimize losses. While a greater quantity of air is retained in both recirculation tanks than what would occur with only a single recirculation event, the increase in fresh air entering the piston is expected to offset any losses. Prior to detailing the results of the strategy, the operation of the control signals within the lower chamber is re-defined. First, the flow direction within the lower piston chamber is redefined with Eq. 5.6.

$$Lower\ Chamber\ Valve\ Flow\ Dir. = \begin{cases} if\ R_1 = 4, Piston\ Ch.2 \\ if\ R_1 = 3, Recirculation\ Tank\ 2 \\ if\ R_1 = 2, Recirculation\ Tank\ 1 \\ if\ R_1 = 1, Flow\ Re-entry\ from\ RT_2 \\ if\ R_1 = 0, Flow\ Re-entry\ from\ RT_1 \end{cases} \tag{5.6}$$

The value of the lower chamber control signal, R_1, is also redefined according to Fig. 5.8.

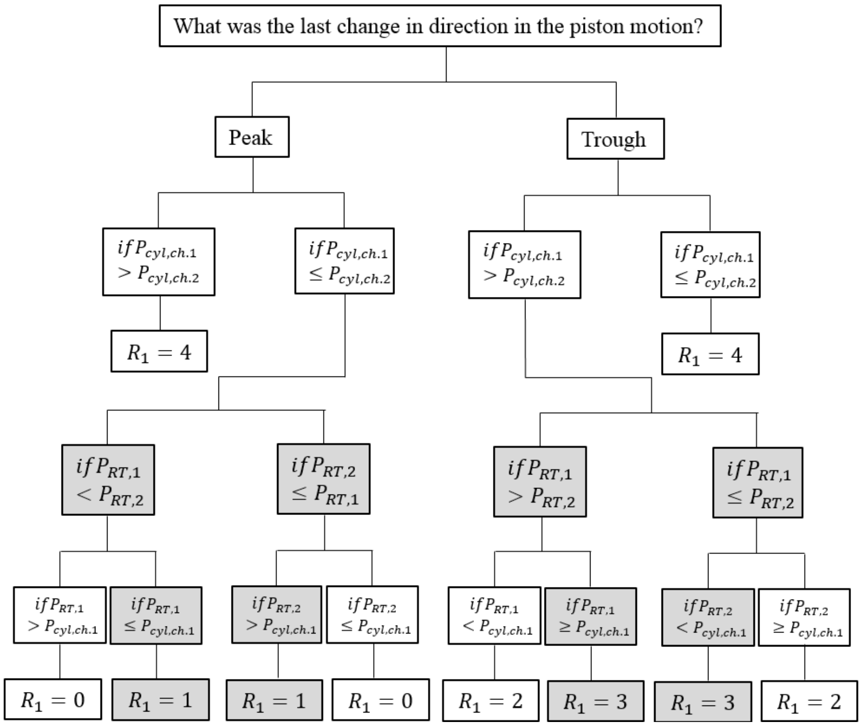

Figure 5.8: Flowchart used to determine value of control signal R_2 when two recirculation tanks are used for the lower piston chamber.

The control decisions that differ from those seen in Fig. 5.4 are highlighted. The performance of the control strategy in both the low and moderate sea-state is given in Table 5.4.

Table 5.4: Performance comparison for passive and actively controlled system using 1 upper chamber and 2 lower chamber recirculation tanks.

H_s = 1.25 m, T_e = 6.5 s				
Device	**Metric**	**Passive**	**Active, 3 Tanks**	**Gain [%]**
D_1^*	Mass Flow, Inlet [kg]	22.30	29.01	30.1
	Mass Flow, Ch. 1 → Ch. 2 [kg]	21.95	75.56	244.2
	Mass Flow, Ch. 2 → Tank [kg]	21.77	25.66	17.9
	# of Mass Flow Events, Inlet	55	66	20.0
	# of Mass Flow Events, Ch. 1→Ch. 2	51	267	423.5
	# of Mass Flow Events, Ch. 2→Tank	47	51	8.5
	Ave. Outlet Exergy, [kW]	1.7160	2.1118	23.1
D_2^*	Ave. Outlet Exergy, [kW]	1.9802	2.1701	9.6
D_3^*	Ave. Outlet Exergy [kW]	0.1088	0.2143	97.0
H_s = 1.75 m, T_e = 8.5 s				
Device	**Metric**	**Passive**	**Active, 3 Tanks**	**Gain [%]**
D_1^*	Mass Flow, Inlet [kg]	58.41	67.94	16.3
	Mass Flow, Ch. 1 → Ch. 2 [kg]	58.12	115.27	98.3
	Mass Flow, Ch. 2 → Tank [kg]	57.53	62.95	9.4
	# of Mass Flow Events, Inlet	49	78	59.2
	# of Mass Flow Events, Ch. 1→Ch. 2	60	246	310.0
	# of Mass Flow Events, Ch. 2→Tank	52	55	5.8
	Ave. Outlet Exergy, [kW]	5.898	6.9201	17.3
D_2^*	Ave. Outlet Exergy, [kW]	10.070	10.779	7.0
D_3^*	Ave. Outlet Exergy [kW]	12.680	13.290	4.8

NOTE: Ch. 1 refers to chamber 1 (lower chamber), Ch. 2 refers to chamber 2 (upper chamber)

Recirculation of air with three tanks provided a nearly universal improvement in both the quantity of mass-flow and number of mass-flow events across all valves. The only exception is in the moderate energy sea-state, for which there was a slight decrease in the quantity of mass-flow between the upper cylinder chamber and the throughput tank; this led to a small decrease in the total exergy output. However, this change was offset by a significant increase in exergy output in the low energy sea-state. This was likely driven by a significant increase in the quantity of mass-flow at the atmospheric inlet, which allowed a greater quantity of compressed air to be carried forward to the outlet of the third device. While this increase in compressed air flow only led to a moderate improvement in exergy in the first two devices, it is likely that these improvements were sufficient to trigger another major outflow event, which corresponded to a large discrete jump in exergy in the third device. However, since the improvement of power output in low energy sea-states is the objective of the control strategy, and the moderate sea-state lies on the boundary of the target region, the net gain across both sea-states is sufficient to state that the three-tank strategy outperforms the two-tank case.

These improvements were achieved despite only slight increases in the number of mass flow events at the atmospheric inlet. As seen in Table 5.4, these improvements were instead driven with an increase in inlet mass flow per event, as was the case in the low energy sea-state. In order to see larger improvements in the exergy output, the number of inlet mass flow events must be further increased. In particular, improving the frequency with which air is drawn into the lower piston chamber ensures that the when air is re-injected into this chamber, the resultant pressure is higher than what would have been achieved in the passive case. To do so, it is necessary to increase the frequency of throughput between the two piston chambers, through the use of two recirculation tanks acting on the upper piston chamber. The use of two recirculation tanks will drop the pressure in the upper piston chamber prior to expansion, which will increase the likelihood of air passing from the lower to the upper chamber. It is expected that this will have a cascading effect that will in turn increase the chance of air entering the piston on the subsequent wave cycle.

5.5.4 Quadruple Recirculation Tank Controller

The four tank configuration makes use of two recirculation tanks for both the lower and upper cylinder chamber; this is expected to further improve the quantity of airflow at the WEC inlet. The operation of the upper recirculation tanks is still the same as what is illustrated in Fig. 5.1; however, the two recirculation tanks in the upper chamber are cascaded together, so as to draw air in sequence on every compression cycle. At the peak of the piston motion, if air is not at a sufficient pressure to flow to the throughput air tank, it is dumped instead to the two recirculation tanks. At first, the highest pressure recirculation tank draws air until the pressure within the tank and piston chamber are equal, followed by the second tank. Similarly, at the trough of piston motion, air within the lower pressure tank is re-inputted into the upper piston chamber until the pressures within the tank and chamber are equalized; this is followed immediately by airflow from the highest pressure tank. Prior to detailing the results for this controller, the operation of the control signals within the lower chamber is re-defined. First, the flow direction within the lower piston chamber is redefined with Eq. 5.7.

$$Upper\ Chamber\ Valve\ Flow\ Dir. = \begin{cases} if\ R_2 = 4, Throughput\ Tank \\ if\ R_2 = 3, Reirculation\ Tank\ 2 \\ if\ R_2 = 2\ , Recirculation\ Tank\ 1 \\ if\ R_2 = 1, Flow\ Re - entry\ from\ RT_2 \\ if\ R_2 = 0, Flow\ Re - entry\ from\ RT_1 \end{cases} \tag{5.7}$$

The value of the upper chamber control signal, R_2, is redefined according to Fig. 5.9.

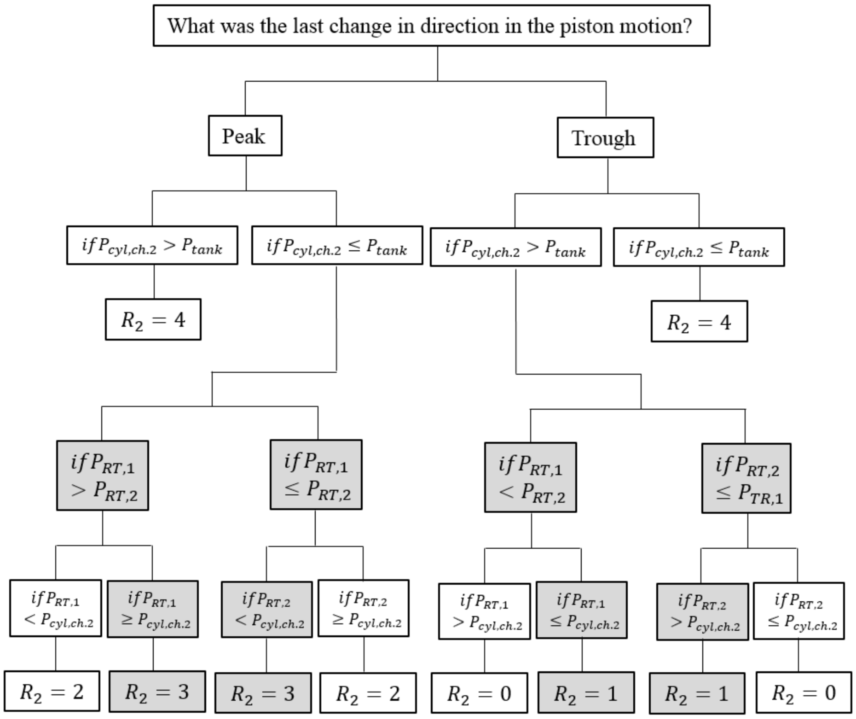

Figure 5.9: Flowchart used to determine value of control signal R_1 when two recirculation tanks are used for the upper piston chamber.

The control decisions that differ from those seen in Fig. 5.3 are highlighted. The performance of the control strategy in both the low and moderate sea-state is given in Table 5.5.

Table 5.5: Performance comparison for passive and actively controlled system using 2 upper chamber and 2 lower chamber recirculation tanks.

H_s = 1.25 m, T_e = 6.5 s				
Device	**Metric**	**Passive**	**Active, 4 Tanks**	**Gain [%]**
D_1^*	Mass Flow, Inlet [kg]	22.30	31.26	40.2
	Mass Flow, Ch. 1 → Ch. 2 [kg]	21.95	75.89	245.7
	Mass Flow, Ch. 2 → Tank [kg]	21.77	25.84	18.7
	# of Mass Flow Events, Inlet	55	74	34.5
	# of Mass Flow Events, Ch. 1→Ch. 2	51	264	417.6
	# of Mass Flow Events, Ch. 2→Tank	47	45	-4.3
	Ave. Outlet Exergy, [kW]	1.7160	2.0691	20.6
D_2^*	Ave. Outlet Exergy, [kW]	1.9802	2.1261	7.4
D_3^*	Ave. Outlet Exergy [kW]	0.1088	0.1696	55.9
H_s = 1.75 m, T_e = 8.5 s				
Device	**Metric**	**Passive**	**Active, 4 Tanks**	**Gain [%]**
D_1^*	Mass Flow, Inlet [kg]	58.41	70.94	21.5
	Mass Flow, Ch. 1 → Ch. 2 [kg]	58.12	115.09	98.0
	Mass Flow, Ch. 2 → Tank [kg]	57.53	63.56	10.5
	# of Mass Flow Events, Inlet	49	76	55.1
	# of Mass Flow Events, Ch. 1→Ch. 2	60	246	310.0
	# of Mass Flow Events, Ch. 2→Tank	52	52	0.0
	Ave. Outlet Exergy, [kW]	5.898	6.7837	15.0
D_2^*	Ave. Outlet Exergy, [kW]	10.070	10.850	7.7
D_3^*	Ave. Outlet Exergy [kW]	12.680	13.355	5.3

NOTE: Ch. 1 refers to chamber 1 (lower chamber), Ch. 2 refers to chamber 2 (upper chamber)

As intended, recirculation using four tanks was successful in improving the quantity of mass flow events at the inlet. However, in doing so the exergy output in the low energy sea-state was decreased substantially, while there was only a slight improvement over the 3-tank controller in the moderate energy sea-state. A potential explanation for this change is that the pressure within the upper piston chamber drops as a result of recirculation to two tanks; as a result, when air is passed from the lower to the upper piston chamber it does so at a lower pressure than the other controllers. Consequently, the subsequent compression cycle does not lead to as high of a pressure in the upper piston pressure, thereby reducing the number of instances in which the subsequent tank pressure is exceeded. This is more apparent in low energy sea-states, for which the drop in pressure further reduces the relatively few number of waves with sufficient energy to sufficiently compress the air within the piston, while simultaneously decreasing the quantity of mass flow per event. This effect was not apparent in the recirculation of the lower piston chamber since air always enters the piston at the same pressure; therefore, it was not possible to further reduce the starting pressure of the piston chamber prior to compression. With this in mind, a comparison of the four controllers is presented, followed by the selection of the final control strategy.

5.5.5 Comparison and Selection of Active Controller

The exergy production from each of the three devices, as a function of control configuration, is given in Table 5.6; for clarity, the highest exergy output for each sea-state is italicized.

Table 5.6: Performance comparison for passive and actively controlled system using 4 recirculation tanks.

H_s = 1.25 m, T_e = 6.5 s			
Control Strategy	**Exergy, D_1^* [kW]**	**Exergy, D_2^* [kW]**	**Exergy, D_3^* [kW]**
No Control	1.7160	1.9802	0.1088
1 Tank	1.7800	1.9959	0.1024
2 Tanks	2.0800	2.1652	0.1761
3 Tanks	*2.1118*	*2.1701*	*0.2143*
4 Tanks	2.0691	2.1261	0.1696
H_s = 1.75 m, T_e = 8.5 s			
No Control	5.898	10.070	12.680
1 Tank	6.364	10.663	13.259
2 Tanks	*7.0978*	*10.973*	*13.511*
3 Tanks	6.9201	10.779	13.290
4 Tanks	6.7837	10.850	13.355

In the low energy sea-state, the three tank recirculation strategy outperforms the other strategies, while for the moderate energy sea-state the two-tank configuration performs the most strongly. It is expected that the reduction in performance with more recirculation tanks in the moderate sea-state is caused by two primary losses associated with recirculation. Namely, in certain waves the time dependence of air recirculation could potentially produce a net decrease in compression as the full quantity of air is not present at the start of the compression cycle. Furthermore, there may be cases in which peaks and troughs in the piston motion are misidentified, which creates a performance loss. In low energy sea-states, these detrimental effects are outweighed by the positive impacts of the strategy, however there will be diminishing returns in higher energy seas.

With this in mind, since the objective of the control strategy is to improve performance in low energy sea-states, and the moderate sea-state lies on the boundary of the target region, the three-tank strategy was selected for the development of the power matrix. The performance of this strategy was only slightly below that of the 2- and 4-tank configurations in the moderate sea-state, while achieving the highest performance in the low energy case. Furthermore, based on the above discussion it is expected that the benefits of more recirculation tanks should outweigh losses in low energy sea-states.

5.6 Power Matrix for Actively Controlled System, and Comparison to Passive System

The power matrix under the influence of active control is created using the same sea-states used for the passively controlled system, to provide a true comparison between the control strategies. The description of these sea-states is given in Section 4.4. In order to provide clarity in the comparison between the actively controlled WEC and the passive system, the comparison is provided directly within this section. Results are broken up into the following categories: power output and efficiency.

5.6.1 Power Output

The power matrix for the actively controlled AOE device is given in Fig. 5.10. As with the passively controlled system, the power is calculated using flow exergy, in order to provide an estimate of the total useful power output from the converter.

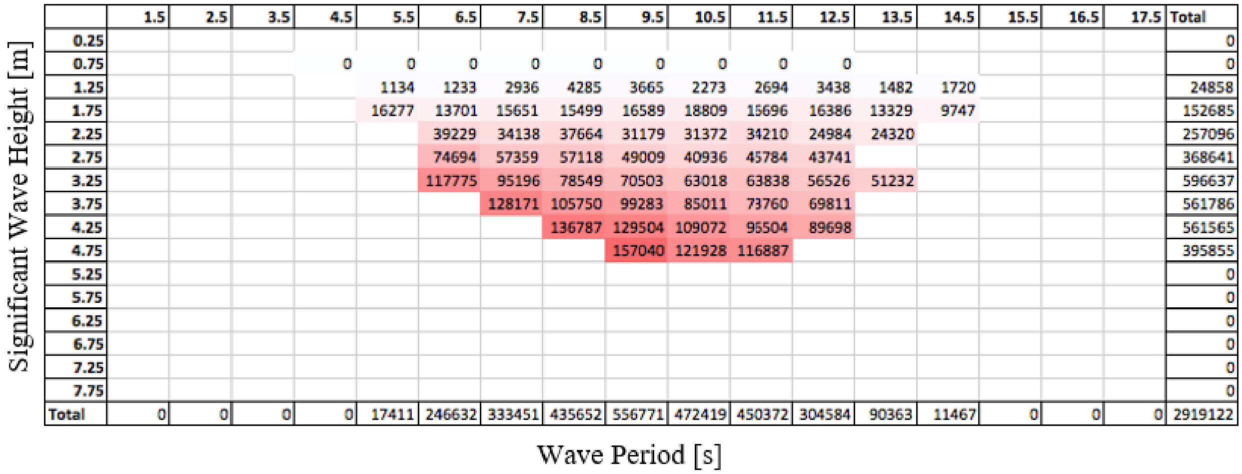

Significant Wave Height [m]

	1.5	2.5	3.5	4.5	5.5	6.5	7.5	8.5	9.5	10.5	11.5	12.5	13.5	14.5	15.5	16.5	17.5	Total
0.25																		0
0.75				0	0	0	0	0	0	0	0	0						0
1.25					1134	1233	2936	4285	3665	2273	2694	3438	1482	1720				24858
1.75					16277	13701	15651	15499	16589	18809	15696	16386	13329	9747				152685
2.25						39229	34138	37664	31179	31372	34210	24984	24320					257096
2.75						74694	57359	57118	49009	40936	45784	43741						368641
3.25						117775	95196	78549	70503	63018	63838	56526	51232					596637
3.75							128171	105750	99283	85011	73760	69811						561786
4.25								136787	129504	109072	95504	89698						561565
4.75									157040	121928	116887							395855
5.25																		0
5.75																		0
6.25																		0
6.75																		0
7.25																		0
7.75																		0
Total	0	0	0	0	17411	246632	333451	435652	556771	472419	450372	304584	90363	11467	0	0	0	2919122

Wave Period [s]

Figure 5.10: Power production [W] as a function of sea-state for actively controlled system.

As expected, the power production increases with significant wave height; for a particular height, the power production decreases with energy period. The maximum power production of 157.0 kW is reached in 4.75 m waves with an energy period of 9.5 s; conversely, the minimum of 0 kW is achieved in all sea-states of 0.75 m. For these low energy sea-states, power was produced from the first two devices in the cascade; however, despite the influence of the active control strategy the crack pressure in the third device was never reached. A comparison between the power production for the passive and actively controlled system is presented in Fig. 5.11.

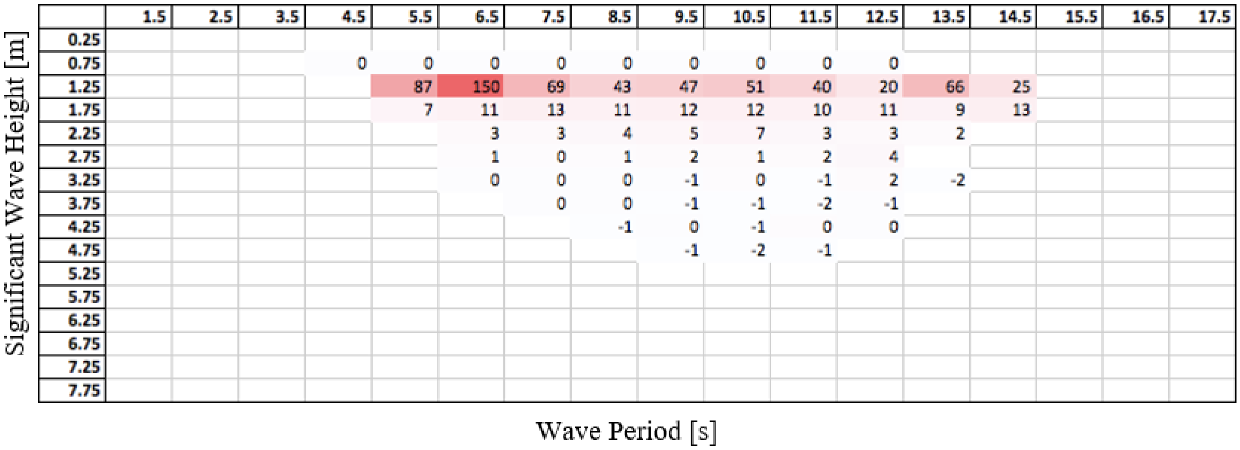

	1.5	2.5	3.5	4.5	5.5	6.5	7.5	8.5	9.5	10.5	11.5	12.5	13.5	14.5	15.5	16.5	17.5
0.25																	
0.75				0	0	0	0	0	0	0	0	0					
1.25					87	150	69	43	47	51	40	20	66	25			
1.75					7	11	13	11	12	12	10	11	9	13			
2.25						3	3	4	5	7	3	3	2				
2.75						1	0	1	2	1	2	4					
3.25						0	0	0	-1	0	-1	2	-2				
3.75							0	0	-1	-1	-2	-1					
4.25								-1	0	-1	0	0					
4.75									-1	-2	-1						
5.25																	
5.75																	
6.25																	
6.75																	
7.25																	
7.75																	

Figure 5.11: Improvement in power production [%] from passive to actively controlled system.

In low energy sea-states, particularly those with a wave height of 1.25 m, the exergy improvement was significant, with a range from 20% to a peak of 150%. Moderate improvements were also seen in sea-states with a wave height of 1.75 m, with gains reducing up until a wave height of 3.25 m. In sea-states above this wave height, the WEC performance was approximately constant, or slightly lower (1 – 2 %) below that of the passively controlled system. Therefore, the controller was successful in increasing power output in low energy sea-states with wave heights of 1.25 m or above, while not providing a significant decrease in performance in high energy seas. However, despite the percentage increase in power production in low energy sea-states, these conditions do not contribute as significantly to the annual power production as high-energy sea-states. In order to determine the relative contribution of each sea-state to the annual energy production under the influence of the active controller, the power matrix is overlaid with the hours of occurrence for the Amphitrite Bank location, as given in Fig. 5.12.

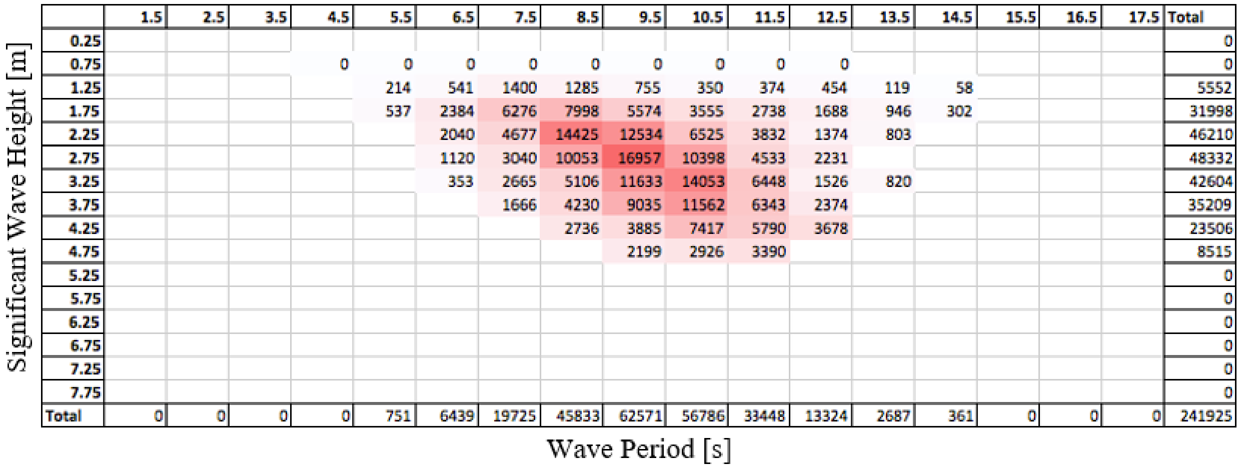

	1.5	2.5	3.5	4.5	5.5	6.5	7.5	8.5	9.5	10.5	11.5	12.5	13.5	14.5	15.5	16.5	17.5	Total
0.25																		0
0.75				0	0	0	0	0	0	0	0	0						0
1.25					214	541	1400	1285	755	350	374	454	119	58				5552
1.75					537	2384	6276	7998	5574	3555	2738	1688	946	302				31998
2.25						2040	4677	14425	12534	6525	3832	1374	803					46210
2.75						1120	3040	10053	16957	10398	4533	2231						48332
3.25						353	2665	5106	11633	14053	6448	1526	820					42604
3.75							1666	4230	9035	11562	6343	2374						35209
4.25								2736	3885	7417	5790	3678						23506
4.75									2199	2926	3390							8515
5.25																		0
5.75																		0
6.25																		0
6.75																		0
7.25																		0
7.75																		0
Total	0	0	0	0	751	6439	19725	45833	62571	56786	33448	13324	2687	361	0	0	0	241925

Figure 5.12: Annual energy [kWh] as a function of sea-state for actively controlled system.

For the Amphitrite Bank location, moderate sea-states continue to account for the bulk of the energy production, while low energy sea-states provide relatively small contributions. In total, the 66 studied sea-states result in the generation of 241.9 MWh, which is produced over 95.54% of the year. When converting this average to production over the entire year, the AOE device generates an average of 30.24 kW. This was an increase of 3.0% from the passive system. However, while the net performance gain from the active controlled system is relatively small, there are several indications that the annual power generation could be improved if the controller is implemented in more than one device. To assess this possibility, the energy output from the first and second devices in the cascade was determined, and compared to the passive system. The annual averaged power output from each of the three devices is shown in Table 5.7.

Table 5.7: Annual averaged power output from each of the devices.

Device	**Passive System [kW]**	**Active System [kW]**	**Improvement [kW]**	**Improvement [%]**
Device 1	10.57	11.40	0.83	7.9
Device 2	20.48	21.25	0.77	3.8
Device 3	29.37	30.24	0.87	3.0

The magnitude improvement remained approximately constant after the first device, which resulted in a progressively smaller decrease in the percentage improvement. Therefore, if the controller were implemented in multiple devices, it would be possible to further increase this magnitude improvement in latter devices, and maintain a moderate percentage gain. However, it is expected that gains will increase beyond that of 7.9%, for the reason that the system is governed by the continual throughput of air. In latter devices, if air cannot be pumped through then the pressure in upstream tanks remains high, which in turn increases the resistance to air throughput. This is seen inherently in the controller for a single device – by drawing air out of the piston more frequently, more air is drawn into the system from ambient thereby increasing the total throughput. When considering the WEC holistically, if air is drawn out of the third device more frequently, then this will increase the throughput of air in the first and second device, beyond what is already being seen. To illustrate this phenomena within a single device, the cumulative mass flow at the inlet and outlet of the first device is compared for the passive and actively controlled system. This comparison is given for a representative low energy sea-state of $H_s = 1.25$ m, $T_e = 6.5$ s in Fig. 5.13.

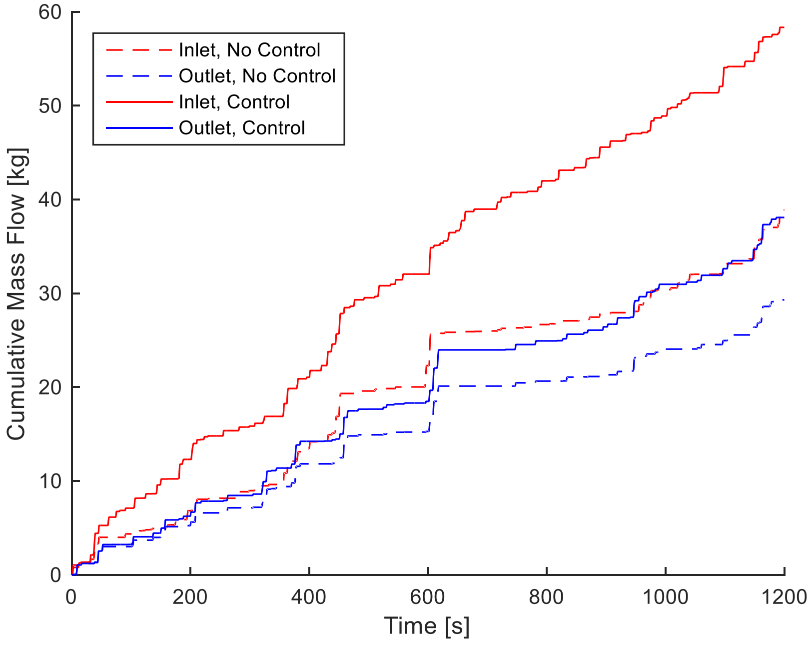

Figure 5.13: Cumulative mass flow at the inlet and outlet of D_1^*

In the passive system, 75.4% of the flow through the inlet is passed onwards to the subsequent device; comparatively, for the controlled system, 65.3% is passed onwards through the cascade. This drop is due to the lack of control in the subsequent device, which creates a resistance to flow that attenuates the improvements achieved with control. Therefore, despite significantly higher flow rates at the device inlet with the implementation of control, a smaller percentage of this mass flow is carried forward to subsequent devices. However, since the magnitude improvement compensates for this reduction in efficiency, there is still a net improvement in the flow onwards to the subsequent device. If control is implemented in all three devices, it is expected that continuity of mass flow will improve between devices, which will lead to gains in power production beyond that which is presently achieved.

However, this possibility is not considered in the current work. Instead, to better grasp how the recirculation strategy is influencing the throughput of air within the system, the efficiency of the WEC is analyzed. In particular, attention is placed on if the control strategy creates an efficiency improvement in each aspect of the power conversion chain; if so, then there is evidence to suggest that the performance of the strategy could be further improved with more devices. Alternatively, if a stage of the conversion process remains stagnant, then there may be a cap on potential performance improvements.

5.6.2 Efficiency

The efficiency of the system is measured in terms of two stages: the efficiency with which wave power is converted to absorbed power, and the rate at which the absorbed power is converted to useful power output. For the purpose of this work, these efficiencies are defined as the absorption and conversion efficiency, respectively, for which more detailed descriptions are provided in Section 4.4.1. Since the function of the active control strategy is to improve the conversion and absorption efficiency in low energy sea-states, these efficiencies are critical metrics for assessing the performance of the controller.

The conversion efficiency in the passively controlled system suffered in low energy sea-states, as the piston typically functioned as a spring in most waves, instead of capturing power. Conversely, under the influence of the active control strategy, the system recirculated air to improve power capture even in low energy waves. In order to compare the conversion efficiency under the influence of the active control strategy, the absorbed power as a function of sea-state is given in Fig. 5.14. The absorbed power was calculated as the sum across all three devices, for which the absorbed power in a particular device was calculated using Eq. 4.4.

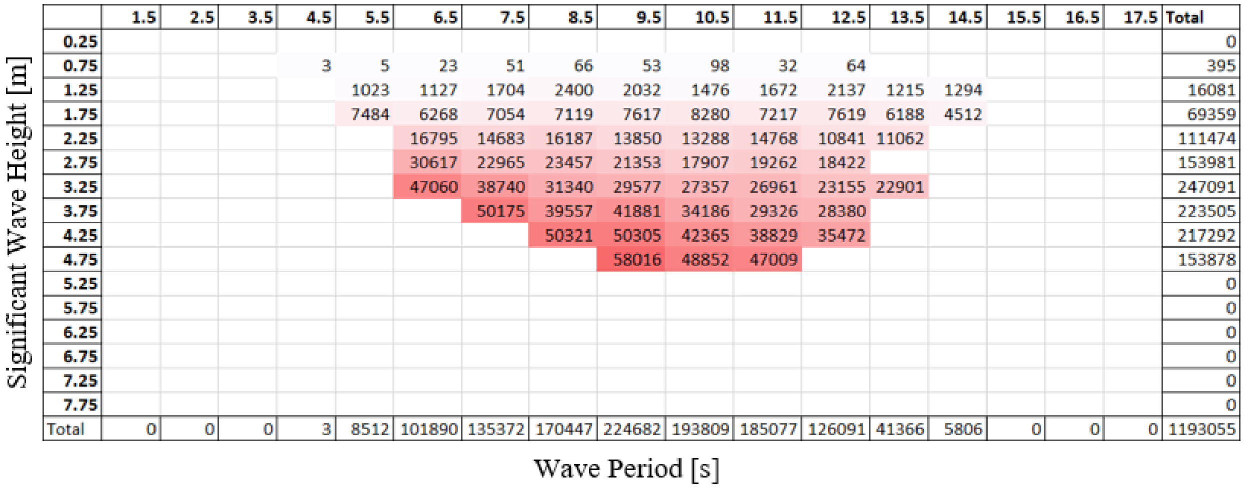

	1.5	2.5	3.5	4.5	5.5	6.5	7.5	8.5	9.5	10.5	11.5	12.5	13.5	14.5	15.5	16.5	17.5	Total
0.25																		0
0.75				3	5	23	51	66	53	98	32	64						395
1.25					1023	1127	1704	2400	2032	1476	1672	2137	1215	1294				16081
1.75					7484	6268	7054	7119	7617	8280	7217	7619	6188	4512				69359
2.25						16795	14683	16187	13850	13288	14768	10841	11062					111474
2.75						30617	22965	23457	21353	17907	19262	18422						153981
3.25						47060	38740	31340	29577	27357	26961	23155	22901					247091
3.75							50175	39557	41881	34186	29326	28380						223505
4.25								50321	50305	42365	38829	35472						217292
4.75									58016	48852	47009							153878
5.25																		0
5.75																		0
6.25																		0
6.75																		0
7.25																		0
7.75																		0
Total	0	0	0	3	8512	101890	135372	170447	224682	193809	185077	126091	41366	5806	0	0	0	1193055

Figure 5.14: Absorbed power [W] as a function of sea-state for actively controlled system.

As with the passively controlled system, the absorbed power in low energy seas is several orders of magnitude below that of higher energy wave conditions. In particular, in the lowest energy sea-states (H_s = 0.75 m), virtually no power is absorbed; this is expected, given that no power is produced in these see states. To provide a stronger comparison to the passively controlled system, the conversion efficiency is calculated as a measure of the readiness with which absorbed power is converted to useful power output. The conversion efficiency is defined using Eq. 4.5, for which the results are given in Fig. 5.15.

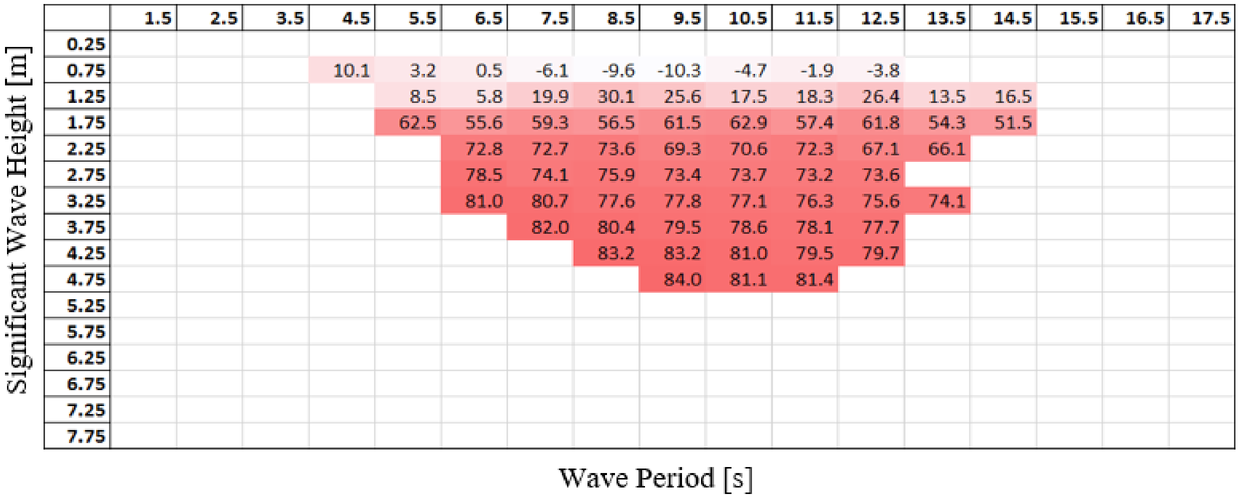

	1.5	2.5	3.5	4.5	5.5	6.5	7.5	8.5	9.5	10.5	11.5	12.5	13.5	14.5	15.5	16.5	17.5
0.25																	
0.75				10.1	3.2	0.5	-6.1	-9.6	-10.3	-4.7	-1.9	-3.8					
1.25					8.5	5.8	19.9	30.1	25.6	17.5	18.3	26.4	13.5	16.5			
1.75					62.5	55.6	59.3	56.5	61.5	62.9	57.4	61.8	54.3	51.5			
2.25						72.8	72.7	73.6	69.3	70.6	72.3	67.1	66.1				
2.75						78.5	74.1	75.9	73.4	73.7	73.2	73.6					
3.25						81.0	80.7	77.6	77.8	77.1	76.3	75.6	74.1				
3.75							82.0	80.4	79.5	78.6	78.1	77.7					
4.25								83.2	83.2	81.0	79.5	79.7					
4.75									84.0	81.1	81.4						
5.25																	
5.75																	
6.25																	
6.75																	
7.25																	
7.75																	

Figure 5.15: Conversion efficiency [%] as a function of sea-state for actively controlled system.

When considering the annual total of absorbed and produced energy, the annually-averaged conversion efficiency is 69.5%. The efficiency increases with the significant wave height, such that a peak efficiency of 84.0% is reached in 4.75 m waves with an energy period of 9.5 s. While lower than the peak in the passive system (85.3%), the actively controlled system still provides a wide band of sea-states that have efficiencies over 70%. Within the low efficiency band that was identified in the passive system, which corresponds to wave conditions below 1.75 m, the peak efficiency is 30.1%, which is achieved in 1.25 m waves with an energy period of 8.5 s. This is a slight drop from the passively controlled system. For a more detailed comparison of conversion efficiencies, Fig. 5.16 provides the percent improvement in the conversion efficiency when comparing the active and passively controlled WEC systems.

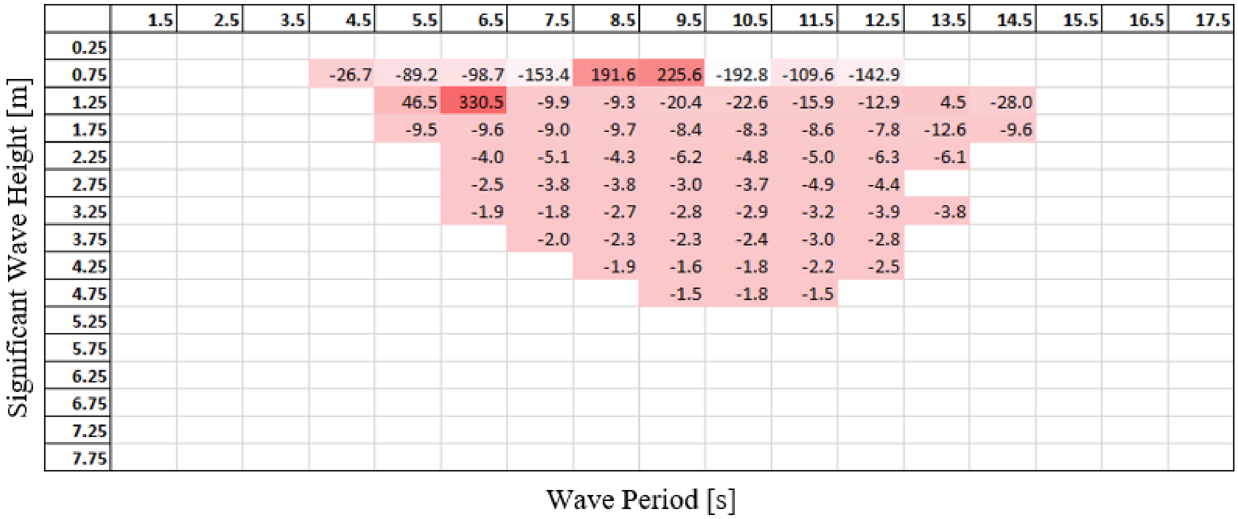

	1.5	2.5	3.5	4.5	5.5	6.5	7.5	8.5	9.5	10.5	11.5	12.5	13.5	14.5	15.5	16.5	17.5
0.25																	
0.75				-26.7	-89.2	-98.7	-153.4	191.6	225.6	-192.8	-109.6	-142.9					
1.25					46.5	330.5	-9.9	-9.3	-20.4	-22.6	-15.9	-12.9	4.5	-28.0			
1.75					-9.5	-9.6	-9.0	-9.7	-8.4	-8.3	-8.6	-7.8	-12.6	-9.6			
2.25						-4.0	-5.1	-4.3	-6.2	-4.8	-5.0	-6.3	-6.1				
2.75						-2.5	-3.8	-3.8	-3.0	-3.7	-4.9	-4.4					
3.25						-1.9	-1.8	-2.7	-2.8	-2.9	-3.2	-3.9	-3.8				
3.75							-2.0	-2.3	-2.3	-2.4	-3.0	-2.8					
4.25								-1.9	-1.6	-1.8	-2.2	-2.5					
4.75									-1.5	-1.8	-1.5						
5.25																	
5.75																	
6.25																	
6.75																	
7.25																	
7.75																	

Figure 5.16: Improvement in conversion efficiency [%] from passive to actively controlled system.

Aside from improvement in certain low energy sea-states, there is an overall drop in conversion efficiency across all sea-states. This drop is minor in moderate to high energy sea-states (less than ~5%), but is significant in many low energy sea-states. When considering the annually averaged conversion efficiency, there was a drop from 74.3% to 69.5%. The reason for this drop in efficiency is that the absorbed power under the influence of the controller increased, particularly in low energy sea-states. In part this was driven by the fact that energy absorption incorporates the net increase in the exergy of the air within the three devices, including the additional recirculation tanks. Since this does not directly contribute to the net power output, this would lead to a drop in power conversion efficiency. Therefore, while there was a net improvement in both power production and energy absorption, the rate by which power was converted decreased. As a measure of the rate by which power was absorbed, the absorption efficiency was calculated according to Eq. 4.6, for which the results are shown in Fig. 5.17.

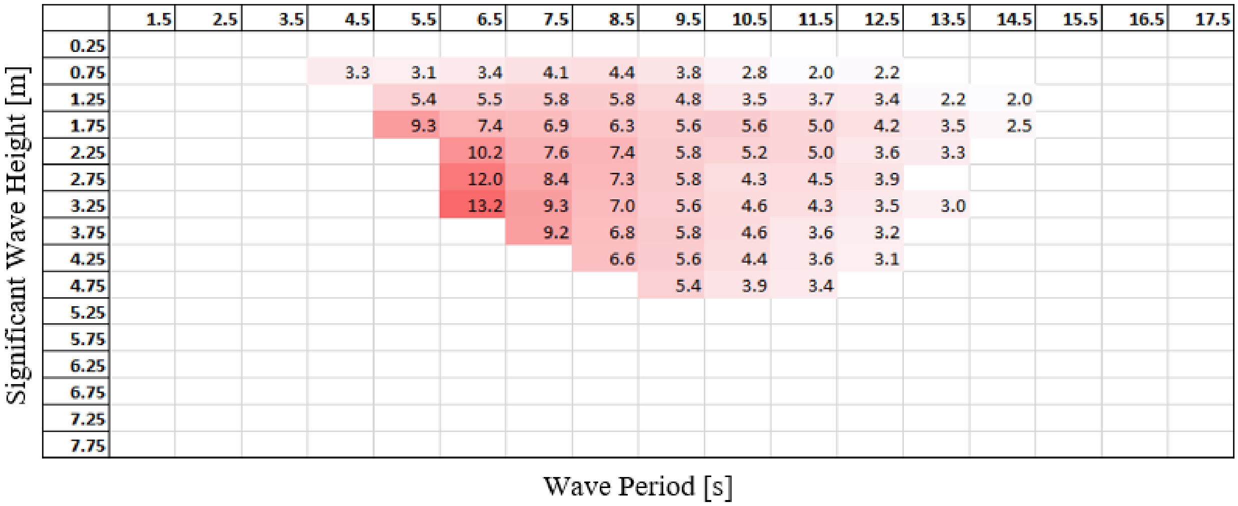

	1.5	2.5	3.5	4.5	5.5	6.5	7.5	8.5	9.5	10.5	11.5	12.5	13.5	14.5	15.5	16.5	17.5
0.25																	
0.75				3.3	3.1	3.4	4.1	4.4	3.8	2.8	2.0	2.2					
1.25					5.4	5.5	5.8	5.8	4.8	3.5	3.7	3.4	2.2	2.0			
1.75					9.3	7.4	6.9	6.3	5.6	5.6	5.0	4.2	3.5	2.5			
2.25						10.2	7.6	7.4	5.8	5.2	5.0	3.6	3.3				
2.75						12.0	8.4	7.3	5.8	4.3	4.5	3.9					
3.25						13.2	9.3	7.0	5.6	4.6	4.3	3.5	3.0				
3.75							9.2	6.8	5.8	4.6	3.6	3.2					
4.25								6.6	5.6	4.4	3.6	3.1					
4.75									5.4	3.9	3.4						
5.25																	
5.75																	
6.25																	
6.75																	
7.25																	
7.75																	

Figure 5.17: Absorption efficiency [%] as a function of sea-state for actively controlled system.

When considering the total absorbed energy annually, the annually-averaged absorption efficiency is 5.2%. The peak absorption efficiency was 13.2%, achieved in seas with a wave height of 3.25 m and an energy period of 6.5 s. A comparison of the increase in the absorption efficiency under the influence of the controller is provided in Fig. 5.18.

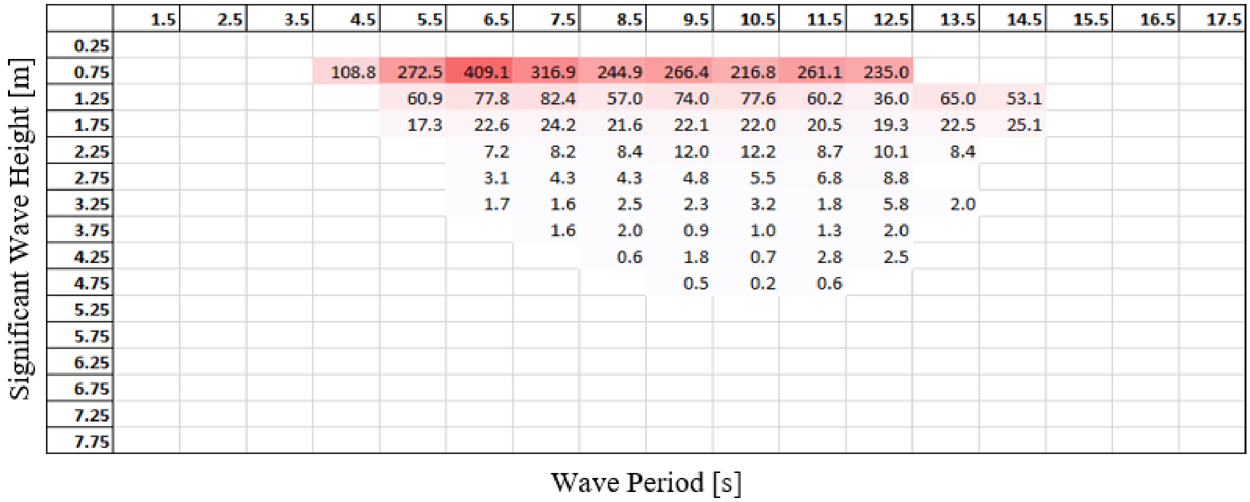

	1.5	2.5	3.5	4.5	5.5	6.5	7.5	8.5	9.5	10.5	11.5	12.5	13.5	14.5	15.5	16.5	17.5
0.25																	
0.75				108.8	272.5	409.1	316.9	244.9	266.4	216.8	261.1	235.0					
1.25					60.9	77.8	82.4	57.0	74.0	77.6	60.2	36.0	65.0	53.1			
1.75					17.3	22.6	24.2	21.6	22.1	22.0	20.5	19.3	22.5	25.1			
2.25						7.2	8.2	8.4	12.0	12.2	8.7	10.1	8.4				
2.75						3.1	4.3	4.3	4.8	5.5	6.8	8.8					
3.25						1.7	1.6	2.5	2.3	3.2	1.8	5.8	2.0				
3.75							1.6	2.0	0.9	1.0	1.3	2.0					
4.25								0.6	1.8	0.7	2.8	2.5					
4.75									0.5	0.2	0.6						
5.25																	
5.75																	
6.25																	
6.75																	
7.25																	
7.75																	

Figure 5.18: Improvement in absorption efficiency [%] from passive to actively controlled system.

With the active controller, there is universal increase in the absorbed power; this aligns with the proposed explanation for the decrease in the conversion efficiency. When considering the annually averaged absorption efficiency, there was an increase from 4.7% to 5.2%. In a particular sea-state, the peak increase is 409.1%, which is achieved in seas with a wave height of 0.75 m and an energy period of 6.5 s. The absorption efficiency increased significantly for all conditions with a wave height of 0.75 m; however, increases of ~20% persist in sea-states up to 1.75 m. To provide a better idea of the trade-off between conversion and absorption efficiency, the net change in power conversion efficiency (from the wave resource to the useful power output) is given in Fig. 5.19. The total power conversion efficiency is calculated as the product of the conversion and absorption efficiencies.

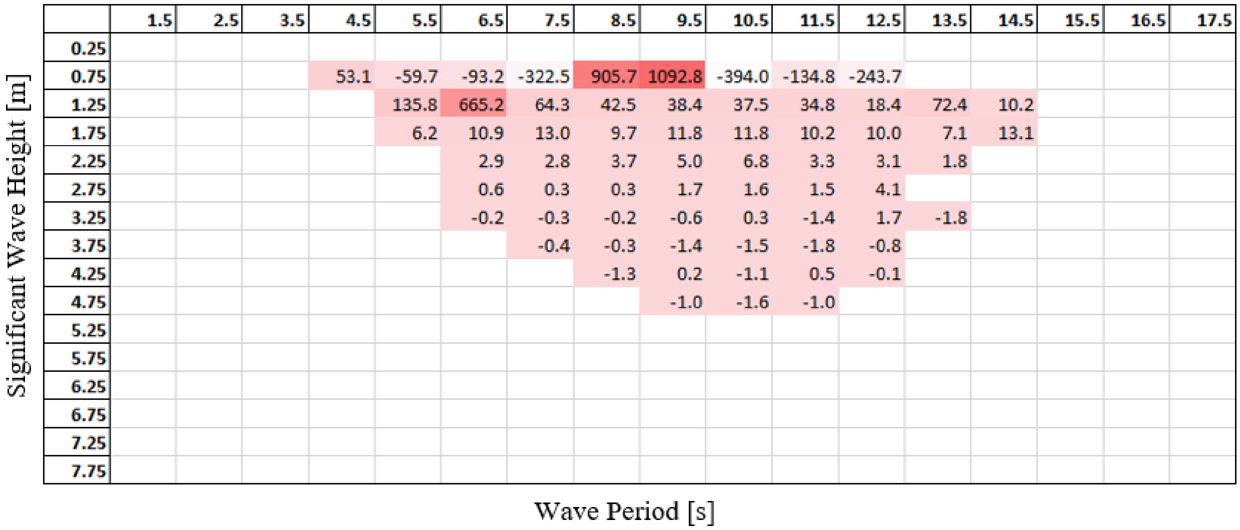

	1.5	2.5	3.5	4.5	5.5	6.5	7.5	8.5	9.5	10.5	11.5	12.5	13.5	14.5	15.5	16.5	17.5
0.25																	
0.75				53.1	-59.7	-93.2	-322.5	905.7	1092.8	-394.0	-134.8	-243.7					
1.25					135.8	665.2	64.3	42.5	38.4	37.5	34.8	18.4	72.4	10.2			
1.75					6.2	10.9	13.0	9.7	11.8	11.8	10.2	10.0	7.1	13.1			
2.25						2.9	2.8	3.7	5.0	6.8	3.3	3.1	1.8				
2.75						0.6	0.3	0.3	1.7	1.6	1.5	4.1					
3.25						-0.2	-0.3	-0.2	-0.6	0.3	-1.4	1.7	-1.8				
3.75							-0.4	-0.3	-1.4	-1.5	-1.8	-0.8					
4.25								-1.3	0.2	-1.1	0.5	-0.1					
4.75									-1.0	-1.6	-1.0						
5.25																	
5.75																	
6.25																	
6.75																	
7.25																	
7.75																	

Figure 5.19: Improvement in total power conversion efficiency [%] from passive to actively controlled system.

While there is no conclusive improvement/decrease in sea states of 0.75 m, there are universal improvements in low – moderate energy sea states with wave heights up to 3.25 m. In particular, sea-states with wave heights of 1.25 m and 1.75 m saw significant improvement. When considering the annually-average power conversion efficiency across all sea-states, there was an increase from 3.5% to 3.6% with the implementation of active control. This is an indication that the active controller improves the net efficiency with which power is absorbed and converted from low energy waves. This improvement is significantly larger than that seen in net power output, because the power absorption factors in improvements across all three devices, rather than improvements solely made in the third device. In order to better assess improvements in efficiency as a function of the energy of the sea-state, Table 5.8 summarizes the efficiency and energy production under the influence of the active control strategy as a function of significant wave height.

Table 5.8: Summary of the efficiency and energy production of the actively controlled AOE WEC as a function of significant wave height.

Wave Height [m]	**0.75**	**1.25**	**1.75**	**2.25**	**2.75**	**3.25**	**3.75**	**4.25**	**4.75**
Conversion Efficiency [%]	-2.27	17.83	58.71	71.21	74.01	77.25	78.92	80.86	81.86
Absorption Efficiency [%]	3.33	4.94	6.01	6.27	5.67	5.21	4.90	4.32	4.02
Total Efficiency [%]	-0.08	0.88	3.53	4.47	4.20	4.03	3.86	3.50	3.29
Probability of Occurrence [%]	6.15	25.68	24.10	16.51	11.87	7.50	4.78	2.62	0.80
Component of Annual Wave Power Transport [%]	0.55	6.98	13.72	16.02	17.84	16.42	14.14	10.39	3.93
Component of Energy Production [%]	0.00	2.29	13.23	19.10	19.98	17.61	14.55	9.72	3.52

NOTE: All probabilities are calculated relative to the sea-states included in the generation of the PM spectrum, not all sea-states annually. These values were selected to ensure the scaling of the percentage difference in the resource and energy production was consistent.

When considering solely the sea-states used in the generation of the power matrix, seas with wave heights between 0.75 m – 1.75 m encompass 55.93% of the hours; under the influence of the active controller, these sea-states account for 15.52% of the energy production, compared to 13.74% for the passively controlled system. While this is still quite low, this corresponds to a 16.3% improvement in energy production over the passive system. A direct comparison in the component of energy production as a function of wave height is given in Table 5.9.

Table 5.9: Comparison of the component of the annual energy production as a function of significant wave height for the passive and actively controlled system.

Wave Height [m]	**0.75**	**1.25**	**1.75**	**2.25**	**2.75**	**3.25**	**3.75**	**4.25**	**4.75**
Component of Energy Production , Passive [%]	0.00	1.52	12.22	18.88	20.30	18.20	15.18	10.05	3.67
Component of Power Production, Active [%]	0.00	2.29	13.23	19.10	19.98	17.61	14.55	9.72	3.52
Improvement [%]	0.00	50.66	8.27	1.17	-1.58	-3.24	-4.15	-3.28	-4.09

The percent improvement in sea-states of 1.25 m is particularly significant; however, this corresponds to a small change in terms of magnitude. Therefore, while the strategy functioned as intended, there is still a significant discrepancy in energy production. However, it is important to recognize that there may be additional benefits to these changes, aside from the magnitude of power output per sea-state. In particular, aside from a wave height of 0.75 m, there is an increase in the contribution from the lowest energy half of sea-states, as well as a decrease in the highest energy half of sea-states. Therefore, the active controller provides an increase in the total energy consumption, as well as in the continuity of power production throughout the year. This may increase the ease with which power is incorporated into the grid. Furthermore, the percent contributions are skewed in part by the inclusion of power output from the highest energy sea-states. These sea-states may require the WEC to convert to a survivability mode; if this is case, then the low energy sea-states are currently being undervalued in terms of the percent contribution to the power output. Lastly, as a result of the net increase in power conversion efficiency with active control, there is a basis for stating that further improvements could be achieved by implementing the control strategy in multiple devices. In particular, the increase in power absorption as a result of active control implementation ensures that the available energy would also increase. This would prevent a cap from forming on the maximum power output from control implementation. If further gains could be achieved with recirculation in multiple devices, then there would be a much more dramatic change in the power output in low energy sea-states, which would further smooth the annual distribution of power output.

5.7 Summary of Active Controller

In this chapter, an active controller was developed for the increase of power production in low energy sea-states; the controller was subsequently applied to the first device in the AOE WEC. The active controller applied a strategy by which the energy absorption in low energy sea-states was increased by improving the continuity of air throughput. In particular, the active controller used valve control in combination with four variable pressure accumulator tanks to recirculate air within both the upper and lower chambers of the piston. The selected configuration of active controller used a single recirculation tank for the upper chamber, two recirculation tanks for the lower chamber, and a single air throughput tank. This configuration was selected following the study of 1, 2, 3, and 4 - recirculation tank arrangements. The study of each of these arrangements was enabled by the application of the dynamically coupled model developed in Chapter 2.

Following the selection of an optimal active controller, a power matrix for the actively controlled AOE WEC was developed. In addition to providing comprehensive performance data for the AOE WEC under the influence of a novel active control strategy, the power matrix data was used to assess the performance benefit achieved with increased control complexity. In particular, the actively controlled system was found to produce 30.24 kW, which was an increase of 3.0% over the passively controlled system. The increase in power production in the first and second devices in the WEC chain were 7.8% and 3.8%, respectively. In addition to performance improvements, the absorption efficiency saw a marked improvement, from 4.7% to 5.2%. This provided a basis for stating that the overall power production of the system could further be improved with implementation of the active controller in the second and third devices of the AOE WEC.

However, even with implementation in a single device, the active controller increased the continuity of power production throughout year. The component of the annual power production increased in sea-states with significant wave heights of 1.25 m – 2.25 m, while decreasing in sea-states with greater wave heights. This change was driven by a significant increase in the component of annual power production in low-energy sea-states (those with significant wave heights of 0.75 m – 1.75 m) from 13.74% to 15.52%, when compared to the passively controlled system. Therefore, the active controller was successful in increasing both the energy absorption and power production of low-energy sea-states.

Chapter 6. Conclusions and Future Work

In this work, a dynamically coupled model architecture of the Accumulated Ocean Energy Inc. wave energy converter was developed using the finite element solver ProteusDS and MATLAB/Simulink. This model architecture was subsequently applied for implementation of passive and active control in the AOE WEC, for which detailed performance assessments were conducted at each stage. Through the development and implementation of these stages, significant contributions were made to the fields of wave energy modelling and control, while also uncovering new directions for future research. This chapter summarizes these findings, through the discussion of conclusions, recommendations, and future work.

6.1 Conclusions

Recent improvements in the complexity and computational speed of numerical methods have seen an increased interest in the application of numerical simulation tools for the modelling of wave energy converter devices. However, many of these approaches make use of significant simplifying assumptions, particularly in modelling the WEC power take-off. Consequently, the implementation of control in a cascaded technology such as the AOE WEC necessitated the development of an improved model architecture; in particular, one that could simultaneously resolve the real-time state of particular PTO components within multiple WEC devices, without prohibitive computational times. The developed model architecture expanded on the dynamically coupled modelling approach developed by Bailey et al [6] [27] in order to resolve the hydrodynamic, PTO, and mooring forcing acting on the three devices within the AOE WEC. These forces are then used to determine the complete state of the system at each time step of the simulation. The subsequent application of this modelling approach to a passive control problem demonstrated high sensitivity to PTO parameter selection, which suggests that the fidelity of the developed model may be critical for developing realistic PTO designs and control strategies.

The passive control problem was realized as an optimization of eight critical PTO parameters with the objective of maximizing exergy output. After only 15 generations, the optimization procedure led to an increase of 330.35% over an initial, informed estimate of the optimal design. As a result, the developed methodology reduced reliance on complete knowledge of the WEC design space when attempting to maximize power output. Furthermore, the developed procedure simultaneously informed future research directions through the exploration of power quality and survivability considerations. In particular, compromises in the design space were identified, such that a 5.5% reduction in exergy output was sufficient to produce a 55% reduction in the end-stop collision rate. Furthermore, the disparity in power production between low and moderate energy sea-states informed the objective of the active control strategy; namely, the increase of power production in low energy sea-states.

The developed controller was limited by the pneumatic and cascaded nature of the AOE WEC. In contrast to much of the control literature, an optimal PTO force could not be dictated directly; instead, focus was placed on developing a realistic control strategy that was structured around the improvement of device efficiency in low energy sea-states. To this aim, a recirculation-based control strategy was developed, in which three accumulator tanks were used to selectively pressurize and de-pressurize the piston at opportune times, thereby increasing the continuity of air throughput. Under the influence of the active controller, the annually-averaged power output increased by 3.0%, from 29.37 kW to 30.24 kW; this represented an increase in efficiency from 3.5% to 3.6%. Furthermore, the contribution of low-energy sea-states to the annual power output increased significantly. In particular, sea-states with significant wave heights between 0.75 m – 1.75 m, which encompass 55.93% of the hours on average throughout the year, saw their contribution to the annual power production increase from 13.74% to 15.52%.

In addition to this improvement, these metrics do not capture the intrinsic value in increasing power continuity; as a result, there is significant value in implementing the active controller.

In conclusion, the development of a dynamically coupled model for the AOE WEC enabled the implementation of passive and active control in the AOE WEC, which resulted in significant improvements to the quantity and quality of power output. These control strategies account for and incorporate realistic PTO parameters, and as a result, provide significant value for the continued development of the AOE WEC. More importantly, these improvements demonstrate the significant value in the implementation of this tiered control methodology, with the hope that this work will better inform WEC control development in the future.

6.2 Recommendations and Future Work

This work has produced a number of technical tools, which are of significant value to the WEC modelling and control fields. However, to inform future research in the implementation of control in cascaded pneumatic wave energy converters, several key areas were identified for future work. These research directions are broken into two major categories: model validation and further control assessment/implementation.

6.2.1 Model Validation and Improvement

The first potential research direction lies in the experimental validation of the dynamically coupled modeling approach. While the model made use of experimentally verified ProteusDS software and literature-based thermodynamic equations, the accuracy of individual components is not sufficient to verify the accuracy of the collective model. Therefore, future work may perform tank testing in order to validate larger components of the modelling structure. In particular, work can assess the accuracy of the PTO model both with/without the active controller, in order to see if the accuracy of the model is significantly affected by the introduction of additional dynamic perturbations.

Furthermore, the model may be expanded to include a dynamic model of the on-shore architecture. This would properly account for the effect of control on the power conversion chain, while resolving components such as the pipeline to shore; these components are critical for assessing downstream losses in the power conversion process, and may lead to more accurate assessments of the final power production. In addition, the simplified assumption of dry air within the system may be better resolved, through the inclusion of site and temperature-specific humidity in the ambient air. Accounting for humidity will likely have a substantial effect on the temperature gain during piston compression.

6.2.2 Future Control Implementation

In addition to model-based considerations, several directions for future work arose from the optimization results. Primary among these considerations are the more accurate assessment of the effect of power quality and end-stop collision rate on the optimal design. While both of these considerations are important for the eventual deployment of the AOE WEC, these factors were not included in the objective function of the optimization. Consequently, future work could assess the potential design compromises arising from the inclusion of these factors. In particular, future work must address the collision rate as it is prohibitively high (~1.34 collisions/min), and must be reduced if the design is to be considered feasible. However, the collision rate does not provide sufficient data to accurately assess the potential design compromises needed to ensure WEC survivability. In order to assess the design compromise arising from the inclusion of both power output and survivability factors, future work may perform a design optimization in which the force limits in the converter are resolved. For example, these limits may address design constraints on the moorings, PTO force, and end-stop collision rate. Conversely, active control may be assessed as a method of reducing the end-stop collision rate.

In addition, future work may continue the optimization procedure in order to attempt to identify a global optimum; however, given that there was a 311.98% increase in the objective function following the first seven generations, and an 18.37% increase in the subsequent eight generations (despite an increase in the population size from 60 to 90), it is expected that there will be diminishing returns in doing so.

In regards to the active controller, future work should address the inclusion of active control in two- and three-device configurations. This will better indicate the potential performance improvements seen with active control implementation, while simultaneously providing a more complete perspective on the trade-off between power production and control complexity. As can be seen in Chapter 5, the net increase in the power output from the first device is 7.9%; however, half of this improvement is lost due to the passive control of the subsequent two devices. With control implementation in the subsequent two devices, even if only two recirculation tanks are used, a larger chunk of this improvement could be carried forward to the final device. More importantly, there is evidence to suggest that the gains could be higher than 8%. In particular, the WEC is highly sensitive to the continual throughput of air. If air from the third device is drawn out more frequently, then this increases the efficiency of air throughput in the previous two devices. Removal of this bottleneck with the implementation of a holistic active control strategy may lead to further improvements. Secondly, the active control strategy provided significant improvements in the efficiency of wave power absorption. Since this is the first stage in the energy conversion process, the strategy increases the cap on net power production.

References

[1] K. Gunn and C. Stock-Williams, "Quantifying the global wave power resource," *Renewable Energy,* vol. 44, pp. 296-304, 23 February 2013.

[2] S. J. Beatty, P. Wild and B. J. Buckham, "Integration of a wave energy converter into the electricity supply of a remote Alaskan island," *Renewable Energy,* vol. 35, no. 6, pp. 1203-1213, 2010.

[3] I. Lopez, J. Andreu, S. Ceballos, I. M. de Alegria and I. Kortabarria, "Review of wave energy technologies and the necessary power-equipment," *Renewable and Sustainable Energy Reviews,* vol. 27, pp. 413-434, 2013.

[4] Y. Li and Y.-H. Yu, "A synthesis of numerical methods for modeling wave energy converter-point absorbers," *Renewable and Sustainable Energy Reviews,* vol. 16, pp. 4352-4364, 5 June 2012.

[5] B. R. Robertson, C. E. Hiles and B. J. Buckham, "Characterizing the near shore wave energy resource on the west coast of Vancouver Island, Canada," *Renewable Energy,* no. 71, pp. 665-678, 27 November 2014.

[6] H. Bailey, J. P. Ortiz, B. Robertson, B. J. Buckham and R. S. Nicoll, "A Methodology for Wave-to-Wire WEC Simulations," in *2nd Marine Energy Technology Symposium,* Seattle, 2014.

[7] M. Penalba and J. V. Ringwood, "A Review of Wave-to-Wire Models for Wave Energy Converters," *Energies,* vol. 9, no. 506, 30 June 2016.

[8] A. F. d. O. Falcao, "Wave energy utilization: A review of the technologies," *Renewable and Sustainable Energy Reviews,* vol. 14, pp. 899-918, 2010.

[9] J. Falnes, "A review of wave-energy extraction," *Marine Structures,* vol. 20, pp. 185-201, 2007.

[10] A. Clement, P. McCullen, A. Falcao, A. Fiorentino, F. Gardner, K. Hammarlund, G. Lemonis, T. Lewis, K. Nielson, S. Petroncini, M.-T. Pontes, P. Schild, B.-O. Sjostrom, H. C. Sorensen and T. Thorpe, "Wave energy in Europe: current status and perspectives," *Renewable and Sustainable Energy Reviews,* vol. 6, pp. 405-431, 2002.

[11] S. Beatty, "Self-Reacting Point Absorber Wave Energy Converters," 2015.

[12] A. Uihlein and D. Magagna, "Wave and tidal current energy - A review of the current state of research beyond technology," *Renewable and Sustainable Energy Reviews,* vol. 58, pp. 1070-1081, May 2016.

[13] R. F. Beck and A. M. Reed, "Modern Computational Methods for Ships in a Seaway," *Transactions: Society of Naval Architects and Marine Engineers,* vol. 109, pp. 1-51, 2001.

[14] A. E. Maguire, *Hydrodynamcs, control and numerical modelling of absorbing wavemakers,* University of Edinburgh, 2011.

[15] A. Day, A. Babarit, A. Fontaine, Y.-P. He, M. Kraskowski, M. Murai, I. Penesis, F. Salvatore and H.-K. Shin, "Hydrodynamic modelling of marine renewable energy devices: A state of the art review," *Ocean Engineering,* vol. 108, pp. 46-69, 24 August 2015.

[16] M. Folley, Numerical Modelling of Wave Energy Converters, Elsevier Inc., 2016.

[17] M. P. Retes, G. Giorgi and J. V. Ringwood, "A Review of Non-Linear Approaches for Wave Energy Converter Modelling," in *11th European Wave and Tidal Energy Conference,* Nantes, 2011.

[18] J. G. Bretl, *A Time Domain Model for Wave Induced Motions Coupled to Energy Extraction,* University of Michigan, 2009.

[19] C. Lee and J. Newman, "Computation of wave effects using the panel method," in *Numerical models in fluid-structure interaction*, Southampton, WIT Press, 2004.

[20] A. Combourieu, M. Lawson, A. Babarit, K. Ruehl, A. Roy, R. Costello, P. L. Weywada and H. Bailey, "WEC3: Wave Energy Converter Code Comparison Project," in *11th European Wave and Tidal Energy Conference,* Nantes, 2015.

[21] P. B. Garcia-Ross, R. Costello, F. Dias and J. V. Ringwood, "Hydrodynamic Modelling Competition - Overview and Approaches," in *34th International Conference on Ocean, Offshore and Arctic Engineering,* St. John's, 2015.

[22] M. Lawson, B. B. Garzon, F. Wendit, Y.-H. Yu and C. Michelen, "COER Hydrodynamic Modelling Competition: Modelling the Dynamic Response of a Floating Body Using the WEC-Sim and FAST Simulation Tools," in *34th International Conference on Ocean, Offshore, and Arctic Engineering*, St. John's, 2015.

[23] A. R. Roy, S. J. Beatty, V. Mishra, D. M. Steinke, R. S. Nicoll and B. J. Buckham, "Comparison of Numerical Simulations with Experimental Measurements for the Response of a Modified Submerged Horizontal Cylinder Moored in Waves," in *34th International Conference on Ocean, Offshore, and Arctic Engineering,* St. John's, 2015.

[24] C. M. Sandvik, *Wave-to-Wire Model of the Wave Energy Converter Bolt2,* Norwegian University of Science and Technology, 2012.

[25] K. Nielson, M. M. Kramer, F. Ferri, A. S. Zurkinden and M. Alves, "Overview of Wave to Wire Models," Aalborg, 2014.

[26] D. I. M. Forehand, A. E. Kiprakis, A. J. Nambiar and A. R. Wallace, "A Fully Coupled Wave-to-Wire Model of an Array of Wave Energy Converters," *IEEE Transactions on*

Sustainable Energy, vol. 7, no. 1, pp. 118-128, January 2016.

[27] H. Bailey, B. R. Robertson and B. J. Buckham, "Wave-to-wire simulation of a floating oscillating water column wave energy converter," *Ocean Engineering,* no. 125, pp. 248-260, 17 August 2016.

[28] WAMIT Inc., "WAMIT User Manual, Version 7.2," WAMIT Inc., Chestnut Hill, MA, 2016.

[29] S. Soylu, "Incorporation of the Articulated-Body Equations into a Model-Based Sliding-Mode Controller for the Reduction of Dynamic Coupling Effect in Underwater-Manipulator Systems," University of Victoria, 2005.

[30] J. P. Ortiz, *The Influence of Mooring Dynamics on the Performance of Self Reacting Point Absorbers,* University of Victoria, 2016.

[31] Dynamic Systems Analysis Ltd., "ProteusDS Manual; ProteusDS v2.34," Dynamic Systems Analysis Ltd., Halifax, 2017.

[32] B. J. Buckham, *Dynamics Modelling of Low-Tension Tethers for Submerged Remotely Operated Vehicles,* University of Victoria, 2003.

[33] B. Robertson, H. Bailey, D. Clancy, J. Ortiz and B. Buckham, "Influence of wave resource assessment methodology on wave energy production estimates," *Renewable Energy,* vol. 86, pp. 1145-1160, 2016.

[34] S. Bhattacharjee, "Properties of Various Ideal Gases (at 300 K)," [Online]. Available: https://www.ohio.edu/mechanical/thermo/property_tables/gas/idealGas.html. [Accessed 10 July 2017].

[35] J. F. Carneiro and F. G. de Almeida, "Reduced-order thermodynamic models for servo-pneumatic actuator chambers," *Journal of Systems and Control Engineering,* vol. 220, no. 1, pp. 301-314, 13 March 2006.

[36] V. Blagojevic and M. Stojiljkovic, "Mathematical and Simulink Model of the Pneumatic System with Bridging of the Dual Action Cylinder Chambers," *Mechanical Engineering,* no. 5, pp. 22-31, 2007.

[37] Y.-M. Kim, J.-H. Lee, S.-J. Kim and D. Favrat, "Potential and Evolution of Compressed Air Energy Storage: Energy and Exergy Analyses," *Entropy,* vol. 14, pp. 1501-1521, 2012.

[38] A. Rogers, A. Henderson, X. Wang and M. Negnevitsky, "Compressed Air Energy Storage: Thermodynamic and Economic Review," in *PES General Meeting,* National Harbor, 2014.

[39] H. Struchtrup, Thermodynamics and Energy Conversion, Berlin: Springer-Verlag, 2014.

[40] Atlas Copco, "Using Cataloque Performance Data," Atlas Copco, 2016. [Online]. Available: http://www.atlascopco.com/airmotors/aboutairmotors/technicalguide/usingcatalogue/. [Accessed 8 January 2017].

[41] Deprag, "Air Motors," Deprag, September 2014. [Online]. Available: http://www.deprag.com/fileadmin/bilder_content/emedia/broschueren_pics/emedia_druckluftmotoren/D6000/D6000en.pdf. [Accessed 8 January 2017].

[42] Ingersoll Rand, "Air Motors," Ingersoll Rand, 2016. [Online]. Available: https://www.ingersollrandproducts.com/en-us/power-tools/products/air-motors.html. [Accessed 08 January 2017].

[43] MODEC, "Air Motor Handbook," MODEC, [Online]. Available: http://www.modec.fr/our-solutions/air-motors/?lang=en. [Accessed 31 May 2017].

[44] Parker, "Air Motors," Parker Hannifin Corp, 2017. [Online]. Available: http://www.parker.com/. [Accessed 31 May 2017].

[45] PSI Automation, "Motor Selection Guide," PSI Automation, [Online]. Available: http://www.psiautomation.com/motor-select.cfm. [Accessed 08 January 2017].

[46] Dresser Rand, "KG2 Gas Turbines," Dresser Rand, 2017. [Online]. Available: https://www.dresser-rand.com/products-solutions/0-15-mw/kg2-gas-turbines/. [Accessed 31 May 2017].

[47] MAN Turbomachinery, "Gas Turbines," MAN Diesel and Turbo, 2017. [Online]. Available: http://turbomachinery.man.eu/products/gas-turbines. [Accessed 31 May 2017].

[48] A. A. E. Price, "New Perspectives on Wave Energy Converter Control," The University of Edinburgh, 2009.

[49] P. Ricci, M. Alves, A. Falco and A. Sarmento, "Optimisation of the Geometry of Wave Energy Converters," in *International Conference Ocean Energy*, Bremerhaven, 2006.

[50] W.-c. Zhang, H.-x. Liu, L. Zhang and X.-w. Zhang, "Hydrodynamic analysis and shape optimization for vertical axisymmetric wave energy converters," *China Ocean Engineering*, vol. 30, no. 6, pp. 954-966, December 2016.

[51] B. Bouali and S. Larbi, "Contribution to the Geometry Optimization of an Oscillating Water Column Wave Energy Converter," *Energy Procedia*, vol. 36, pp. 565-573, 2013.

[52] M. Gomes, C. Nascimento, B. Bonafini, E. Santos, L. Isoldi and L. Rocha, "Two-Dimensional Geometric Optimization of an Oscillating Water Column Converter in Laboratory Scale," *Thermal Engineering*, vol. 11, no. 1-2, pp. 30-36, 2012.

[53] R. A. Durren, "Absorber Geometry Optimization for a New Wave Energy Converter," 2012.

[54] T. Mundon and B. Nair, "Optimization of a Magnetostrictive Wave Energy Converter," in *Grand Renewable Energy*, Tokyo, 2014.

[55] J. Goggins and W. Finnegan, "Shape optimization of floating wave energy converters for a specified wave energy spectrum," *Renewable Energy*, vol. 71, pp. 208-220, November 2014.

[56] M. Colby, E. Nasroullahi and K. Tumer, "Optimizing Ballast Design of Wave Energy Converters Using Evolutionary Algorithms," in *Genetic and Evolutionary Computation Conference*, Dublin, 2011.

[57] A. McCabe, G. Aggidis and M. Widden, "Optimizing the shape of a surge-and-pitch wave energy collector using a genetic algorithm," *Renewable Energy*, vol. 35, no. 12, pp. 2767-2775, December 2010.

[58] A. Kurniawan, "Modelling and geometry optimisation of wave energy converters," 2013.

[59] A. Babarit and A. Clement, "Shape optimization of the SEAREV wave energy converter," in *9th World Renewable Energy Conference*, Firenze, 2006.

[60] L. Victor, P. Troch and J. P. Kofoed, "On the Effects of Geometry Control on the Performance of Overtopping Wave Energy Converters," *Energies*, vol. 4, no. 10, pp. 1574-1600, 2011.

[61] J.-C. Gilloteaux and J. Ringwood, "Control-informed geometric optimisation of wave energy converters," *IFAC Proceedings Volumes,* vol. 43, no. 20, pp. 366-371, September 2010.

[62] T. Weise, Global Optimization Algorithms - Theory and Applications, 2nd Edition ed., Online: Self-Published, 2009.

[63] S. P. Lim and H. Harin, "Performance Comparison of Genetic Algorithm, Differential Evolution and Particle Swarm Optimization Towards Benchmark Functions," in *IEEE Conference on Open Systems*, Sarawak, 2013.

[64] Det Norske Veritas, "Modelling and Analysis of Marine Operations," Det Norske Veritas, 2011.

[65] International Electrotechncal Commission, "Electricity producing wave energy converters - Power performance assessment," International Electrotechncal Commission, 2017.

[66] E. Ozkop and I. H. Altas, "Control, power and electrical components in wave energy conversion systems: A review of the technologies," *Renewable and Sustainable Energy Reviews,* vol. 67, pp. 106-115, 2017.

[67] J. Falnes, "Optimum Control of Oscillation of Wave-Energy Converters," *International Journal of Offshore and Polar Engineering*, vol. 12, pp. 147-155, 2002.

[68] D. Evans, "Power from Water Waves," *Annual Review of Fluid Mechanics,* vol. 13, pp. 157-187, 1981.

[69] B. Drew, A. R. Plummer and M. Sahinkaya, "A review of wave energy converter technology," *Proceedings of the Institution of Mechanical Engineers, Part A: Journal of Power and Energy,* vol. 223, pp. 887-902, 2014.

[70] S. Salter, J. Taylor and N. Caldwell, "Power conversion mechanisms for wave energy," *Proceedings of the Institution of Mechanical Engineers, Part M: Journal of Engineering for the Maritime Environment,* vol. 216, 2002.

[71] S. R. Nielson, Q. Zhou, M. M. Kramer, B. Basu and Z. Zhang, "Optimal control of nonlinear wave energy point converters," *Ocean Engineering,* vol. 72, pp. 176-187, 2013.

[72] J. Hals, J. Falnes and T. Moan, "A Comparison of Selected Strategies for Adaptive Control of Wave Energy Converters," *Journal of Offshore Mechanics and Arctic Engineering,* vol. 133, 2011.

[73] J. Falnes, "Wave-Energy Conversion Through Relative Motion Between Two Single-Mode Oscillating Bodies," *Journal of Offshore Mechanics and Arctic Engineering,* vol. 121, pp. 32-38, 1999.

[74] D. Valerio, P. Beirao and J. S. d. Costa, "Reactive control and phase and amplitude control applied to the Archimedes Wave Swing," in *Proceedings of the Seventeenth International Offshore and Polar Engineering Conference*, Lisbon, 2007.

[75] E. Tedeschi, M. Carraro, M. Molinas and P. Mattavelli, "Effect of Control Strategies and Power Take-Off Efficiency on the Power Capture From Sea Waves," *IEEE Transactions on Energy Conversion*, vol. 26, no. 4, pp. 1088-1098, 2011.

[76] P. Gieske, "Model Predictive Control of a Wave Energy Converter: Archimedes Wave Swing," Delft University of Technology, 2007.

[77] F. Fusco and J. V. Ringwood, "A Simple and Effective Real-Time Controller for Wave Energy Converters," *IEEE Transactions on Sustainable Energy*, vol. 4, no. 1, pp. 21-30,

2013.

[78] A. Babarit, G. Duclos and A. Clement, "Comparison of latching control strategies for a heaving wave energy device in random sea," *Applied Ocean Research,* vol. 26, pp. 227-238, 2004.

[79] M. Lopes, J. Hals, R. Gomes, T. Moan, L. Gato and A. O. Falcao, "Experimental and numerical investigation of non-predictive phase-control strategies for a point-absorbing wave energy converter," *Ocean Engineering,* vol. 36, pp. 386-402, 2009.

[80] G. Li and M. R. Belmont, "Model predictive control of sea wave energy converters - Part I: A convex approach for the case of a single device," *Renewable Energy,* vol. 69, pp. 453-463, 2014.

[81] "Li, Guang; Weiss, George; Mueller, Markus; Townley, Stuart; Belmont, Mike R.," *Renewable Energy,* vol. 48, pp. 392-403, 2012.

[82] J. Cretel, A. Lewis, G. Lightbody and G. Thomas, "An Application of Model Predictive Control to a Wave Energy Point Absorber," *IFAC Proceedings Volumes,* vol. 43, no. 1, pp. 267-272, 2010.

[83] J. Hals, J. Falnes and T. Moan, "Constrained Optimal Control of a Heaving Buoy Wave-Energy Converter," *Journal of Offshore Mechanics and Arctic Engineering,* vol. 133, 2011.

[84] A. O. Falcao and P. Justino, "OWC wave energy devices with air flow control," *Ocean Engineering,* vol. 26, pp. 1275-1295, 1999.

[85] A. Babarit, M. Guglielmi and A. H. Clement, "Declutching control of a wave energy converter," *Ocean Engineering,* vol. 36, no. 12-13, pp. 1015 - 1024, 2009.

[86] A. F. d. O. Falcao, "Phase control through load control of oscillating-body wave energy converters with hydraulic PTO system," *Ocean Engineering,* vol. 35, pp. 358-366, 2008.

[87] A. F. d. O. Falcao, "Modelling and control of oscillating-body wave energy converters with hydraulic power take-off and gas accumulator," *Ocean Engineering,* vol. 34, pp. 2021-2032, 2007.

[88] H. Li, J. E. Braun and B. Shen, "Modeling Adjustable Throat-Area Expansion Valves," in *International Refrigeration and Air Conditioning Conference,* Purdue, 2004.

[89] C.-H. Shin, "A numerical study on the characteristics of transient flow in a pressure regulator resulting from closure of the pressure control valve," *Journal of Mechanical Science and Technology,* vol. 27, no. 2, pp. 443-449, 2013.

Appendix A: Supplementary Information for Model Development

This Appendix aggregates several supplemental descriptions of model components, which are subdivided in the following sections.

A.1 Supplemental Equations for Defining Model-Based Valve Flow Limits

To implement the model-based flow limits described in Section 2.4.4, the optimal pressure is first determined, which is the pressure that the cylinder and tank will both equal in the subsequent time step, provided that optimal mass flow (highest allowable mass flow) occurs. This pressure is then used to determine the optimal mass flow rate. While equations for both $\mathrm{P_{opt,cyl\,outlet}}$ and $\mathrm{\dot{m}_{opt,cyl\ outlet}}$ are given in Section 2.4.4. The full array of equations used in each valve are contained here. The optimal pressure for the inlet flow valve is merely $\mathrm{P_{amb}}$, such that the optimal mass flow rate is given in Eq. A.1.

$$\dot{m}_{\mathrm{opt,cyl\ inlet}} = \left(\frac{1}{R_s T_{\mathrm{amb}}\gamma}\right)\Bigg[\frac{\left(P_{\mathrm{amb}} - P_{\mathrm{cyl,ch.1}}\right)V_{\mathrm{cyl,ch.1}}}{\Delta t} - \gamma P_{\mathrm{cyl,ch.1}}\dot{z}A_{\mathrm{cyl}} \\ + (\gamma - 1)h_{\mathrm{cyl}}a_{\mathrm{cyl,ch.1}}\left(T_{\mathrm{cyl,ch.1}} - T_W\right)\Bigg] \tag{A.1}$$

The optimal pressure and mass flow rate for the valve between the lower and upper chambers of the cylinder is given in Eq. A.2 and Eq. A.3, respectively.

$$P_{\mathrm{opt,cyl\ ch.1\rightarrow ch.2}} = \left(\frac{\Delta t}{V_{\mathrm{cyl,ch.1}}+V_{\mathrm{cyl,ch.2}}}\right)\Bigg[\frac{P_{\mathrm{cyl,ch.2}}V_{\mathrm{cyl,ch.2}}+P_{\mathrm{cyl,ch.1}}V_{\mathrm{cyl,ch.1}}}{\Delta t} + \gamma P_{\mathrm{cyl,ch.1}}\dot{z}A_{\mathrm{cyl}} - \\ (\gamma - 1)h_{\mathrm{cyl}}a_{\mathrm{cyl,ch.1}}\left(T_{\mathrm{cyl,ch.1}} - T_W\right) - \gamma P_{\mathrm{cyl,ch.2}}\dot{z}A_{\mathrm{cyl}} - \\ (\gamma - 1)h_{\mathrm{cyl}}a_{\mathrm{cyl,ch.2}}\left(T_{\mathrm{cyl,ch.2}} - T_W\right)\Bigg] \tag{A.2}$$

$$\dot{m}_{\mathrm{opt,cyl\ ch.1\rightarrow ch.2}} = \left(\frac{1}{R_s T_{\mathrm{cyl,ch.1}}\gamma}\right)\Bigg[-\frac{\left(P_{\mathrm{opt,cyl\ ch.1\rightarrow ch.2}}-P_{\mathrm{cyl,ch.1}}\right)V_{\mathrm{cyl,ch.1}}}{\Delta t} - \gamma P_{\mathrm{cyl,ch.1}}\dot{z}A_{\mathrm{cyl}} - \\ (\gamma - 1)h_{\mathrm{cyl}}a_{\mathrm{cyl,ch.1}}\left(T_{\mathrm{cyl,ch.1}} - T_W\right)\Bigg] \tag{A.3}$$

The optimal pressure and mass flow rate for the valve between the upper chamber of the cylinder and the tank is given in Eq. A.4 and Eq. A.5, respectively. While these formulas are already stated in Section 2.4.4 they are stated again here for continuity.

$$P_{\mathrm{opt,cyl\ outlet}} = \left(\frac{\Delta t}{V_{\mathrm{tank}} + V_{\mathrm{cyl,ch.2}}}\right)\Bigg[\frac{P_{\mathrm{tank}}V_{\mathrm{tank}}}{\Delta t} - \gamma P_{\mathrm{cyl,ch.2}}\dot{z}A_{\mathrm{cyl}} \\ - (\gamma - 1)h_{\mathrm{cyl}}a_{\mathrm{cyl,ch.2}}\left(T_{\mathrm{cyl,ch.2}} - T_W\right) - (\gamma - 1)h_{\mathrm{tank}}a_{\mathrm{tank}}(T_{\mathrm{tank}} - T_W)\Bigg] \tag{A.4}$$

$$\dot{m}_{\mathrm{opt,cyl\ outlet}} = \left(\frac{1}{R_s T_{\mathrm{cyl,ch.2}}\gamma}\right)\Bigg[-\frac{\left(P_{\mathrm{opt,cyl\ outlet}} - P_{\mathrm{cyl,ch.2}}\right)V_{\mathrm{cyl,ch.2}}}{\Delta t} - \gamma P_{\mathrm{cyl,ch.2}}\dot{z}A_{\mathrm{cyl}} \\ - (\gamma - 1)h_{\mathrm{cyl}}a_{\mathrm{cyl,ch.2}}\left(T_{\mathrm{cyl,ch.2}} - T_W\right)\Bigg] \tag{A.5}$$

The optimal pressure and mass flow rate for the valve between the tank and subsequent connecting pipe (used in devices 1 and 2) is given in Eq. A.6 and Eq. A.7, respectively.

$$\mathrm{P_{opt,tank\,outlet}} = \left(\frac{\Delta t}{\mathrm{V_{tank}+V_{pipe}}}\right)\left[\frac{\mathrm{P_{tank}V_{tank}+P_{pipe}V_{pipe}}}{\Delta t} - (\gamma-1)\mathrm{h_{pipe}a_{pipe}}\left(\mathrm{T_{pipe}-T_W}\right) - (\gamma-1)\mathrm{h_{tank}a_{tank}}(\mathrm{T_{tank}-T_W}) + \gamma \mathrm{R_s T_{cyl,ch.2}\dot{m}_{cyl,outlet}}\right] \tag{A.6}$$

$$\mathrm{\dot{m}_{opt,tank\,outlet}} = \left(\frac{1}{\mathrm{R_s T_{tank}}\gamma}\right)\left[-\frac{\left(\mathrm{P_{opt,tank\,outlet}-P_{tank}}\right)\mathrm{V_{tank}}}{\Delta t} - (\gamma-1)\mathrm{h_{tank}a_{tank}}(\mathrm{T_{tank}-T_W}) + \gamma \mathrm{R_s T_{cyl,ch.2}\dot{m}_{cyl,outlet}}\right] \tag{A.7}$$

The optimal pressure and mass flow rate for the valve between the pipe and subsequent cylinder chamber (used in devices 1 and 2) is given in Eq. A.8 and Eq. A.9, respectively.

$$\mathrm{P_{opt,pipe\,outlet}} = \left(\frac{\Delta t}{\mathrm{V_{cyl,ch.1}+V_{pipe}}}\right)\left[\frac{\mathrm{P_{cyl,ch.1}V_{cyl,ch.1}+P_{pipe}V_{pipe}}}{\Delta t} + \gamma \mathrm{P_{cyl,ch.1}\dot{z}A_{cyl}} - (\gamma-1)\mathrm{h_{pipe}a_{pipe}}\left(\mathrm{T_{pipe}-T_W}\right) - (\gamma-1)\mathrm{h_{cyl}a_{cyl,ch.1}}\left(\mathrm{T_{cyl,ch.1}-T_W}\right) + \gamma \mathrm{R_s T_{tank}\dot{m}_{tank,outlet}}\right] \tag{A.8}$$

$$\mathrm{\dot{m}_{opt,pipe\,outlet}} = \left(\frac{1}{\mathrm{R_s T_{pipe}}\gamma}\right)\left[-\frac{\left(\mathrm{P_{opt,pipe\,outlet}-P_{pipe}}\right)\mathrm{V_{pipe}}}{\Delta t} - (\gamma-1)\mathrm{h_{pipe}a_{pipe}}\left(\mathrm{T_{pipe}-T_W}\right) + \gamma \mathrm{R_s T_{tank}\dot{m}_{tank,outlet}}\right] \tag{A.9}$$

Eq. A.6 and Eq. A.7 define the model-based flow limits in both the throughput tank and recirculation tanks. However, an additional set of formulas is needed to define the model-based flow limit when air is passing from the recirculation tank back to the lower and upper cylinder chambers. The optimal pressure and mass flow rate for the valve between the recirculation tank and the lower cylinder chamber is given in Eq. A.10 and Eq. A.11, respectively.

$$\begin{aligned} P_{opt,RT\rightarrow cyl,ch.1} = \left(\frac{\Delta t}{V_{tank} + V_{cyl,ch.1}}\right) \Bigg[& \frac{P_{tank}V_{tank} + P_{cyl,ch.1}V_{cyl,ch.1}}{\Delta t} \\ & - (\gamma - 1)h_{cyl,ch.1}a_{cyl,ch.1}\left(T_{cyl,ch.1} - T_W\right) \\ & - (\gamma - 1)h_{tank}a_{tank}(T_{tank} - T_W) + \gamma P_{cyl,ch.1}\dot{z}A_{cyl}\Bigg] \end{aligned} \tag{A.10}$$

$$\begin{aligned} \dot{m}_{opt,RT\ outlet} = \left(\frac{1}{R_s T_{tank}\gamma}\right)\Bigg[& -\frac{\left(P_{opt,RT\rightarrow cyl,ch.1} - P_{tank}\right)V_{tank}}{\Delta t} \\ & - (\gamma - 1)h_{tank}a_{tank}(T_{tank} - T_W)\Bigg] \end{aligned} \tag{A.11}$$

The optimal pressure and mass flow rate for the valve between the recirculation tank and the upper cylinder chamber is given in Eq. A.12 and Eq. A.13, respectively.

$$\begin{aligned} P_{opt,RT\rightarrow cyl,ch.2} = \left(\frac{\Delta t}{V_{tank} + V_{cyl,ch.2}}\right) \Bigg[& \frac{P_{tank}V_{tank} + P_{cyl,ch.2}V_{cyl,ch.2}}{\Delta t} \\ & - (\gamma - 1)h_{cyl,ch.2}a_{cyl,ch.2}\left(T_{cyl,ch.2} - T_W\right) \\ & - (\gamma - 1)h_{tank}a_{tank}(T_{tank} - T_W) + \gamma P_{cyl,ch.2}\dot{z}A_{cyl}\Bigg] \end{aligned} \tag{A.12}$$

$$\begin{aligned} \dot{m}_{opt,RT\ outlet} = \left(\frac{1}{R_s T_{tank}\gamma}\right)\Bigg[& -\frac{\left(P_{opt,RT\rightarrow cyl,ch.2} - P_{tank}\right)V_{tank}}{\Delta t} \\ & - (\gamma - 1)h_{tank}a_{tank}(T_{tank} - T_W)\Bigg] \end{aligned} \tag{A.13}$$

This set of formulas (A.1 – A.13) defines the application of the model-based flow limit by stating the formulas for each valve in the PTO model; these equations are consistent for each device in the WEC.

A.2 Filter Selection for Actively Controlled System

This section describes how filters for the determination of peaks and troughs in the piston motion (needed for application of the active controller) were determined. The application of these filters within the active controller is described in Section 5.4.2. The two filters used in the filtering process are a Savitzky-Golay (SG) filter, as well as a motion threshold. The motivation behind the selection of the Savitzky-Golay filter, as well as the resulting ideal set of SG filter parameters, is described in the following section. This is followed by the selection of the ideal set of motion threshold parameters; the motivation for the motion threshold is provided in Section 5.4.2.

A.2.1 Selection of Savitzky–Golay Filter

When selecting how best to filter the piston motion signal, analysis was performed on two primary methods: frequency and polynomial based filtering. SG filtering was found to perform much stronger than frequency-based methods, as the frequency bandwidth shifted significantly within the sea-state. The frequency distribution contained within the piston motion in a low (H_s = 1.25 m, T_e = 6.5 s) and high-energy (H_s = 4.25 m, T_e = 10.5 s) sea-state is included in Fig. A.1; these piston motions were gathered during power matrix generation under the influence of the passive control strategy.

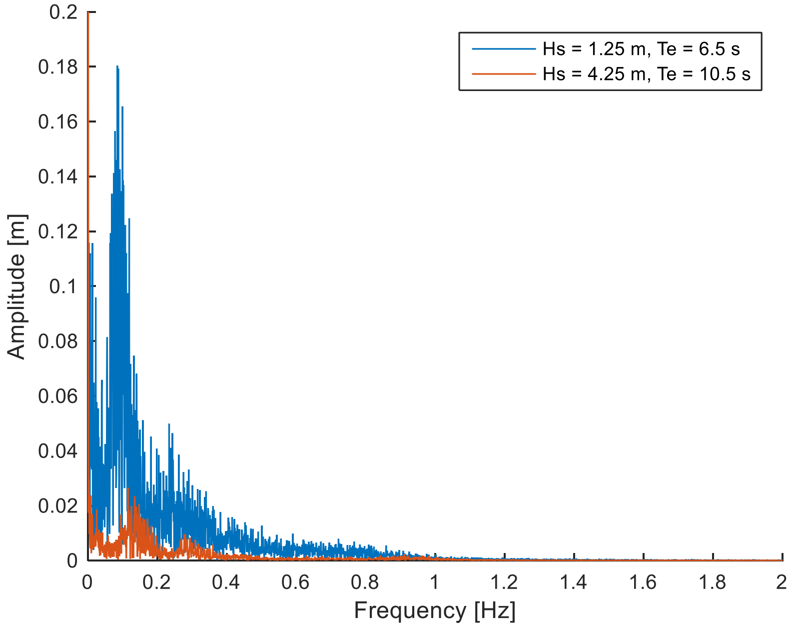

Figure A.1: Single-sided amplitude spectrum of piston motion signal in D_1.

Three frequency peaks are exhibited in the low energy sea-state, while two peaks are seen in the high-energy case. This is an indication that the frequency content of the piston motion signal is highly dependent on the sea-state in which it the WEC is placed. Therefore, no single bandwidth could be used to filter the motion of the piston signal in a variety of sea-states. As a result, attention was shifted to polynomial based filtering. In particular, a Savitzky-Golay (SG) filter was selected as it is a more generalized form of a moving average filter, in which a polynomial is fitted to the last N points of a signal [1]. The SG filter is better than averaging as it allows smoothing without the removal of data features, such as peaks, that are typically attenuated by a moving average filter [1]. The SG filter is based on the following three parameters:

1. Polynomial order
2. Number of points that are used to generate the polynomial.
3. Point about which the polynomial is centered around, which is realized as a delay.

The selection of these parameters was conducted through testing in a combination of sea-states. This testing was initially conducted via post processing of the power matrix simulation data for the passively controlled WEC, followed by testing in the actively controlled system. First, the polynomial order was selected as the minimum order with which the signal could be recreated accurately; this prevents fitting to higher order, non-physical, responses. A second order polynomial was found to meet this criterion, as a linear fit could not capture rapid changes in device motion. A sample comparison of the first and second order polynomial fit for passively controlled piston motion in a low energy sea-state (H_s = 1.25 m, T_e = 6.5 s) is given in Fig. A.2; this piston signal is for passively controlled motion. It is important to note that no delay is introduced in the signal.

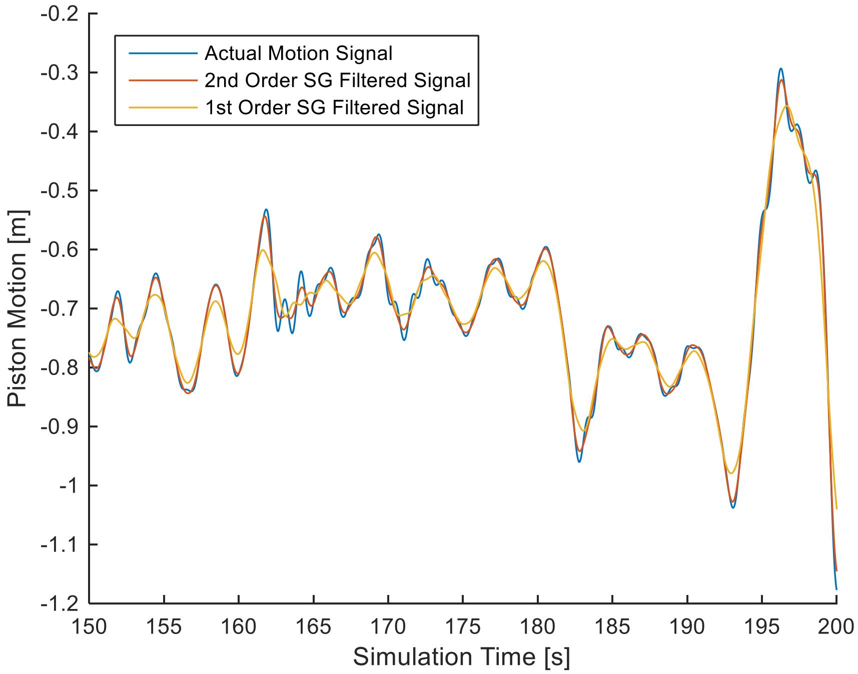

Figure A.2: Sensitivity of SG filter to polynomial order for H_s = 1.25 m, T_e = 6.5 s seas.

The 1st order SG filtered signal is not able to capture the sharp-peaked nature of the piston motion signal; this is clearly exhibited in the time period from 160-170 s, in which the motion of the filtered signal opposes that of the true signal. Conversely, the 2nd order signal tracks peaks accurately; more importantly, it does so without tracking high-frequency motions, such as those seen in the peak from 195-200 s. Consequently, the second order filter was used in the active control strategy. Using the second order polynomial fitting, the number of points used to generate the polynomial was tested with data from power matrix generation under the influence of the passive control strategy. Since the number of points must be odd, the following numbers of points were tested: 401, 601, 801, and 1001. When testing in a low and moderate energy sea-state, for delays of 0.2 s, 0.3 s, or 0.4 s it was found that 801 points produced an equal or stronger fit than the other numbers of points. Since fit was assessed visually, each of these studies are not included here. As an example, Fig. A.3 compares filtered signals using 401, 601, 801, and 1001 points and a delay of 0.4 s to the actual piston motion signal in a low energy sea-state (H_s = 1.25 m, T_e = 6.5 s).

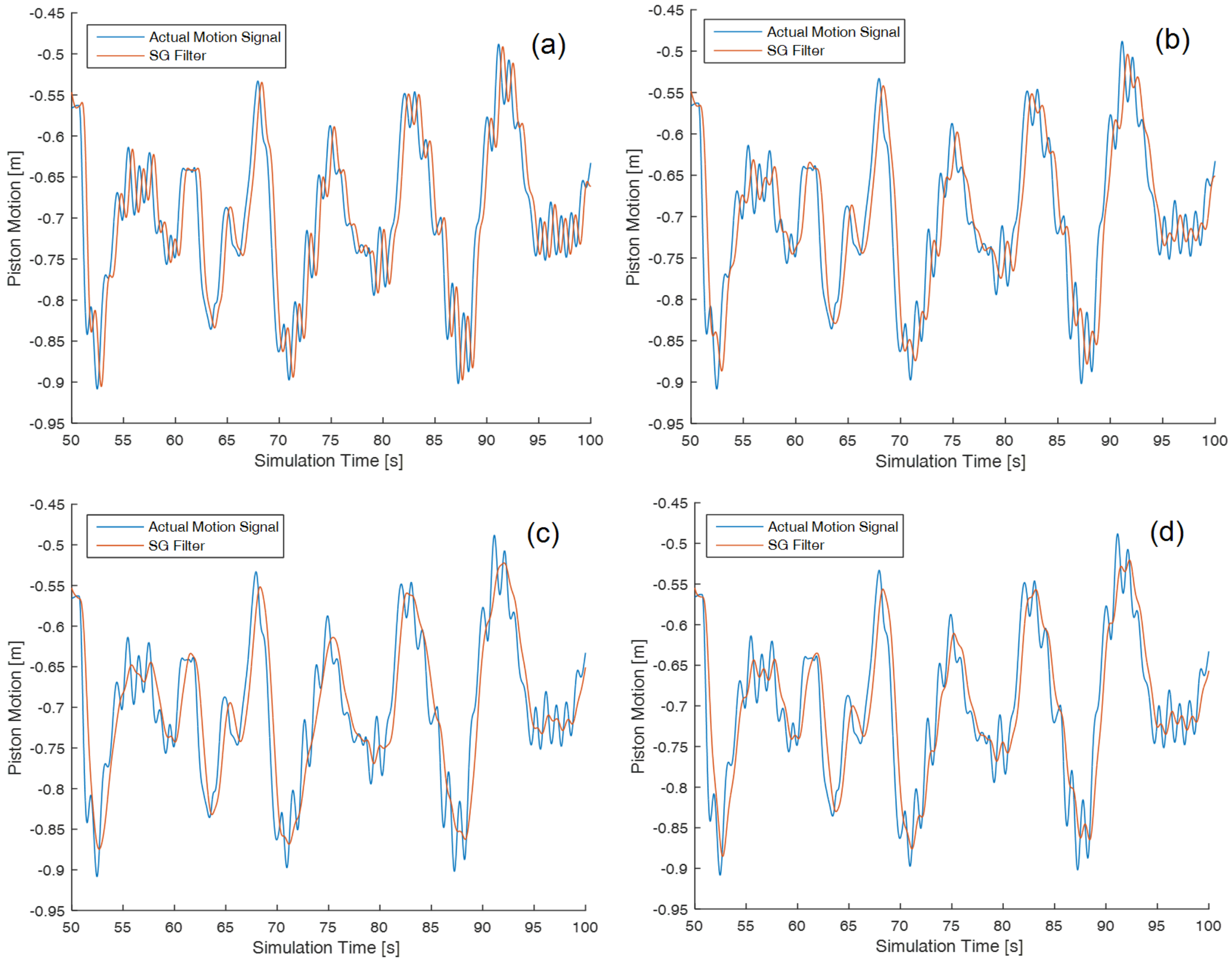

Figure A.3: SG filtered signals using (a) 401 (b) 601 (c) 801 and (d) 1001 points for H_s = 1.25 m, T_e = 6.5 s seas.

When 401 and 601 points were used to produce the SG polynomial, high frequency motions were captured in the signal. Conversely, 801 and 1001 points were able to eliminate most high frequency motions; however, the SG filter using 801 points was able to do so more readily. This behavior could potentially be caused if too many points are included, such that significant curvature is seen in the selected portion of the signal; as a result, additional curvature is added in the signal fit at the current time. While only exhibited for the above sample signal, this behavior was seen repeatedly in other tests. Consequently, 801 points were used in the SG filter.

While the determination of the first two parameters was based on data from the passively controlled system, the delay can only be tested in real-time, as performance of the active control strategy is believed to be highly dependent on the accurate timing of the peak and trough locations. As a result, there is a significant compromise in selecting the delay, as increasing the delay will increase the accuracy of the filtered signal (reaching a maximum at 400 samples, or 0.8 s), but will simultaneously introduce error in the timing of peaks and troughs in the signal. To evaluate the nonlinear compromise between these resultant effects, power production over 500 s was measured for a low (H_s = 1.25 m, T_e = 6.5 s) and moderate (H_s = 2.25 m, T_e = 10.5 s) energy sea-state. The exergy output from each of the three devices in the WEC are contained in Table A.1.

Table A.1: Exergy output as a function of delay in SG filter.

H_s = 1.25 m, T_e = 6.5 s					
Exergy	0.2 s Delay	0.3 s Delay	0.35 s Delay	0.4 s Delay	0.5 s Delay
D_1^* [kW]	1.609	1.647	1.622	Not studied	1.440
D_2^* [kW]	1.547	1.581	1.572		1.488
D_3^* [kW]	0	0	0		0
H_s = 2.25 m, T_e = 10.5 s					
D_1^* [kW]	9.145	10.078	9.785	9.743	9.494
D_2^* [kW]	16.444	17.305	17.198	17.118	16.962
D_3^* [kW]	22.415	23.268	23.245	23.121	22.985

In both cases, and across all three devices, the optimal delay was found to be 0.3 s, which provided a balance between polynomial and timing accuracy. As a result, the final SG filter parameters were to use a 2nd order polynomial, constructed from 801 points, with a delay of 0.3s.

A.2.2 Selection of Motion Threshold Parameters

In order to prevent the act of recirculation inducing peaks/troughs in the piston motion, a motion threshold was applied. The motivation behind the introduction of this threshold is given in Section 5.4.1. The motion threshold only records a peak or trough if the device has moved a certain distance since the last trough and peak, respectively. As a result, when a trough is reached, the act of recirculating air is not sufficient to generate an immediate peak (or vice versa). To select the desired motion threshold, exergy production from each of the three devices was measured over 500 s in three low and moderate sea-states, for which the results are included in Table A.2.

Table A.1: Exergy output as a function of the size of motion threshold.

H_s = 1.25 m, T_e = 6.5 s									
Exergy	**0**	**0.001**	**0.005**	**0.01**	**0.02**	**0.04**	**0.05**	**0.06**	**0.1**
D_1^* [kW]	1.4374	1.5789	1.6472	1.6329	1.7246	1.8451	1.8051	1.7915	1.6326
D_2^* [kW]	1.4926	1.5574	1.5810	1.5782	1.6199	1.6558	1.6417	1.6215	1.5555
D_3^* [kW]	0	0	0	0	0	0	0	0	0
H_s = 1.75 m, T_e = 8.5 s									
D_1^* [kW]	7.7191	7.8825	Not studied	7.3163	Not studied		7.5054	Not studied	
D_2^* [kW]	12.635	12.993		12.430			12.423		
D_3^* [kW]	17.273	17.653		17.041			16.967		
H_s = 2.25 m, T_e = 10.5 s									
D_1^* [kW]	10.149	Not studied	10.078	Not studied			10.166	Not studied	
D_2^* [kW]	17.414		17.305				17.455		
D_3^* [kW]	23.368		23.268				23.454		

For all three sea-states, it can be seen that there are two peaks in performance. It is believed that the first peak corresponds to the point at which the micro-fluctuations are removed, while the second peak corresponds to fundamental changes in device motion, as a result of wave or thermodynamic-induced fluctuations being ignored. Consequently, the relative magnitude of the second peak may/may not be higher than the first, depending on whether the altered piston motion leads to a significant positive improvement. In the three studied sea-states, the second peak was most noticeable in the lowest energy case. This result was expected, since the SG filter does not perform as well in low energy sea-states, particularly those with a small period; these sea-states generate comparatively smaller and sharper peaks in piston motion when compared to high energy sea-states. Consequently, the motion threshold may have removed some of the remaining high frequency oscillations that passed through the SG filter. However, this local peak is not expected to persist in high energy sea-states. As a result, the motion threshold was selected to be 0.005 m, in order to target improvements solely based on the removal of control-induced fluctuations. This corresponded to the smaller, local, peak in the low energy sea-state, and was near the global peak in seas of H_s = 1.75 m, T_e = 8.5 s. In the highest energy sea-state, the exergy was not sensitive to the motion threshold; likely since the energy of the waves was sufficient to damp out any micro-oscillations induced through recirculation.

Appendix A: References

[1] J. L. Guinon, E. Ortega, J. Garcia-Anton and V. Perez-Herranz, "Moving Average and Savitzki-Golay Smoothing Filters Using Mathcad," in *International Conference on Engineering Education* , 2007, 2007.